Title
Ion Energy and Wave Propagation in a Hollow Cathode Plume

Author
Dodson, Christopher

Publication Date
2018

Peer reviewed|Thesis/dissertation

UNIVERSITY OF CALIFORNIA
Los Angeles

Ion Energy and Wave Propagation in a Hollow Cathode Plume

A dissertation submitted in partial satisfaction
of the requirements for the degree
Doctor of Philosophy in Aerospace Engineering

by

Christopher Dodson

2018

ABSTRACT OF THE DISSERTATION

Ion Energy and Wave Propagation in a Hollow Cathode Plume

by

Christopher Dodson
Doctor of Philosophy in Aerospace Engineering
University of California, Los Angeles, 2018
Professor Richard E. Wirz, Chair

Hollow cathodes used as electron sources for long duration and high power electric propulsion missions exhibit a poorly understood phenomenon that can lead to anomalously energetic ion bombardment of cathode surfaces. An understanding of this mechanism is therefore needed to prevent failure of high current cathodes and to enable predictive modeling of cathode lifetime. Recent experimental and theoretical work has shown ion acoustic turbulence (IAT) can in some operating conditions lead to energetic ion formation and subsequent erosion of the keeper. The primary goal of this research is to understand the relationship between IAT and ions in the plume of a high current hollow cathode. Additionally, understanding this relationship will provide insight into the overall importance of IAT to cathode plume behavior such as anomalous resistivity caused by the interaction of IAT with electrons.

The experimental effort used a combination of plasma probes and laser-induced fluorescence (LIF) diagnostics. Parametric studies of ion heating as a function of mass flow rate and discharge current showed an increase of both wave energy and ion heating with discharge current, and a decrease in both with higher mass flow rates. The first study was conducted along the plume centerline, focusing on the scaling of IAT wave energy with ion temperature. For the first time it was shown that ion heating does in fact qualitatively scale with IAT energy locally in the near plume. The scaling parameter for ion heating to wave energy was obtained for a range of operating conditions and locations in the plume, and was

compared to a first-principles-derived fluid formulation for ion heating. These results and accompanying analyses showed that near the cathode the scaling parameter was higher than predicted but converged toward the predicted values downstream.

To delve further into the plume behavior, a second set of experiments investigated the correlation between IAT wave propagation, ion drift, and ion heating in the plume of the same cathode for similar operating conditions. An array of plasma probes was used to measure the IAT wave vectors using correlations between plasma fluctuations, and LIF was used for obtaining the axial and radial ion velocity distribution function. It was also found that variations of discharge current and flow rate resulted in consistent ion velocity and ion acoustic wave vector propagation. It was also found that for the high current to flow rate condition that IAT wave energy and ion heating was much more significant, again providing evidence that there is a scaling between these two properties.

The dissertation of Christopher Dodson is approved.

Benjamin A. Jorns

Dan M. Goebel

George J. Morales

Mohamed A. Abdou

Raymond M. Spearrin

Richard E. Wirz, Committee Chair

University of California, Los Angeles

2018

Table of Contents

List of Figures

List of Tables

Acknowledgments

First I would like to sincerely thank my advisor, Prof. Richard Wirz, who provided guidance, encouragement, and many opportunities throughout my time at UCLA. Although I was initially hesitant to commit to a Ph.D., our conversations motivated me to want to become a researcher, and I am better for it. Most of all I want to thank you for your support through the many ups and downs of graduate school life.

I am also very grateful to have had such an inspiring and qualified graduate committee: Prof. Ben Jorns, Prof. George Morales, Dr. Dan Goebel, Prof. Mohamed Abdou, and Prof. Mitchell Spearrin. All of you challenged my work in the right ways, and I am proud to have been your student.

To the members of the UCLA Plasma and Space Propulsion Laboratory, I will always be glad for the time we spent as friends and colleagues. I would especially like to thank Dr. Taylor Matlock and Dr. Ben Dankongkakul for setting such a high bar for research quality. The camaraderie of the lab is what I will miss most about my time at UCLA.

Lastly, I would like to thank the funding agencies and institutes who enabled this research. My fellowship was supplied by the National Science Foundation Graduate Research Fellowship (Grant No. DGE-1144087). The experimental campaign was carried out as part of a collaboration between the University of California, Los Angeles, and the Jet Propulsion Laboratory, California Institute of Technology, under a contract with the National Aeronautics and Space Administration. The support of the joint NASA GRC and JPL development of HERMeS by NASA's Space Technology Mission Directorate through the Solar Electric Propulsion Technology Demonstration Mission project is also gratefully acknowledged. I would also like to acknowledge Ray Swindlehurst and Nowell Niblitt for their assistance in running the experimental facility, and Mohamed A. Elhafsi for experimental setup and operation.

Vita

2003–2006	NASA Undergraduate Student Research Program - NASA Marshall Space Flight Center, research advisor: Dr. Thomas Markusic.
2006	B.S. Mechanical Engineering, Ohio University.
2007-2013	Propulsion Engineer, SpaceX.
2013–2014	Graduate Student Researcher, UCLA Plasma and Space Propulsion Laboratory.
2014-2017	National Science Foundation Graduate Student Research Fellowship.
2014	M.S. Aerospace Engineering, UCLA.

Publications

Dodson, C., Jorns, B., and Wirz, R., "Measurements of Ion Velocity and Wave Propagation in a Hollow Cathode Plume", *Plasma Sources Science and Technology*, 2018 (in review).

Dodson, C., Perez-Grande, D., Jorns, B., Goebel, D., and Wirz, R., "Ion Heating Measurements on the Centerline of a High-Current Hollow Cathode Plume", *Journal of Propulsion and Power*, Vol. 34, No. 5, (2018), pp. 1225-1234.

Dodson, C., Jorns., B., and Wirz, R., "Ion Acoustic Wave Propagation and Heating in a High-Current Hollow Cathode Plume," 35th International Electric Propulsion Conference, Atlanta, GA, Oct 8-12, 2017.

Jorns, B., Dodson, C., Goebel, D., and Wirz, R., "Propagation of Ion Acoustic Wave Energy in the Plume of a High-Current LaB6 Hollow Cathode", *Physical Review E* 96, 023208, (2017).

Dodson, C., Perez-Grande, D., Jorns, B., Goebel, D., and Wirz, R., "Laser-induced Fluorescence Measurements of Energetic Ions in a 100-A LaB6 Hollow Cathode", 52nd AIAA/ASME/SAE/ASEE Joint Propulsion Conference and Exhibit, Salt Lake City, UT, July 25-27, 2016.

CHAPTER 1

Introduction and Motivation

1.1 Introduction

Long-duration space missions (up to 50,000 h) have been proposed over the past two decades that would utilize ion propulsion[3], and recently with the advent of magnetic shielding[4] Hall thrusters are now also being considered for such missions[5, 6]. Hollow cathodes, which provide electrons for ionization and neutralization, must also be able to meet these ambitious lifetime requirements. For example, recently a LaB_6 cathode designed for a 12.5 kW Hall thruster was developed to have a lifetime of as long as 75,000 h when considering emitter lifetime and orifice erosion rates[7]. However, erosion of discharge cathode keepers and thruster surfaces, caused by energetic ion production in the plume, still needs evaluated for these long-duration missions. Additionally, as the power of electric propulsion increases so too does the current needed from hollow cathodes. Recently a LaB_6 cathode was developed for an 80 kW Hall thruster that can sustain a current of up to 300 A[8], but at these high currents significant erosion of the cathode keeper and orifice plate was observed. High flow rate external gas injection was needed reduce energetic ion production sufficiently to enable >10,000 h missions. The duration and cost of lifetime testing of thrusters and hollow cathodes could be much reduced if the mechanism responsible for energetic ion production could be understood and modeled.

Recent experimental and theoretical developments have shown an increasingly strong case that ion acoustic turbulence (IAT), caused by a high electron drift velocity, is the cause of the ion heating. In this work we investigate the correlation in the near plume between

ion heating and wave energy propagation using laser and probe diagnostics over a range of operating conditions. In addition to providing more information on the cause of energetic ion production, measuring the propagation direction and energy of acoustic waves in the near plume will be useful in a more general sense because of the importance of acoustic waves to the macroscopic plasma equilibrium and the transport of particles and energy in the plume. These aspects are not currently modeled self-consistently, so these measurements could provide insight into the mechanisms that need to be captured in the models, and data from the experiments can be used for benchmarking simulations.

1.2 Hollow Cathodes

Hollow cathodes are efficient plasma sources used for a variety of applications. Industrial applications include plasma processing and ion etching. In this work, we focus on the application of hollow cathodes to electric propulsion (EP), in which it is used as an efficient electron source for Hall and ion thrusters (Fig. 1.1). A cross-section of a typical hollow

(a) MaSMi Hall thruster [9]. (b) NEXT ion thruster [10].

Figure 1.1: Electric propulsion applications of hollow cathodes.

cathode design is shown in Fig. 1.2 [11]. It consists of an annular cathode tube inside of which is an insert made of a material that thermionically emits electrons when heated. Dur-

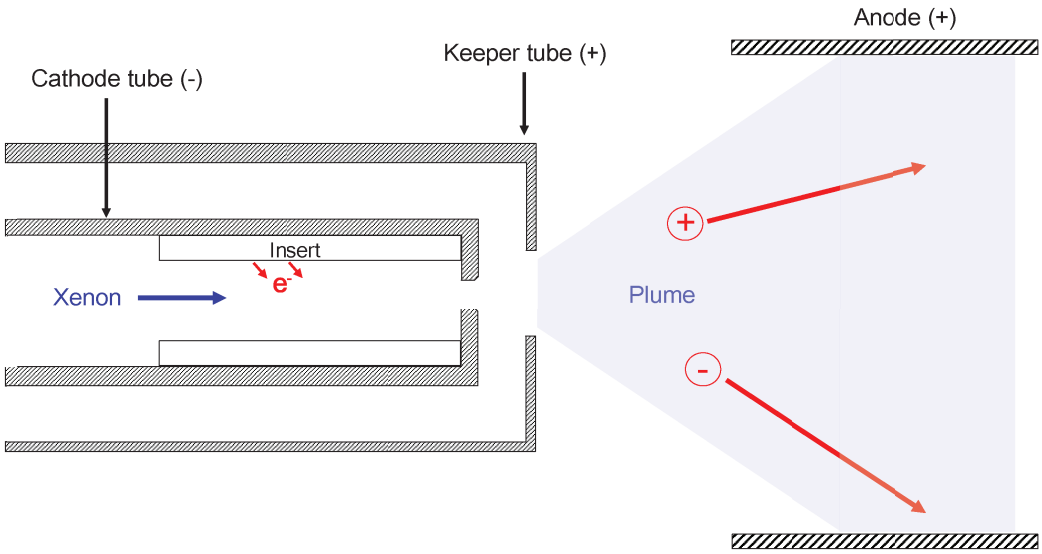

Figure 1.2: Cross-section of a typical hollow cathode.

ing start-up the heat is supplied by a resistive heater (typically tantalum) wrapped around the cathode tube. After start-up the heater is turned off and the emitter temperature is maintained by conduction from the orifice and from ion and electron bombardment of the emitter by the insert region plasma. Outside of the cathode is an anode which generates an electric field drawing electrons from the cathode plasma plume, where they ionize a propellant gas which flows through the cathode. To protect the cathode from ion bombardment which can limit the device lifetime, a keeper is installed which intercepts most of the ions incident on the cathode. For high current cathodes both the cathode and keeper tubes are constructed out of graphite, with the orifice plate some hard refractory metal such as tungsten or molybdenum. The conditions in the plume of hollow cathodes vary widely depending on the application. Typical ion and Hall thruster discharge cathodes operate at $<$20 A, while neutralizer cathodes for ion thrusters operate at a fraction of that, in the mA range. In this work, we operate at high discharge currents such that the levels of ion acoustic turbulence dominates the energy spectrum, allowing us to isolate the ion acoustic mode from other modes, such as the lower frequency ionization-type oscillations. This also allows us to focus on the effects that are typically only found in high power discharge cathodes.

1.3 Previous Work

The motivation for this work stemmed from the observations of high erosion rates of surfaces exposed to high-current hollow cathode plumes. In 1988 both Rawlin[12] and Brophy and Garner[13] saw evidence of energetic ions in both axial and radial directions. They believed these ions had to have energies in excess of the discharge voltage to explain the erosion rates seen based on the plasma densities present and assuming the maximum ion energy to be that of the cathode-to-anode potential (<30 V). Since that time many researchers have measured the ion energy distribution function (IEDF) using retarding potential analyzers (RPAs) in hollow cathode plumes[14, 15, 16, 17, 18, 19, 20, 21, 22]. Many of the studies showed energies well in excess of the discharge voltage. Chu et al.[20] showed that, although higher gas flow rates reduced energetic ion production, injecting gas directly into the near plume resulted in a more significant reduction in ion energies. This is the approach used in the X3 cathode since its very high current (up to 300 A) has shown high erosion rates of the keeper without external gas injection. Ho's more recent measurements of erosion of the keeper face of a 100 A LaB_6 cathode also show that erosion rates are higher than can be explained by ions falling through the sheath potential alone, and the location of the erosion was farther off-axis than expected, indicating that the ions were being accelerated by a different mechanism[23].

Recent work at JPL has shown the formation of these energetic ions may be explained by the presence of ion acoustic turbulence in the cathode plume. Mikellides et al. claimed that a high electron Mach number could exist in the plume which could drive IAT[24]. Experiments by Jorns et al. confirmed the existence of IAT in the plume and found the IAT wave energy to increase with discharge current and decreasing flow rate[25, 26, 27]. These experiments also provided evidence that the waves are dampened by collisions between ions and neutral gas. This is promising in that it suggests that for cathode operating conditions in which energetic ions are produced, the wave energy and therefore ion energy can be either reduced by gas injection or choice of an operating condition that results in less turbulent heating from the ions. Additionally, theoretical and experimental work by Jorns et al. indicated that the wave

energy was sufficient to cause the formation of a hot ion tail, and RPA measurements showed qualitative agreement with a 1D kinetic model ion heating on the cathode centerline[21]. However, in that study no measurements of the axial IVDF were obtained and the radial IVDF was measured only at a single location, 10 cm from the cathode centerline (compared to a plume diameter of 2 cm). While these results indicate IAT has a role in ion heating, high spatial resolution maps of the IVDF in the cathode plume are needed to evaluate the extent of this effect on IVDF evolution.

Besides the work specifically focusing on IAT for EP-specific cathodes, experimental measurements of ion acoustic waves and fluctuations associated with the ion acoustic instability have a long history. The following experiments are particularly relevant to this study: measurements of phase velocity and fluctuation specrum by Fenneman in a positive column He discharge [28] (similar to our conditions, i.e. partially ionized while pulling a net current); measurements of acoustic wave propagation directions by Gekelman [29]; measurements of wave energy and angular dependence of the fluctuation spectrum by Slusher [30]; and measurements of fluctuation spectra of current-driven instabilities by Hamberger [31].

In addition to the experimental observations, simulations using OrCa2D at JPL have predicted operating conditions that result in a potential structure that would cause ions born in the plume to be accelerated back towards the keeper and thruster surfaces. Should the mechanism responsible for heating add to the ion temperature component normal to the keeper, anomalous erosion could occur. In the far plume, energetic ions might impact the screen grid and anode of ion thrusters, also causing anomalous erosion. Due to the non-linear relationship between sputter yield and ion energy, it is important to know both the fluence and energy of ions incident on thruster surfaces to bound the erosion rate and, therefore, the lifetime of high power thrusters.

1.4 Thesis Objectives

The objective of this work is to understand how fluctuations related to the ion acoustic mode correlate to ion energy in a cathode plume for a range of operating conditions. Laser-induced fluorescence (LIF) is used to measure the IVDF via Doppler shift of an atomic transition of xenon ion and plasma probes are used to measure the energy contained in the turbulent plasma fluctuations. The correlation between the two are analyzed and compared to a fluid model of the plume to better understand the relevant physical mechanisms and the type of model needed to predict ion heating. From these measurements and analyses, scaling laws will be derived to with the goal enable predictive modeling of ion heating in cathode plumes for lifetime prediction.

1.5 Thesis Overview

The remainder of this dissertation is organized as follows. Chapter 2 presents a description of the properties of the ion acoustic mode relevant to this study. The dispersion relation is presented, followed by wave energy calculations and relating energy to ion temperature through a scaling parameter. Chapter 3 describes the experimental setup. First, the plasma probing techniques for both steady-state and fluctuation measurements are described, then the LIF technique for singly-charged xenon ions is discussed.

Chapter 4 presents the results from the first test series of ion heating due to IAT involving measurements along the centerline of a high current hollow cathode. Ion energy measurements from two independent diagnostics are compared to each other, and wave energy measurements are presented. A scaling analysis was performed to relate wave to thermal energy of the ions. Chapter 5 covers the results from the second test series that was performed on a 2D half-plane in the cathode plume. Background properties, ion flow and temperature, and wave flow and energy results are presented. An analysis of the correlations between wave energy, ion energy, and the propagation of both is then presented, followed by

a brief discussion of the background effects on the plume properties.

Finally, Chapter 6 reviews the results of this study and provides recommendations for future work. An appendix is provided that contains the 2D measurements for all operating conditions.

CHAPTER 2

Theory

2.1 Introduction

For plasmas with a net current such as in the hollow cathode plume, the current is primarily carried by the electrons due to their higher mobility. This current results in an electron distribution function shifted by the mean drift velocity, V_e. Once the drift velocity reaches the value of the ion acoustic velocity, which for cold ions is $c_s = \sqrt{T_e/M}$, an instability develops, and the amplitude of the ion fluctuations will grow (convected downstream). When finite ion temperature is considered this drift velocity threshold increases, until at the point when $T_i \sim T_e$ where the threshold is equal to the electron thermal velocity, $v_e = \sqrt{T_e/m}$ [32]. Beyond an electron Mach number of 1, where this parameter is defined as $M_e = V_e/v_e$, there is the potential for the Buneman instability to develop. Both the ion acoustic and Buneman modes interact with both electrons and ions, modifying their temperatures and potentially their drift velocities through wave-particle interactions.

In this research we focus on the effects of the ion acoustic mode and disregard the potential of the Buneman instability. As will be discussed, the electron Mach number is not a parameter that was directly measured and was only inferred based on averaging across a cross-section of the plume. However, simulations estimate that $M_e < 1$ for these plume conditions which would imply that the acoustic mode is the dominant one.

2.2 Ion Acoustic Waves

Ion acoustic waves are electrostatic, longitudinal oscillations in plasma potential, ϕ, and plasma density, n, that propagate at the acoustic velocity c_s. The properties of the wave are described by the dispersion relation that relates the frequency, ω, to the wavenumber, k. Here we will present the dispersion relation in a manner following Tenneman [28] and Jorns [26] after which we will discuss the growth rate.

For this derivation we start with several broad assumptions that simplify the analysis. First, we initially do not apply any magnetic field, and the self-magnetic field due to the current can be neglected. We assume the modes are electrostatic, i.e. there is no perturbed magnetic field. The only correlations considered are Coulomb, and that the BGK model for collisions is sufficient, which approximates collisions as a constant collision frequency operating on a current and equilibrium distribution function [33]: $\nu_s(f_s - f_{0s})$, where s denotes denotes the species and nu_c is the collision rate. Finally, we consider the 1-dimensional case along the centerline of the plume. Making these assumptions we start with the kinetic equation:

$$\frac{\partial f_s}{\partial t} + v\frac{\partial f_s}{\partial z} + \frac{e}{m_s}E\frac{\partial f_s}{\partial v} = -\nu_s(f_s - f_{0s}). \tag{2.1}$$

We also use Poisson's equation to relate the electric field to the distribution functions:

$$\frac{\partial E}{\partial z} = \frac{e}{\epsilon_0}\left(\int f_i \,\mathrm{d}v - \int f_e \,\mathrm{d}v\right). \tag{2.2}$$

We next assume that the distribution functions and fields are composed of a steady-state and fluctuating component, i.e. $f_s = f_{s0} + f_{s1}$ and $E = E_0 + E_1 \approx E_1$ if we assume the background electric field is low, which is true at least along the centerline of hollow cathode plumes based on experimental measurements. In order to assume the waves propagate as plane waves, we invoke the eikonal approximation, i.e. that the plasma properties have a weak spatial variation and that in order to propagate the wavelength must be short relative

to the distance over which the medium varies, which we approximate using the gradient length scale $L = n/\nabla n$. This allows us to Fourier analyze this equation to transform spatial and temporal derivatives into frequency space using the generic formulation $A = \widehat{A}e^{i(kx-\omega t)}$, where A is any property and $\widehat{A}$ is the amplitude of the fluctuation.

Substituting Fourier-analyzed electric field and distribution functions into the Boltzmann and Poisson equations, ignoring higher-order terms and using the relationship $\int f_s \, \mathrm{d}v = n_s$, we have:

$$\frac{\partial f_{1s}}{\partial t} + v\frac{\partial f_{1s}}{\partial z} + \frac{e}{m_s}E_1\frac{\partial f_{0s}}{\partial v} = -\nu_s f_{1s} + \nu_s \frac{n_{1s}}{n_0} f_{0s} \tag{2.3}$$

$$\frac{\partial E_1}{\partial z} = \frac{e}{\epsilon_0}(n_{1i} - n_{1e}) \tag{2.4}$$

Fourier analyzing the derivatives, substituting E_1 from Eq. 2.4 into Eq. 2.3 for each species, and assuming the unperturbed distribution functions are displaced Maxwellians, we arrive at the dispersion relation for this mode:

$$\epsilon(\omega, k) = 1 - \frac{1}{2k^2}\sum_{s=e,i}\frac{1}{\lambda_{ds}^2}\frac{Z'(\zeta_s)}{1 + i(\nu_s/(kv_s\sqrt{2}))Z(\zeta_s)}, \tag{2.5}$$

where ϵ is the plasma dielectric tensor, $\lambda_{ds} = (\epsilon_0 T_s/q^2 n_s)^{1/2}$ is the Debye length. $Z(\zeta_s)$ and $Z'(\zeta_s)$ are the plasma dispersion function and its derivative, respectively, defined by:

$$Z(\zeta_s) = i\sqrt{\pi}e^{-(\zeta_s)^2}[1 + \mathrm{erf}(i\zeta_s)], \tag{2.6}$$

$$Z'(\zeta_s) = -2(1 + \zeta_s Z(\zeta_s), \tag{2.7}$$

and the ζ_s term, which is in general complex ($\zeta = x + iy$), physically represents the ratio of

the wave phase velocity to the particle thermal velocity, and is given by

$$\zeta_s = \frac{\omega + i\nu_s - kV_s}{k}\left(\frac{m_s}{2T_s}\right)^{1/2}, \tag{2.8}$$

where V_s is the drift speed.

The dispersion relation in Eq. 2.5 is complicated and highly nonlinear. To simplify, we make several further assumptions. First, we observe that the typical ordering of velocities in hollow cathode plasmas is: $v_i \ll c_s \ll V_e \ll v_e$. This allows us to only consider the cases when $|\zeta_e| \ll 1$ and $|\zeta_i| \gg 1$, where we can use Taylor and asymptotic expansions, respectively, to enable an analytical expression for the dispersion relation [34]. For electrons with small ζ_e, we use the Taylor expansion

$$Z(\zeta_e) = i\pi^{1/2}e^{-\zeta_e^2} - 2\zeta_e\left[1 - \frac{2\zeta_e^2}{3} + \frac{4\zeta_e^4}{15} - \frac{8\zeta_e^6}{105} + \mathcal{O}(\zeta_e^8)\right], \tag{2.9}$$

and for large $\zeta = x + iy$, appropriate for ζ_i, we use the asymptotic expansion

$$Z(\zeta_i) = i\pi^{1/2}\sigma e^{-\zeta_i^2} - \zeta_i^{-1}\left[1 + \frac{1}{2\zeta_i^2} + \frac{3}{4\zeta_i^4} + \frac{15}{8\zeta_i^6} + \mathcal{O}(\zeta_i^{-8})\right], \tag{2.10}$$

where,

$$\sigma = \begin{cases} 0 & y > |x|^{-1} \\ 1 & |y| < |x|^{-1} \\ 2 & y < -|x|^{-1} \end{cases} \tag{2.11}$$

We approximate the frequency dependence by separating the dielectric tensor into real and imaginary components: $\epsilon(\omega, k) = \epsilon_r + i\epsilon_i$. We assume k is real, which allows $\omega = \omega_r + i\omega_i$. If the growth rate is small, i.e. $\omega_i \ll \omega_r$, we can Taylor expand the dielectric function with respect to ω_r. These assumptions result in two relations from which we can obtain

information regarding the frequency dispersion and growth rate of this mode:

$$\epsilon_r(\omega_r, k) = 0, \tag{2.12}$$

$$\omega_i = -\frac{\epsilon_i(\omega_r, k)}{\partial\epsilon_r(\omega_r)/\partial\omega}, \tag{2.13}$$

Applying the relation in Eq. 2.12 to Eq. 2.5 yields the kinetic dispersion for the real frequency of the ion acoustic mode:

$$(\omega_r^{'})^2 = k^2 c_s^2 \left(\frac{1}{(\lambda_{de})^2 + 1} + 3\frac{T_i}{T_e} \right). \tag{2.14}$$

where $\omega^{'} = \omega - kV$. For cold ions $T_i \ll T_e$ and large wavelengths $k\lambda_{de} \ll 1$, the phase velocity (which in this case is also equal to the group velocity) is just the ion acoustic speed:

$$v_g = \omega/k = c_s. \tag{2.15}$$

For our conditions, the long wavelength approximation holds (due to high density and thus small λ_{de}), ad we get the following approximate real component of the dispersion relation (which is what would be measured):

$$\omega \approx k\left[c_s \left(1 + 3\frac{T_i}{T_e} \right)^{1/2} + V_i \right], \tag{2.16}$$

where we have made the substitution $\omega_r \to \omega$ and have transformed back into the lab frame.

Analyzing the imaginary part of ω from Eq. 2.13 yields the growth rate of the mode, γ:

$$\gamma = 2\omega_I = c_s k \left[\left(\frac{\pi}{2} \right)^{1/2} \left(\frac{V_{de}^{'} - c_s}{v_e} \right) - \left(\frac{\pi}{2} \right)^{1/2} \left(\frac{T_e}{T_i} \right)^{3/2} e^{-T_e/2T_i} \right] - \nu_i, \tag{2.17}$$

where $V_{de}^{'} = V_{de} - V_{di}$ is the drift velocity of the electrons relative to the ions. The first term inside the brackets represents inverse electron Landau damping of the wave, in which

the wave gains energy at the expense of the electron drift. The second term represents ion Landau damping. Typically ion acoustic waves are only observed for $T_e \gg T_i$, but for strong electron drift (generally, but not always, associated with a high net current), the waves can propagate even with strong damping. The last term represents damping of the wave through collisions of the ions with other particles, which for our conditions is dominated by ion-neutral collisions.

2.2.1 Validity of Weak Damping Approximation

The conditions that justify the expansions used to obtain the analytical expressions for the dispersion relation are usually associated with cold ions ($T_i \ll T_e$, making $\omega/k \gg v_i$) and low particle drifts (particularly $V_e \ll v_e$). As we will show in the results sections, the presence of ions with temperature $T_i \approx T_e$ would result violate the latter assumption in a lower value of ζ_i (since $\omega/k \sim v_{i,th}$ in the reference frame of the ions). Additionally, as showed by Jorns [1], the electron Mach number could possibly be large (up to 3). This would result in $|\zeta_e| \not\ll 1$.

The fully self-consistent analysis of this system requires solving the dispersion relation, Eq. 2.5. Here we have performed that numerically using a Mathematica root-finding algorithm for various values of electron Mach number and ion-electron temperature ratios, assuming a fixed electron temperature of 2.5 eV and ion drift velocity of 4 km/s (this latter parameter will only affect the slope value, not relative change in the group velocity). Increasing electron drift or ion temperatures results in a reduction in the slope of the dispersion relation relative to the that obtained using Eq. 2.14, but that it is more sensitive to the electron drift. For conditions in which $M_e < 1$, precicted by simulations, the reduction in the group velocity will be $< 20\%$. The trend of slope with respect to ion temperature is consistent with that predicted by Landau [35], who claimed that in the strong damping limit the dispersion relation would be such that $\omega \propto k/(\ln k)^{1/2}$.

This analysis assumes isotropic and Maxwellian velocity distribution functions for both ions and electrons, and neglects the presence of multiple particle populations. As will be

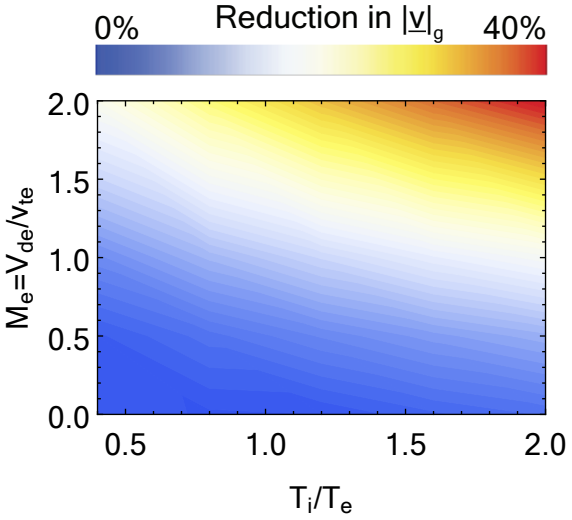

Figure 2.1: Reduction in group velocity estimated using the slope of the dispersion relation measurements. Analysis was performed assuming $T_e = 2.5$ eV, $V_i = 4$ km/s.

shown in the results sections, measurements in this study show that for the operating conditions in which the ions are heated, these assumptions may no longer hold. For this reason, we do not apply any corrections to the simplified dispersion relation used to obtain the group velocities (which, in turn, allow us to generate the wave vector propagation plots), and Fig. 2.1 serves only to illustrate the order of the correction possible. Additionally, this analysis was not extended to the imaginary component of the dispersion relation (Eq. 2.17, providing the damping rate) since no quantitative analysis on growth rates was performed here. One final note is that this analysis was performed up to $M_e = 2$, but for $M_e > 1$ this dispersion relation may no longer be applicable as the stronger Buneman instability may be initiated which has a different dispersion relation. This analysis also illustrates the importance in knowing the electron drift velocity in order to get the appropriate values for the group velocity vectors from correlation measurements.

2.3 Ion Acoustic Turbulence

The ion acoustic instability results in an unstable fluctuation spectrum across all wave numbers. In reality the low-frequency limit is set by geometric constraints or collisions, and the high-frequency limit is set by nonlinear saturation mechanisms such as electron trapping, ion resonance broadening, or nonlinear ion Landau damping, which result in a transfer of energy from high to low frequencies [26]. Analysis by Jorns using the measurements presented in this study indicate that the Sagdeev scaling for nonlinear Landau damping appears to be a possible mechanism to explain the saturation observed [1].

The result is a spectrum of fluctuations that typically spans from ∼100 kHz up to several MHz. Scattering of the electrons on the waves results in what is referred to as anomalous resistivity (in that it can greatly exceed the classical resistivity caused by Coulomb collisions) and Joule heating of the electron population. Despite being heated, due to energy conservation the net kinetic energy of the electron population decreases. The ions interact with the waves through ion Landau damping, which extracts energy from the waves and heats the ions. The turbulent waves exist as a cone-shaped spectrum of vectors dominated by growth in the direction of the relative electron drift velocity, $\vec{V}_{de} - \vec{V}_{di}$ [36], and confirmed by experiments such as that by Slusher [30].

To estimate the low-frequency cutoff, we first address the geometric cutoff. We approximate the cutoff distance as the density gradient length scale, $L = n_e/\nabla n_e$. With $k_c = 2\pi/L$, where k_c is the cutoff wavenumber, substitution into the dispersion relation (Eq. 2.16) results in the low frequency cutoff:

$$\nu_L = \frac{(c_s + V_{di})}{L}. \tag{2.18}$$

Another relevant parameter for the low frequency cutoff is the ion-neutral collision frequency, ν_{in}. For this weakly ionized plasma we assume the dominant collisions are due to

charge-exchange or elastic ion-neutral collisions, leading to the following:

$$\nu_{in} = \nu_{CEX} + \nu_{el} = n_n v_i (\sigma_{CEX} + \sigma_{el}), \tag{2.19}$$

where n_n is the neutral gas density, $v_i = \sqrt{2T_i/m_i}$ is the ion thermal velocity, and the cross-sections for charge-exchange and elastic collisions are, using Ref. 37, approximated by $\sigma_{CEX} = (-0.8821 \ln|v_i - v_n| + 15.1262) \times 10^{-20} m^2$ and $\sigma_{el} = 6.42 \times 10^{-16}/|v_i - v_n| m^{-2}$, respectively. We can approximate the neutral gas density by assuming it is collisionless in the plume and has a finite divergence angle using $n_n = Q_n/v_{n0}\pi(r_0 + \theta z)^2$, where Q_n is the neutral particle flow rate, v_{n0} is the neutral gas velocity (approximated as $\sqrt{2T_n/m_n}$ and assuming T_n, the neutral gas temperature is $\sim$ 1000 K), r_0 is the keeper orifice diameter, and θ is the divergence angle of the plume ($\sim$45°).

2.3.1 Wave Energy

For electrostatic waves, the spectral energy density for the k^{th} mode of the ion acoustic waves is:

$$E_k = \epsilon_0 \frac{k^2 \phi_k^2}{2} \omega_r \frac{\partial \epsilon_r}{\partial \omega_r} = \frac{\omega_r}{k c_s} \left(\frac{n_0 q^2 \phi_k^2}{T_e} \right). \tag{2.20}$$

where ϵ_r is the real component of the dielectric tensor. The total wave energy is then the integral through all wavenumbers [38]:

$$E_T = \frac{\epsilon_0}{2} \frac{1}{V_k} \int_0^\infty \omega' [k \widetilde{\phi}(k)]^2 \frac{\partial \epsilon_r}{\partial \omega'} \, \mathrm{d}\boldsymbol{k}, \tag{2.21}$$

where $\omega' = \omega - k V_{di}$, $\widetilde{\phi}(k)$ is the amplitude of the fluctuating plasma potential of acoustic mode with wavevector $\boldsymbol{k}$. Note that this is over all wavenumber space. However, using Ref. [36], we note that ion acoustic waves propagate in a small cone centered about the direction of the relative electron drift V_{de}'. If we assume that the majority of the wave energy is along this drift direction then the volumetric integral in Eq. 2.21 becomes a line integral

in k-space, L_k. Using the dispersion relation and this assumption, we obtain:

$$E_T = \frac{1}{T_e}\frac{1}{L_k}\int_{1/\omega_0}^{1/\omega_{pi}} q\widetilde{\phi}(k)^2 \,\mathrm{d}k, \tag{2.22}$$

where the lower integral bound ω_0 is chosen based on the lower cutoff of the mode, which will be discussed in the next section. The maximum frequency for the ion acoustic mode is the plasma frequency, $\omega_{pi} = \sqrt{ne^2/\epsilon_0 M}$. Rewriting in frequency space gives:

$$E_T = \frac{1}{T_e}\int_{\omega_0}^{\omega_{pi}} \frac{q^2\widetilde{\phi}(\omega)^2}{L_\omega} \,\mathrm{d}\omega, \tag{2.23}$$

where we express L_k inside the integral since that is how the measured spectral power per frequency was taken as a single measurement at each frequency. Accounting for the drift results in the following, expressed as a summation:

$$E_T = \sum_{\omega_0}^{\omega_{pi}} \frac{q^2(\widetilde{\phi}_\omega^2/L_\omega)}{T_e(1+3T_i/T_e)}\left[1+\frac{V_i}{c_s}\right]. \tag{2.24}$$

This expression shows that the thermalized energy of the distribution can be related to the total wave energy.

2.4 Scaling of Ion Temperature and IAT Wave Energy

In order to predict the energies and fluxes of ions in the plume of hollow cathodes for lifetime considerations, we desire a way to determine, self-consistently, the wave energy and the interaction of the waves with the various species and with itself (i.e. wave-wave and wave-particle-wave coupling). To address this, Jorns proposed a method wherein IAT and the effects it has on the plume plasma is self-consistently treated using a fluid formulation [39], which we briefly describe here. The conventional fluid equations are derived by taking moments of the kinetic equation (Eq. 2.1). To incorporate turbulent fluctuations into a

fluid model, the the RHS of the kinetic equation retains a term for first order fluctuations in electric field and density. Including this term when taking moments results in additional terms in the momentum and energy equations equivalent to turbulent-driven anomalous force and heat flux terms, respectively. These terms are related to the wave energy distribution in frequency and physical space using an assumption for the wave energy spectrum and the kinetic wave equation, which describes the evolution of wave energy density as the waves are convected into the plume. Parameters within that equation can be related to the macroscopic parameters through the dispersion relation, and moments of the kinetic wave equation then result in a relation for total wave energy to macroscopic parameters. Substituting this into the turbulent terms of the fluid equations then provides a set of modified fluid equations that accounts for turbulent fluctuations as they relate to Maxwellian distributions. Note that this approach cannot account for resonantly coupling of IAT to the ions or electrons. This approach also requires an assumption regarding the shape of the wave energy spectrum, or that the shape can effectively be accounted for in an average IAT wave frequency.

In the reference frame of the ions, the energy density associated the ion motion, $W_{part} = n_0 T_i$, can be related to the electrostatic energy density of the wave, $W_T = n_0 E_T$, by a scaling parameter,

$$\Gamma = W_{part}/W_T, \tag{2.25}$$

where n_0 is the zero-order plasma density (assuming quasi-neutrality) and E_T is the total energy per unit charge from the spectrum of electric field fluctuations. Note that here we are only considering the energy associated with the IAT portion of the fluctuation spectrum. The energy in the low-frequency oscillations is not considered here, but may also contribute to ion energy. The relationship between the change in ion temperature as a function of wave energy change is then given by $\Delta T_i \approx \Gamma \Delta E_T$. Because of the importance of being able to obtain a scaling parameter for cathode plumes, one of the aims of this study is to measure the ion temperature and wave energy to evaluate the dependence of Γ on macroscopic properties of the plume.

CHAPTER 3

Experimental Approach

3.1 Introduction

In this chapter we discuss the experimental setup, the diagnostics, and the data analysis techniques applied to the measurements. While there were two experimental configurations used, the cathode assembly, vacuum facility, and laser system was used for each. The modifications between experiments consisted of changes to the diagnostics, and were minimal.

3.2 Facility and Cathode Assembly

The experiments were performed in a 2.6 m x 5.2 m long vacuum chamber facility at the Jet Propulsion Laboratory (JPL), California Institute of Technology. Pumping was provided by a combination of LN_2 shrouds and cryogenic pumps, with a total xenon pumping speed of $\sim$40 kL/s and a base pressure of $\sim 10^{-7}$ Torr. Convection and ionization gauges provided pressure information. The cathode discharge was powered by a 330 A Sorensen power supply. Cathode flow control was provided by an Apex flow controller up to 50 sccm. A needle valve on a bypass leg allowed for increasing the background pressure. Research grade xenon gas was used for all testing.

The testing was performed using a 100 A class hollow cathode, shown in Fig. 3.1. The emitter was constructed of LaB_6, with an inner diameter of 4.3 mm. The cathode and keeper were made of graphite and the cathode orifice plate was made of tungsten. The keeper orifice diameter is 10 mm. A 100 mm diameter, 300 mm long copper anode was located 30 mm

downstream of the keeper face and aligned concentrically with the cathode. The high power capability of the cathode required water cooling through a copper tube brazed to the anode. Tungsten sheets lined the inside of the anode to prevent copper from the anode sputtering onto the cathode. No magnetic field was applied in this test series to simplify the comparison of theory to experiment. Modeling by Ortega [40] showed the maximum field to be 50 G in the region between the cathode and keeper, and to decrease with distance downstream, so magnetic field effects are neglected in this study.

The cathode assembly (Fig. 3.2) is mounted to two orthogonal stages that provide axial and lateral translation of the assembly, while probe and optical diagnostics remained fixed. The entire setup was mounted at the end of the vacuum chamber with the anode approximately at the chamber centerline to minimize facility interactions. The position of the stages were measured using stringpots. The anode was biased with respect to the cathode via the copper tubing which are isolated from the chamber through a non-conducting sleeve. The cathode was kept at ground potential, with both the keeper and anode floating relative to the cathode. The configuration of the cathode assembly, diagnostics, and measurement domain is illustrated in Fig. 3.3.

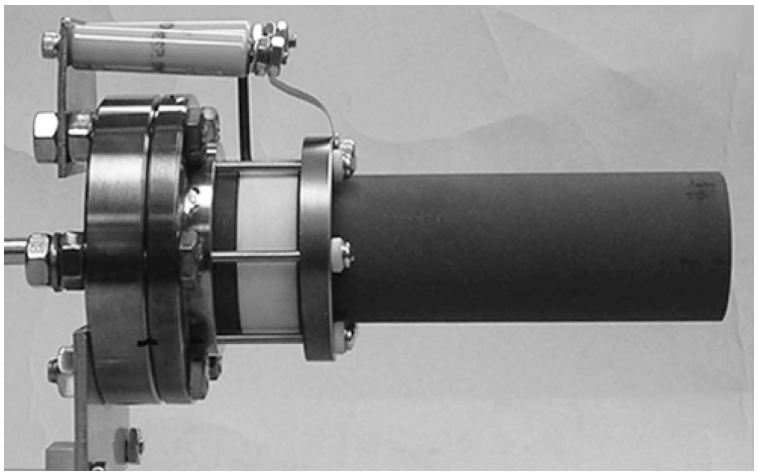

Figure 3.1: 100 A, 1/2" LaB_6 Hollow Cathode.

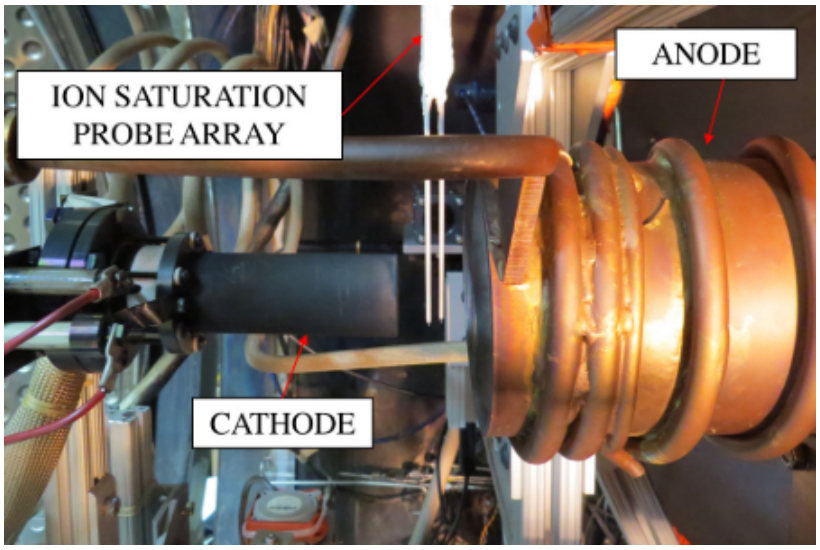

Figure 3.2: Cathode assembly [1].

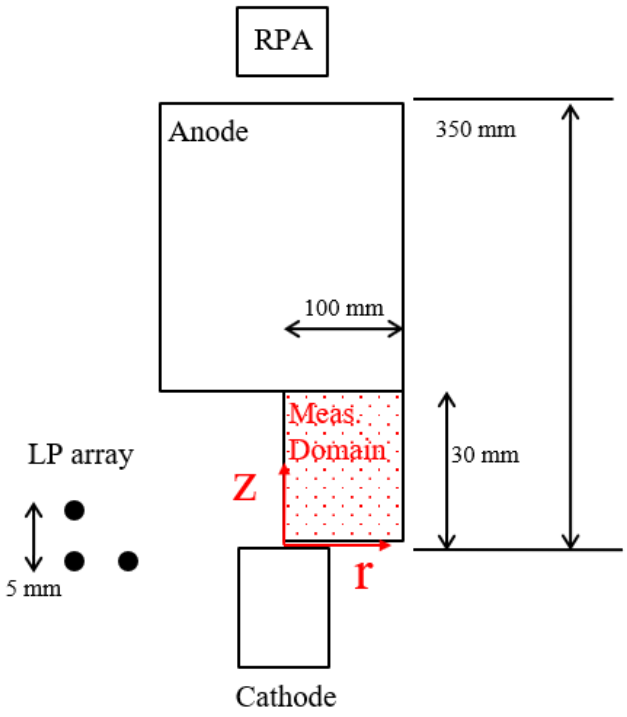

Figure 3.3: Measurement domain. LP: Langmuir probe, RPA: retarding potential analyzer. (Not to scale)

3.3 Retarding Potential Analyzer

An RPA was used to measure the IEDF in the far plume. Because it is a relatively large device (∼40 mm dia.), it cannot be used for near-plume measurements to without significantly perturbing the plasma. This diagnostic was used in this study for two reasons: 1) To verify that the operating conditions produced energetic ions as measured by other researchers using RPA's in similar operating conditions, and 2) to see if the LIF-measured ion energies matched the RPA.

The RPA was a four-grid type (see Fig. 3.4) located on the cathode centerline 350 mm downstream of the keeper face, approximately at the end of the anode, facing the cathode keeper face. From upstream to downstream, the first grid of the RPA was allowed to float; the second, electron-repelling grid was biased to -10 V with respect to ground; the third grid had a variable bias voltage applied to discriminate ion energies; the fourth grid was grounded through a Keithly 427 high impedance current amplifier. The output voltage from the amplifier provided a signal proportional to ion current to the collector with energies greater than the discriminator bias voltage. Because it is not possible to discern between singly- and multiply-charged ions it was assumed that singly-charged ions dominated the plasma at the RPA location. The discriminator voltage was provided by a DC power supply swept at 1 V increments from 0 to 100 V and measuring the time-averaged voltage at each step.

From Ref. 42, Ch. 3, the collector current is determined as follows:

$$I_c(V_{bias}) = \frac{q^2 n_i A}{m_i} \int_{eV_{bias}}^{\infty} f_{i,c}(E - e\phi_{pl}) dE, \tag{3.1}$$

where I_c is the collector current, V_{bias} is the discriminator bias, n_i is ion density, A is collector area, and $f_{i,c}(E)$ is the IEDF at the collector, and ϕ_{pl} is the local plasma potential. Accounting for the local plasma potential is necessary due to energy gained by the ions falling through the sheath to the collector. The value for ϕ_{pl} at the location of the RPA

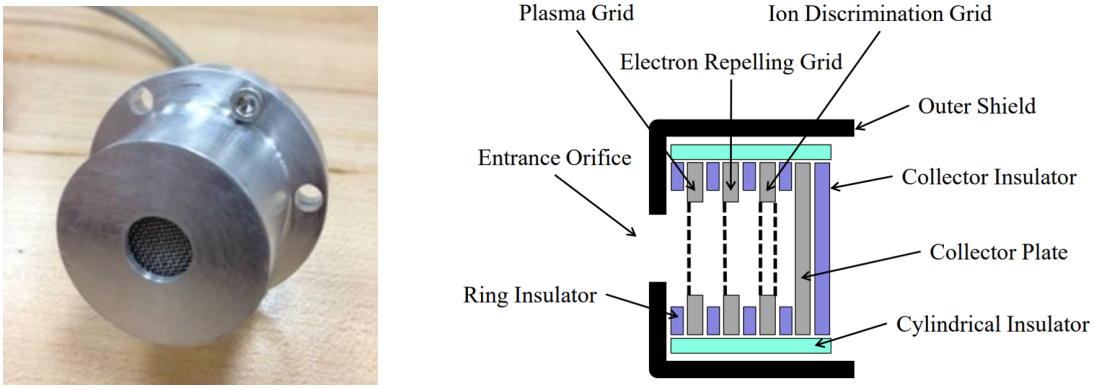

(a) RPA body

(b) RPA cross-section [41].

Figure 3.4: Retarding potential analyzer.

was not measured in these experiments, so it was approximated to be equal to the discharge voltage, V_d. Differentiating Eq. 3.1, we get:

$$-\frac{dI}{dV_{db}} = \frac{q^2 n_i A_c}{m_i} f_{i,c}(E - e\phi_{pl}) \propto f_{i,c}(E - e\phi_{pl}), \tag{3.2}$$

where the constants were ignored since we are seeking the IEDF shape function. These differentiated data were boxcar-averaged then normalized to the signal maximum for each measurement condition. Because it is possible that $\phi_{pl} < V_d$, the energies calculated could be slightly higher than calculated here.

The raw data from the RPA consists of the collector current as a function of the discriminator bias. An example of the data collected by an RPA, along with the calculated IEDF using Eq. 3.2 is shown in Fig. 3.5. The black dotted line represents the raw signal from the current amplifier normalized to its maximum value, and the black solid line is a 10-point moving average of that data. The orange dotted line is the derivative of the collector current, and the orange solid line is the 5-point moving average of the derivative. Note that there is substantial noise due to numerical differentiation, necessitating the additional averaging step. The RPA results presented in Sec. 4.3 were generated using this averaging technique. An uncertainty analysis for the RPA-derived IEDF's was not performed because this was

used a secondary diagnostic, the SNR was low, and because no measurements of the plasma potential at the RPA location was taken.

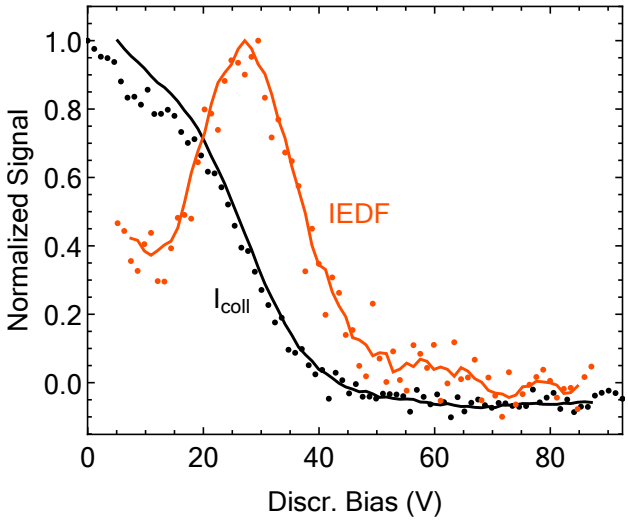

Figure 3.5: Example data from the RPA. These results were obtained on axis with the cathode operating at 130 A, 15 sscm.

3.4 Steady State Langmuir Probe Measurements

Cylindrical Langmuir probes were used to measure steady-state properties such as plasma density and electron temperature. In both experiments the probe was oriented with the probe tip coplanar with the lateral axis and orthogonal to the unit vector along the probe centerline. For the centerline experiment (Sec. 4) a single probe was used, whereas for the 2D experiment (Sec. 5) an array of three probes (Fig. 3.6) was employed to enable dispersion relation measurements. For the 2D experiment, steady-state measurements were taken on the corner probe while the other two probes were allowed to float. It should be noted that use of Langmuir probes in such a high density plasma as found in the near plumes of hollow cathodes will perturb the plasma. For example, the discharge voltage of the cathode power supply was found to vary by as much as 10% when the probe was positioned 5 mm downstream of the keeper face on the centerline.

To obtain electron temperature the probe bias was swept from -70 V to +10 V relative to ground using a Kepco bipolar operational power supply. The sweep signal was provided by a Wavetek 178 waveform synthesizer swept at 30 Hz, isolated from the Kepco supply with an operational amplifier. Current was measured through a 50 Ω resistor by an oscilloscope, averaging the trace over 50 sweeps. The +10 V maximum bias voltage was chosen to avoid excessive electron current (caused by densities exceeding 10^{19} m^{-3}) that could make the probe emissive at that sweep rate.

Figure 3.6: Langmuir probe configuration for the 1D (a) and 2D (b) [2] experiments.

3.4.1 Density

Density measurements were needed to match previous experiments at similar operating conditions, and was needed for calculations of the low-frequency cutoff of the IAT mode and plasma pressure. Steady-state values of ion saturation current in this circuit configuration were used to approximate the plasma density. Using the commonly used assumption of stationary, isotropic, cold ions, and the thin-sheath approximation[43] (since the ratio of the probe radius to the Debye length was ~ 300), we have the following relationship:

$$n = \frac{I_{sat}}{e^{-1/2} q A v_{sh}}, \tag{3.3}$$

where the ratio of density at the sheath boundary to bulk plasma, n_{sh}/n_0, is $\approx e^{-1/2}$, A is the sheath area (approximately equal to the collection area of the probe), and v_{sh} is the speed at which ions are accelerated to at the sheath edge (assumed to be the Bohm velocity $\sqrt{T_e/M_i}$).

3.4.2 Electron Temperature

Besides being generally useful to know for any plasma, the electron temperature is critical to this study because the IAT wave energy is linearly proportional to T_e, as will be shown in Eq. 3.4. The electron temperature was inferred from an exponential fit to the probe current-voltage (IV) trace[43]. The ion current was approximated using a linear fit to the I-V curve in the voltage range of ∼-40V to -10V. The electron current was determined by subtracting this fit to the ion current from the total current, and applying an exponential curve fit to $I_e(V) \approx e^{\frac{V_p - V_b}{T_e}}$ to determine T_e.

An example Langmuir probe I-V trace is shown in Fig. 3.7, with the raw data along with the fit to I_{sat} and the calculated electron current also indicated. The value for I_{sat} used in Eq. 3.3 is taken at the lowest portion of the I-V curve. Uncertainty was approximated by applying linear regression to both the linear ion saturation and exponential electron temperature portions.

3.4.3 Plasma Potential

It was found that biasing the probe >10 V resulted in excessively high electron current and the probe became emissive. This prevented electron current measurements near the electron saturation region of the I-V curve, so it was not possible to determine plasma potential using the knee of the characteristic. However, due to the importance of plasma potential in the plume an attempt was made to estimate potential by equating the electron saturation current for slow, Maxwellian electrons with the ion current for slow, isotropic ions entering

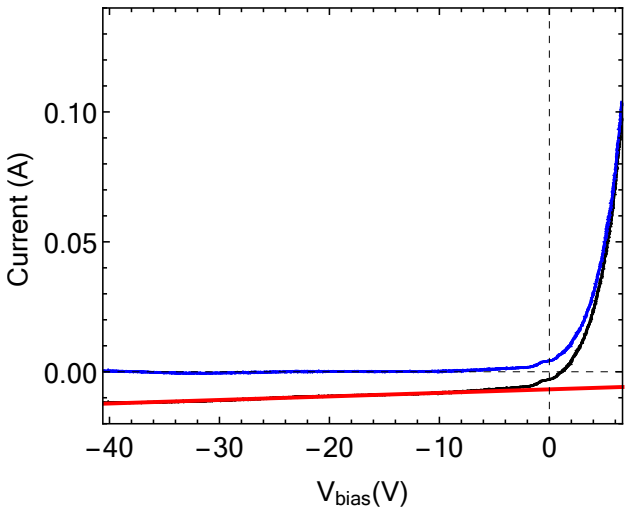

Figure 3.7: Example data from the Langmuir probe. Red is the ion saturation current fit and blue is the electron current used for determining the electron temperature.

the sheath at the Bohm velocity $v_{Bohm} = \sqrt{T_e/m_i}$, resulting in the following relationship [43]:

$$\phi_p = \phi_f - T_e \ln\left[e^{-1/2}\sqrt{\frac{2\pi m_e}{m_i}}\right], \tag{3.4}$$

where ϕ_p is the plasma potential and ϕ_f is the floating potential. Note that the previous discussion of the effects of drifts illustrate the significant uncertainty (not quantified here) inherent in this estimate of plasma potential. Nevertheless, this treatment was used to show the qualitative structure of the plasma potential. Because of the assumption of a Maxwellian electron distribution function and the difficulty of quantifying density and electron temperature uncertainties, no attempt to quantify the plasma potential uncertainty was performed. Instead, potential is evaluated qualitatively in order to get approximations for the potential well structure present in the plume.

3.5 Fluctuation Spectra and Wave Energy

The wave energy is critical to this study, and is obtained by measuring the high frequency fluctuations of ion density and relating this to the plasma potential fluctuations. To esti-

mate the wave energy in Eq. 2.24, we also need the fluctuating plasma potential amplitude spectrum up to several MHz. The potential amplitude spectrum can be measured using the cylindrical Langmuir probe array discussed earlier by applying a negative bias voltage of -27 V and measuring the voltage drop across a shunt resistor. The bias was applied using a set of batteries connected to ground to avoid any low-impedance paths to ground that could exist in a power supply, which would affect high frequency measurements. Fluctuation measurements used for wave energy calculations were only taken on the upstream probe to avoid any potential wake effects due to particle flow.

To obtain the fluctuating plasma potential power spectrum, $\widetilde{\phi}$, the following relationship holds for electrostatic perturbations of small amplitude:

$$\widetilde{\phi} = \frac{k_B T_e}{q}\left(\frac{\widetilde{n}_i}{\overline{n}_i}\right). \tag{3.5}$$

where $\widetilde{n}_i/\overline{n}_i = \widetilde{I}_{sat}/\overline{I}_{sat}$. Note that this treatment does not account for electron or ion drifts, which we have shown to be important for density and electron temperature calculations, and we have assumed that the fluctuating pressure term is dominated by density fluctuations with negligible electron temperature fluctuations.

An example of a fluctuation spectrum and the curve fit used to determine the total IAT spectral power is shown below in Figure 3.8. The IAT power is clearly defined, and the fluctuations below ∼100 kHz are ignored. This plot illustrates the inverse cascade of wave energy from high to low frequencies which is consistent with a turbulent spectrum (c.f. Ref. 44, Ch. 1). The wave energy values were not reported for cases where it was not possible to distinguish between the two modes. The uncertainty for wave energy, U_{E_T}, is determined by uncertainty propagation using Eq. 3.4.

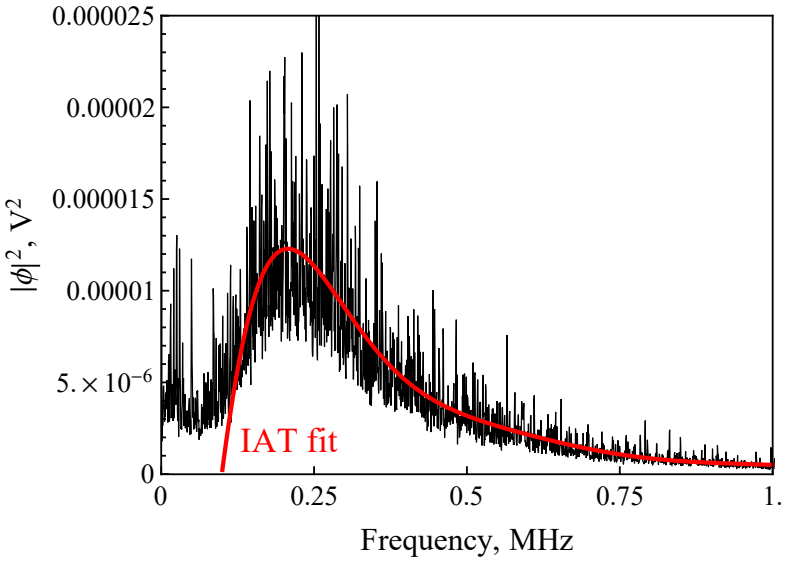

Figure 3.8: Example of raw plasma potential amplitude spectrum for the 130 A, 10 sccm, operating condition at z = 16 mm.

3.6 Wave Dispersion Relation

The dispersion relation serves two primary purposes: it allows for the determination of the modes present in the plasma, and it enables the calculation of the group velocity of ion acoustic waves. This can be obtained by using a pair of fixed probes biased to collect ion saturation current. The dispersion relation, $k(\omega)$, is determined by using the cross-phase of the two signals through the approach described by Beall [45] and Jorns [26], which is briefly described here.

For any two signals, the dispersion relation between them can be determined by taking the Fourier transform $\mathcal{F}$ of each and using the following relationship:

$$k(\omega) = \frac{1}{\Delta x} tan^{-1}\left[\frac{\mathrm{Im}(\mathcal{F}[\phi_2(t)]\mathcal{F}^*[\phi_1(t)])}{\mathrm{Re}(\mathcal{F}[\phi_2(t)]\mathcal{F}^*[\phi_1(t)])}\right]. \tag{3.6}$$

where Δx is the probe separation distance, and the fluctuations in plasma potential are represented in the Eikonal approximation as $\phi(t) = \sum_\omega \phi(\omega) e^{i[k(\omega)x - \omega t]}$. To improve the correlation with noisy signals, the Beall approach involves averaging over a number of time

signals using a histogram technique, binning the k values and weighting them according to the following:

$$S(\omega, k) = \frac{1}{M} \sum_{j=1}^{M} I_{0,\Delta k}[k - k^j(\omega)] \frac{1}{2} [P_1^{(j)}(\omega) + P_2^{(j)}(\omega)], \tag{3.7}$$

where M is the number of time samples, j is the run number, $P_1^{(j)}$ and $P_2^{(j)}$ are the power spectra of the two signals. The function $I(x)$ is used to ignore wavenumbers not discernible based on the probe separation distance, and is defined as

$$I_{0,\Delta k}(x) = \begin{cases} 1, & |k - k^j(\omega)| < \Delta k \\ 0, & |k - k^j(\omega)| > \Delta k. \end{cases} \tag{3.8}$$

where Δk is the width of the bin. Performing this analysis on both sets of probes, oriented parallel and perpendicular to the cathode axis, gives the dispersion relation in each direction. The group velocity, $\mathbf{v}_g = \nabla_k \omega_r$, can then be determined by measuring the slopes in the dispersion relations taken in the axial and radial directions.

For each location, both axial and radial dispersion relations were evaluated, and the frequency range over which both showed a clear linear IAT trend was identified. All data sets of $S(\omega, k)$ in that range were evaluated, the first moment of $S(k)$ for each ω was determined and then used to fit a line, the slope of which is used to determine the wavenumber ratio as follows:

$$\frac{k_z}{k_r} = \frac{m_r}{m_z}, \tag{3.9}$$

where m_z and m_r are the slopes of the axial and radial dispersion relations, respectively. The angle of the wave is given by $\Theta = \tan^{-1} k_z/k_r$. It can be shown that the magnitude the

group velocity vector can be determined by the slopes by:

$$|\mathbf{v}_g| = \frac{1}{\left[(\frac{1}{m_z})^2 + (\frac{1}{m_r})^2\right]^{1/2}}. \tag{3.10}$$

An example of the axial dispersion plot obtained using the Beall techniques is shown in Fig. 3.9, illustrating the linear dispersion characteristic of ion acoustic waves, along with the analysis domain (red box) and best fit (black dotted line). The plots shown have been phase-wrapped (i.e. repeated for higher k's) to make it easier to show the linearity and to fit lines to the IAT portion. This is denoted by the region to the left of the dashed line in the plots. As will be discussed in Sec. 5.5, not all of the plots were as easy as this example to fit a line to the ion acoustic portion of the dispersion relation. Some plots showed evidence of low-frequency modes, suspected to ionization instabilities, and some showed a gradual increase in the slope of $\omega(k)$ for higher frequencies. Additionally, data collected in the wings of the plume had a low SNR. Because of this, it was not possible to find good fits to the IAT portion for both plots, in which case the wave vector is not reported.

The uncertainties in the slopes of each dispersion relation, U_{m_z} and U_{m_r}, were determined by weighting the (ω, k) point at each ω inversely proportional to the variance of $S(k)$ for each frequency during the line fit. The uncertainty of the wave vector direction, that is, the uncertainty in the angle $\Theta_{\mathbf{k}}$, defined as the angle between radial unit vector and axial unit vector, $\Theta_{\mathbf{k}} = \tan^{-1}\frac{|k_z|}{|k_r|}$, is as follows:

$$U_{\Theta_{\mathbf{k}}} = \left[\left(\frac{\partial\Theta_{\mathbf{k}}}{\partial m_z}U_{m_z}\right)^2 + \left(\frac{\partial\Theta_{\mathbf{k}}}{\partial m_r}U_{m_r}\right)^2\right]^{1/2}, \tag{3.11}$$

where the derivatives are $\frac{\partial\Theta_{\mathbf{k}}}{\partial m_z} = \frac{m_r}{m_z^2+m_z^2}$ and $\frac{\partial\Theta}{\partial m_r} = \frac{-m_z}{m_z^2+m_z^2}$.

To verify that the plasma wake from the upstream probe did not affect the fluctuation measurements of the downstream probe, the ion saturation currents were compared along

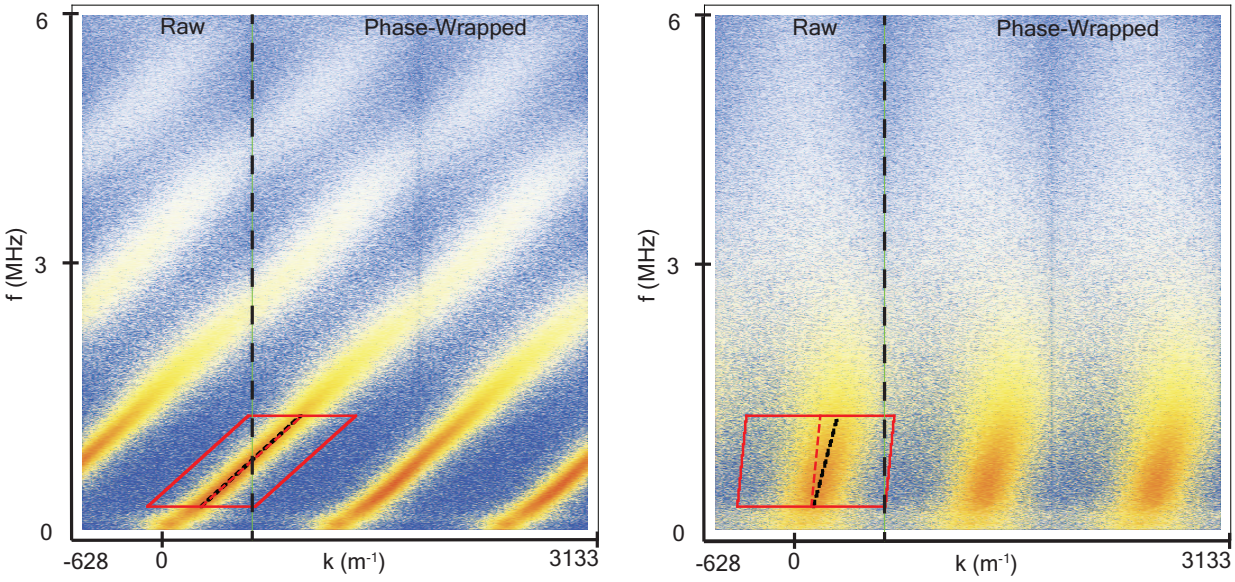

Figure 3.9: Example dispersion relations for 160A, 15sccm. The axial plot is on the left and the radial plot is on the right.

the centerline. It was found that the downstream probe measurement was within 5% of the upstream probe for $z \geq 5$ mm, indicating that the wake of the upstream probe did not affect at least the steady-state density measurements.

3.7 Laser-induced Fluorescence

The LIF technique system used here provides the IVDF of singly-charged xenon ions in the cathode plume. It consists of a laser optics table, fiber optic cables and fiber optic feedthroughs to transfer the light to and from the test setup inside the vacuum chamber, and optics inside the chamber focusing light to the target region and collecting the fluorescence emission. This section will describe the fundamentals of the technique and the hardware used.

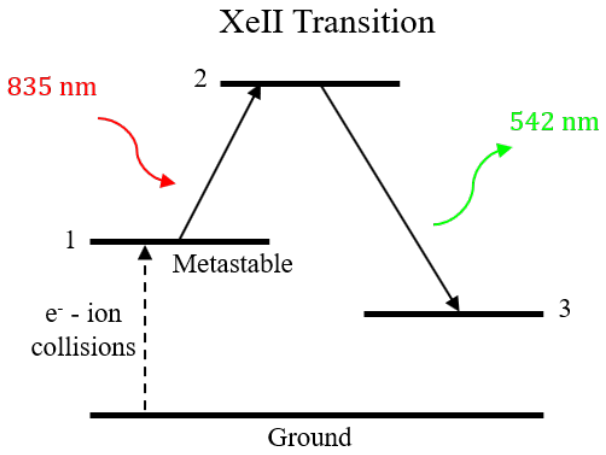

Figure 3.10: LIF scheme for the XeII $5d^2_{7/2} \rightarrow 6d^2_{5/2}$ transition.

3.7.1 Technique Description

This technique involves measuring the Doppler shift of an absorption line of singly-ionized xenon, using the relationship $v_i = c\Delta f/f_0$, where v_i is ion velocity, Δf is the difference between the laser frequency and the frequency of the absorption transition in the rest frame of the ions, f_0, and c is the speed of light. Due to its high transition probability and accessibility using diode lasers, the XeII $5d^2F_{7/2} \rightarrow 6d_2^{5/2}$ transition was excited using 834.953 nm (vacuum), resulting in fluorescence at 542.066 nm (vacuum) [46, 47]. The LIF scheme is non-perturbing if high laser intensities are avoided, and is therefore preferable to physical probes such as an RPA which indirectly provide ion energy information but large size perturbs the plasma, making them appropriate only for use in the far plume. Another advantage of LIF is that it can be used to measure a single species whereas interpretation of the RPA signal requires knowledge of the relative proportion of the species being measured relative to the other charged ionic species. The spatial resolution using LIF is also high, limited only by the optical collection spot size.

The first use of LIF on hollow cathode plumes intended for propulsion applications was by Williams et al.[48], who investigated ion temperature and drift velocities of a low current (<20 A) hollow cathode in both plume and spot modes of operation. Axial ion temperature

generally decreased with distance downstream, and he observed ion energies in excess of the discharge voltage as well as 15-20 eV ions streaming back towards the cathode at off-axis locations. More recent centerline LIF measurements, also for low discharge currents (<20 A) were taken by Georgin in the plume of the H6 Hall thruster[49]. He measured a similar behavior of drift velocity as Williams but found ion temperature to increase with distance downstream up to 1 eV. These differences might be explained by the different environments and operating conditions.

3.7.2 Equipment

A schematic of the laser optics table is shown in Fig. 3.11. The laser is a continuous-wave TLB-6700 Velocity diode seed laser coupled into a TA-7616 tapered amplifier, both by New Focus. The maximum power from the tapered amplifier is 550 mW. Wavelength measurement is provided by a High Finesse WS7 wavelength meter with 60 MHz resolution. The injection beam is modulated at 3 kHz using an optical chopper and coupled to 50 μm step-index optical fiber. The injection fiber feedthrough used initially was an Accuglass 62.5 μm type with connections, but later was changed to an Avantes custom 50 μm with FC/PC connections to improve transmission and consistency (SMA connections are only optimized for a single clocking). Inside the chamber a 62.5 μm injection beam fibers were coupled to 25 mm injection optics that provided a 2 mm spot size at a 1 m and 0.5 m working distances for the axial and radial beams, respectively. No polarizers were used on the injection optics due to the insignificant broadening effect (<1%) expected due to the Zeeman splitting from the self-magnetic field. The maximum average power delivered to the target was 120 mW, but for the earlier experiments using the SMA-type feedthrough the power was ∼90 mW. Figure 3.12 shows the optical configuration at the cathode assembly.

The collection optics consist of 25 mm dia. lenses with 75-125 mm focal lengths. Various collection optic configurations were implemented. For the centerline experiment, two optics were used, one facing upstream and the other downstream, in order to interrogate the plume

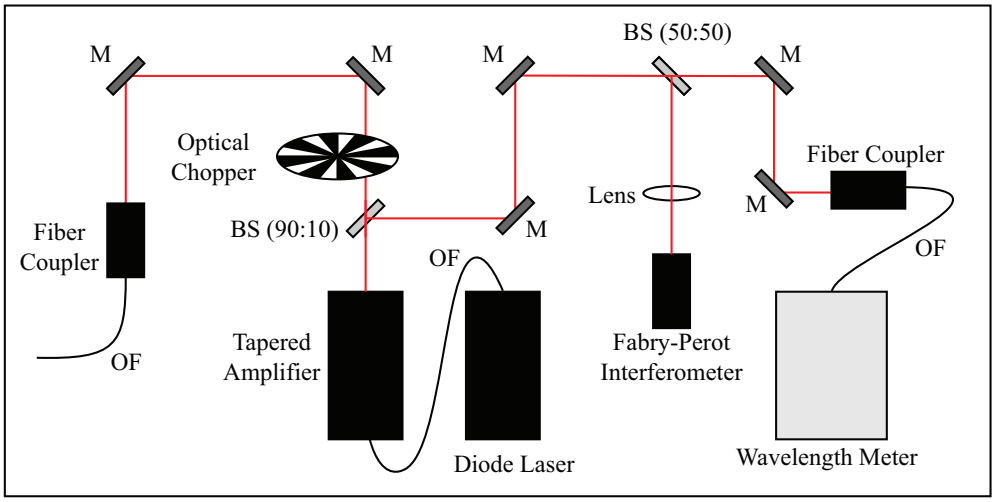

Figure 3.11: LIF optical bench (M: mirror, BS: beam splitter, OF: optical fiber).

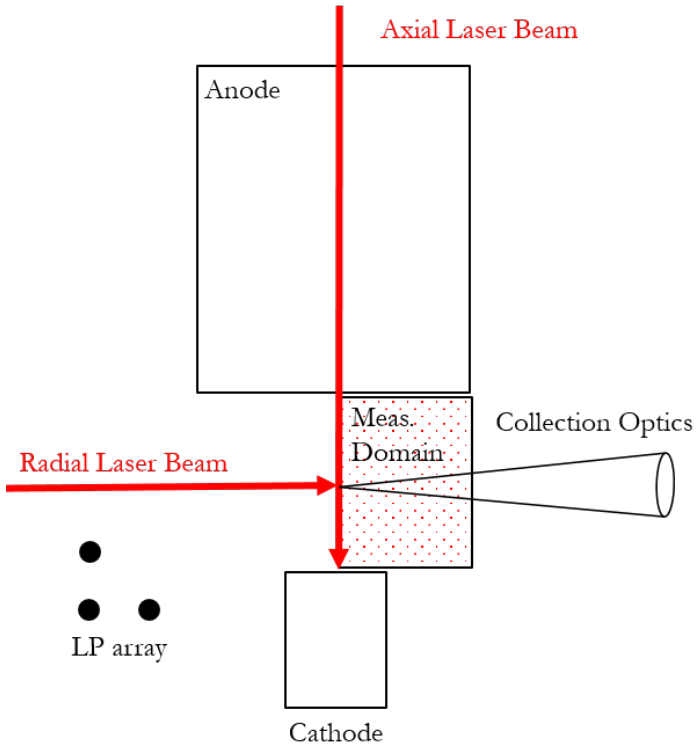

Figure 3.12: LIF measurement domain for the 2D experiment. LP: Langmuir probe, RPA: retarding potential analyzer. (Not drawn to scale)

from cathode to anode. For the 2D experiment, only a single collection optic was used, which was oriented orthogonally to the cathode axis. This was chosen to minimize the

possibility of reflected fluorescence light from inside the anode being collected, which could cause artifacts in the signal. This latter configuration is the one shown in Fig. 3.12. The spot sizes were 0.6-1.2 mm. The collected light was focused to a 600 μm fiber connected to a 600 um Thorlabs fiber feedthrough, to an external 600 μm fiber, and finally to a Hamamatsu H10721-01 photo-multiplier tube (PMT) using a bandpass filter centered at 543 nm with 11 nm FWHM acceptance. Current output from the PMT was directed to a Keithley Model 427 current amplifier, which output voltage to a Stanford Research Systems SR830 lock-in amplifier. The optical chopper was also connected to the SR830, which output the phase-sensitive detection amplified PMT signal to a National Instruments DAQ card.

Phase-sensitive detection is needed for this technique because, even at laser intensities that would saturate the transition, the fluorescence light intensity is still several orders of magnitude lower than the background emission at that wavelength. The lock-in amplifier effectively reduces this noise by using the known optical chopping frequency as a reference, Fourier-transforming the signal from the PMT, and discriminating all signals not occurring at the reference frequency within a certain bandwidth. The full assembly, including both probe and optical diagnostics, is shown in Fig. 3.13.

3.7.3 Data Analysis

Many of the LIF signals showed two peaks, referred to here as the "slow" and "fast" ion populations, with the slow population drift nearly zero. An example of the signal obtained from LIF is shown in Fig. 4.6 for the 70 A, 10 sccm operating condition at the 12 mm location. At the keeper orifice (z = 0 mm) is can be approximated by a single Gaussian curve fit, and corresponds to an ion temperature of $\sim$1 eV. For these signals the two populations were deconvolved using a dual Gaussian curve fit:

$$f_i(v) = n_{01}\sqrt{\frac{m_i}{2\pi T_{i1}}}e^{-m_i(v-V_{i1})^2/2T_{i1}} + n_{02}\sqrt{\frac{m_i}{2\pi T_{i2}}}e^{-m_i(v-V_{i2})^2/2T_{i2}}, \tag{3.12}$$

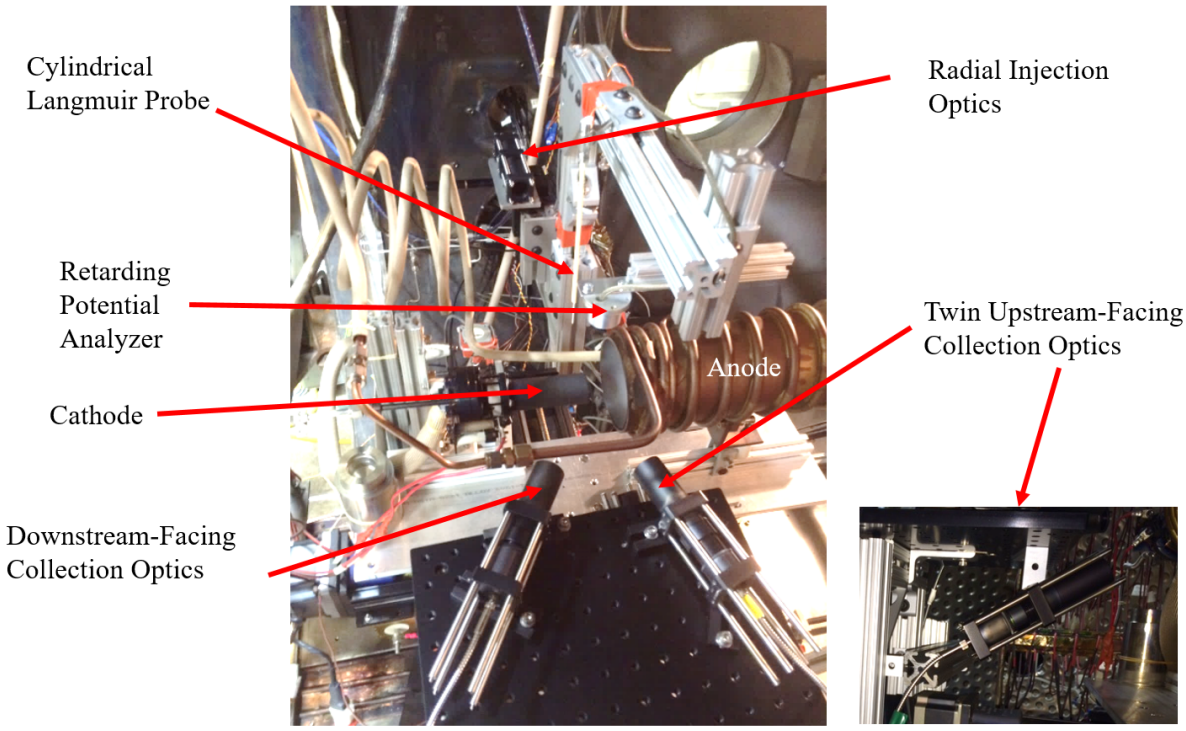

Figure 3.13: Diagnostics configuration in the 2D configuration. Note that here the RPA was oriented to collect radial IEDF measurements, and the orthogonally oriented collection optic was mounted underneath the small optics board, facing up towards the plume.

where n_{01} and n_{02} are the densities of the two ion populations of the slow and fast populations, respectively, and V_{i1} and V_{i2} are the most probable velocities. The angle of the ion drift velocity vector is given by $\Theta_i = \tan^{-1}|V_z|/|V_r|$, where the drift velocities are the most probable velocities of the Gaussian curve fit to the fast population.

3.7.4 Line Broadening

The absorption spectrum measured by the fluorescence of the above transition is can be affected by many factors. These effects include factors intrinsic to the species such as the fundamental uncertainty in the energy levels of the species, the number and type of isotopes, and quantum coupling of spin and angular momentum within the atom. It can also depend

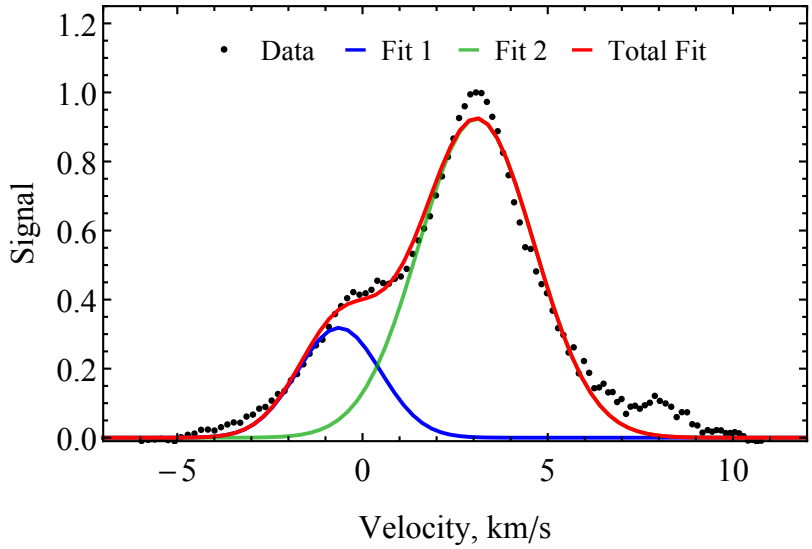

Figure 3.14: Curve fits applied to the 70 A, 10 sccm IVDF at z = 12 mm. Fit 1 refers to the non-drifting population and Fit 2 to the drifting population. Total Fit is the double Gaussian curve fit. The raw data has had a 9 point boxcar average applied.

on factors such as the velocity distribution of the species and interactions with the species and electric or magnetic fields or with the laser causing the transition. To determine the true velocity distribution function it must be deconvolved from the effects of these mechanisms, but in many cases the spectral broadening can be ignored. Here will discuss some of the potential broadening mechanisms and they are accounted for in the data analysis.

3.7.4.1 Zeeman Splitting

The effect of the magnetic field on line broadening, known as the Zeeman effect, involves interaction between the magnetic field and the energy levels of the atom, leading to splitting of the lines. Using a semi-empirical model from Huang [50], the broadening is $\Delta\nu = \alpha B$, where α is a constant empirically determined to be 2.7 MHz/G and B is the magnetic field strength in Gauss. Simulations of the current density [40] show that at 140 A discharge current there is a <5 G magnetic field in the region of the plume where LIF is performed. This results in a negligible line broadening for a 1 eV ion population, and so is neglected.

3.7.4.2 Hyperfine Splitting

Hyperfine splitting is a result of two effects. The first is the interaction between the nuclear electric and magnetic moments with the electronic angular momentum, and the second is based on minute differences in the massess and electron orbital shapes due to the different isotopes of a species. The net effect is to cause multiple absorption lines of varying strengths. The 835 nm XeII transition involves hyperfine splitting constants that are not known, so it is not possible to theoretically deconvolve the lineshape. Work by Huang, using an optogalvanic cell with low temperature, partially ionized XeII using the same transition we use, showed that the effect of the hyperfine splitting could be described by a Gaussian distribution with $\Delta\nu = 440$ MHz [51], resulting in an uncertainty of <10% for a 1 eV population, and so it too is neglected.

3.7.4.3 Saturation Broadening

Saturation broadening (also called power broadening), is the nonlinear response of the observed fluorescence emission relative to the incident laser power. When this occurs, there is an artificial broadening of the measured lineshape. Considering the simplified two-energy level model, this effect occurs when the rate of stimulated de-excitation becomes an appreciable fraction of the rate of stimulated excitation of the metastable level. The effect of this is that the number of ions in the upper energy level state is no longer linearly related to the intensity of the laser. If we assume the Doppler and saturation broadening are the only significant broadening terms, then the fluorescence signal, $S(\nu)$, is a convolution of the Doppler and natural broadening lineshapes. For a thermalized ion population, the Doppler lineshape is a Gaussian:

$$G(\nu) = \frac{1}{\sqrt{2\pi\sigma^2}} e^{-\frac{(v-\mu)^2}{2\sigma^2}} \tag{3.13}$$

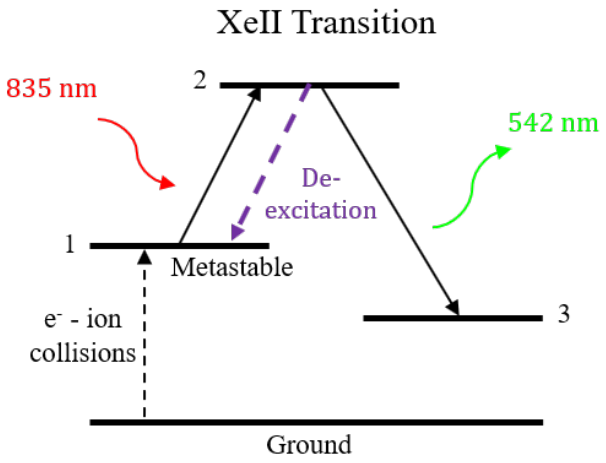

Figure 3.15: Simplified energy level diagram illustrating the pathways of electron-ion collisional excitation and laser-induced de-excitation to alter the population of the metastable level as well as the fluorescence signal.

where σ is the variance and μ is the mean. The lineshape due to natural broadening, denoted here as $L(\nu)$, is a Lorentzian:

$$L(\nu) = \frac{1}{\pi} \frac{\frac{1}{2}\Delta\nu_L}{(v-\mu)^2 + (\frac{1}{2}\Delta\nu_L)^2}, \tag{3.14}$$

The convolution of a Gaussian and Lorentzian is a Voigt distribution, $V(v|\sigma, \Delta\nu_L) = G(v) \otimes L(v)$. The proper way to deconvolve a lineshape would then be to first fit a Voigt profile to the data and then deconvolve it to obtain the Doppler profile, and from that extract the desired mean and variance of that distribution. However, this process is not straightforward or fast for distributions that have multiple peaks and for low SNR. Therefore, in this study we estimate the broadening of a Gaussian distribution expected for the amount of saturation estimated, and treat that broadening as a temperature uncertainty.

To estimate the broadening for a given laser intensity, we take the approach taken by Chaplin [52]. The fluorescence signal is proportional to the density of level 2 in Fig. 3.15, so we seek this density by solving a set of rate equations accounting for the various transitions of this two-level system. The details are given in the reference, but the result is that the

overall density at a given Doppler-shifted frequency is

$$n_2(v,\nu) = \left[\frac{\frac{g_2}{g_1} I_\nu L(\nu;\nu_0,v)}{(1+\frac{g_1}{g_2}) I_\nu L(\nu;\nu_0,v) + \frac{8\pi h\nu_0^3}{c^2 L(\nu;\nu_0,v)}}\right] n_t(v), \tag{3.15}$$

where g represents the degeneracy of the transition, h is Planck's constant, and c is the speed of light. By integrating over all velocities we get upper level density (which is proportional to the ground state density) as a function of laser frequency:

$$n_2(\nu) = \int_{-\infty}^{\infty} n_2(v,\nu) dv \tag{3.16}$$

For a Doppler broadened (Gaussian) distribution this equation gives us the lineshape expected once the effect of saturation broadening is taken into account. We then can estimate relative change in ion temperature. Note that the saturation intensity is traditionally defined as the second term in the denominator in Eq. 3.15:

$$I_{sat} \equiv \left(\frac{g_1}{g_1+g_2}\right)\left(\frac{2\pi\gamma h\nu_0^3}{c^2}\right) \tag{3.17}$$

Using values from the NIST database, where $g_1 = 8$, $g_2 = 6$, $\gamma = A_{21} \approx 10^8$ we calculate a saturation intensity of $122 W/m^2$ for this transition. To first order, the linewidth of a Voigt profile is related to the linewidths of the constituent Gaussian and Lorentzian profiles by $\Delta\nu_L = \sqrt{\Delta\nu_L^2/4 + \Delta\nu_G^2}$, where $\Delta\nu_L = 2A_{21} \approx 2e10^{-8} s^{-1}$. For cases such as ours where $\Delta\nu_G \gg \Delta\nu_L$, then $\Delta\nu_V \approx \Delta\nu_G$. That is, by fitting a Gaussian to the broadened lineshape we can estimate $\Delta\nu_V$, which can then be related to an "'effective"' temperature by $T_{i,eff} = m_i\lambda_0^2\Delta\nu_V^2/8\ln(2)$. We then numerically solve for $n_2(\nu)$ which, when broadened by the amount prescribed by the laser intensity, results in the measured $T_{i,eff}$.

Analysis of the two-level model indicates that this was moderately saturated, with $I_\nu/I_{sat} \sim 1200$ (considered moderate because the effect of saturation is logarithmic with the ratio I_ν/I_{sat}). For example, for 1 eV lineshape this corresponds to a relative broadening,

i.e. $(T_{i,eff} - T_i)/T_i \approx 25\%$, but for ions heated to 5 eV this broadening is $< 10\%$. We therefore find that the uncertainty due to saturation broadening is most significant in the first 10 mm downstream of the keeper. This uncertainty is significant to this study only in the determination of the scaling factor shown in Eq. 2.25. It does not affect the general trends from the study of this scaling as discussed in Sec. 4.6.

One of the major assumptions of the two-level model is that transitions from or two other energy levels are at low enough frequencies that they can be neglected relative to the laser-induced excitation and de-excitation rates. Here we show that this may not be valid. The two pathways considered are quenching from ion-atom collisions and electron-excitation collisions. The rate for ion-atom quenching is given by $\nu_q = n_g \sigma v_i$, where n_g is the neutral gas density, σ is the quenching cross-section, and v_i is the ion velocity. Assuming $n_g = 10^{-20} m^{-3}$, $\sigma \sim 10^{-19} m^2$, and $v_i = V_i \sim 2km/s$, the quenching rate is then $\nu_q \sim 10^{-4}$, which is much less than $A_{21} = 10^6 s^{-1}$. Electron-ion excitation, however, occurs at a higher rate. The rate is given by $\nu_{exc} = n_e \langle \sigma v_e \rangle$, and with $n_e = 10^{19} m^{-3}$ and $\langle \sigma v_e \rangle = 10^{-13} m^{-3} s^{-1}$, we get a rate of $\nu_{exc} \sim 10^7$, which is an order of magnitude higher than A_{21}, meaning that we should consider population of the two energy levels by electron collisions to have an accurate model. This analysis is meant to illustrate that at the high plasma densities encountered in the near plume of hollow cathodes, the simple two level model may need modifications, and it would be beneficial to perform a saturation study in order to determine the limits of this model, and to reduce the uncertainty in the saturation broadening estimation used here.

3.7.5 Uncertainty Analysis

Table 3.1 lists the various line-broadening mechanisms, the effect on the FWHM, $\Delta f_{1/2}$ of a Maxwellian distribution, and the corresponding uncertainty in T_i based on a measured lineshape corresponding to 1 eV. From these estimates, the only relevant sources of line broadening in this plasma are due to hyperfine splitting and saturation broadening, with the latter being the most concerning.

Table 3.1: Line Broadening Estimates.

Broadening Source	$\Delta f_{1/2}$ [MHz]	ΔT_i Uncertainty
Wavelength Meter	60	0.1%
Laser Linewidth	0.2	∼0%
Natural	17	∼0%
Transit-time	1.8	∼0%
Zeeman Effect	13	<10%
Stark Effect	20	∼0%
Hyperfine Splitting	440	<10%
Saturation	730-1000	10-60%

The primary uncertainties in the derived ion properties are due to the deconvolution procedure and line broadening summarized in Table 3.1 (note that we did not consider pressure broadening). Approaching the uncertainty analysis conservatively, we therefore treat both saturation broadening and curve fit uncertainties as equally probable, and calculate the total uncertainty as the RMS of the two. This applies to the ion temperature and velocity, and in this study we focus on these parameters for the fast ion population only.

The final uncertainty discussed here is that of the drift direction, Θ_i, which is as follows:

$$U_{\Theta_i} = \left[\left(\frac{\partial \Theta_i}{\partial V_z} U_{V_z} \right)^2 + \left(\frac{\partial \Theta_i}{\partial V_r} U_{V_r} \right)^2 \right]^{1/2}, \tag{3.18}$$

where the derivatives are $\frac{\partial \Theta_i}{\partial V_z} = \frac{V_r}{V_z^2+V_z^2}$ and $\frac{\partial \Theta_i}{\partial V_r} = \frac{-V_z}{V_z^2+V_z^2}$, and the uncertainties in the velocities, which are due solely to curve-fitting (ignoring the very low uncertainty in wavelength measurement), are U_{V_z} and U_{V_r}.

3.7.6 LIF Operation

Prior to closing the test setup, the collection optics were all aligned to the same reference mark. Because they were all mounted to the same rigid structure, and because they were close to the collection volume and each other, they only required alignment prior to pumping down the chamber. However, the injection optics, because they were farther away from the target volume, required alignment at the beginning of each LIF experiment. The injection

optics tubes were mounted to motorized translation stages providing vertical and lateral adjustment (Thorlabs MT1-Z8). Once the cathode was at thermal steady-state at ∼60 A of discharge current, the following alignment procedure was performed: 1) passing green light (532 nm) through the collection optics, illuminating the face of the keeper; 2) moving the cathode axially until at the collection beam waist; 3) passing red (670 nm) light through the injection optics to illuminate the keeper face; and 4) adjusting the alignment of the injection optics to center the injection beam with the collection beam. The wavelengths used were chosen based on minimum differences in focal length of the given optics relative to the wavelengths used in the experiment, since achromatic doublets (which provide a nearly constant focal length over a given wavelength range) were not always used. Once the collection and injection beams were aligned, the cathode was moved until the injection beam coincided with the outer edge of the keeper in order to obtain a reference location for the assembly relative to the collection volume using the stringpots.

For LIF signal acquisition, a combination of setting of the PMT voltage, lock-in time constant and sensitivity, and current amplifier gain were found to maximize SNR for a given wavelength. The laser wavelength was controlled to discrete values with a dwell time determined by the lock-in time constant. The wavelength scan range was set to obtain ∼100 data points for regions of high SNR, and ∼200-300 points for regions of low SNR, attempting to cover the full IVDF with margin on the wings to get a zero signal reference and SNR value. For regions with low SNR, initially we attempted to improve the signal adjusting the injection optic alignment, but it was found that in some cases this the signal would increase with increasing misalignment due to the emission strength of the new collection volume (such as a higher metastable population caused by higher T_e or n_e. Therefore, this approach was discontinued and the alignment set just before the experiment was left as is throughout. For switching between collection optics, IVDF's were obtained at the same location (typically 15 mm downstream) to verify the collection volumes were equivalent.

CHAPTER 4

Measurements Along the Plume Centerline

4.1 Introduction

The centerline experiment was performed to investigate the correlation between wave energy and ion heating. Ion heating as a function of discharge current and cathode flow rate were parametrically evaluated for five operating conditions, shown in Table 4.1. IV curves for the three flow rates are shown in Fig. 4.1. To match the plasma conditions previously performed on this cathode design at JPL [27] (since the plasma properties were extensively measured), background pressure was controlled to 2.2×10^{-4} Torr by flowing xenon through a leak valve. As was shown by Jorns[21], the discharge voltage is correlated to IAT wave energy and, therefore, ion temperature. With this in mind, the discharge current-discharge voltage (IV) curves for this cathode were obtained prior to any other probing.

Table 4.1: Operating Conditions for the centerline study. Voltage and currents shown are accurate to within 1 V and 1 A, respectively. Note that the standard used for flow rate is 25°C and 760 Torr.

Discharge Current [A]	Discharge Voltage [V]	Flow Rate [sccm]
70	15.4	10
100	17.4	10
130	21.0	10
130	18.2	15
130	16.8	20

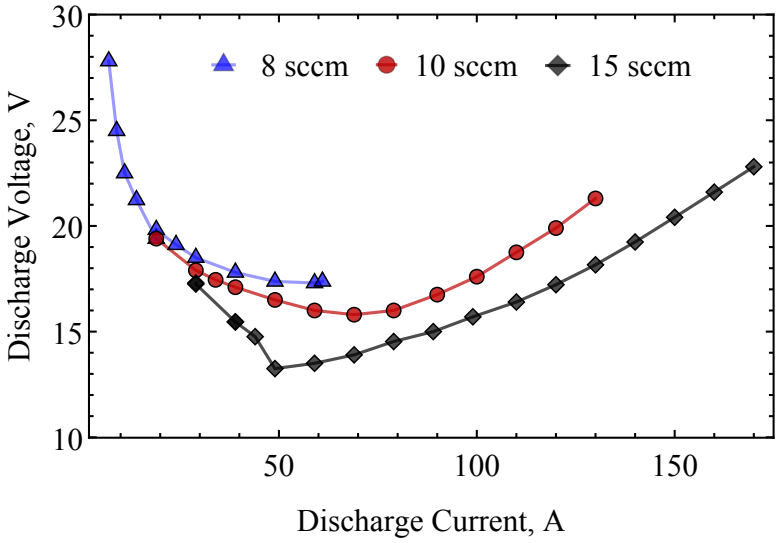

Figure 4.1: Discharge voltage vs. discharge current for various flow rates .

4.2 Steady-State Langmuir Probe Measurements

Because both the Langmuir probe and optical diagnostics were fixed, probe measurements were taken separately from LIF measurements. To verify the global plasma conditions were similar the discharge voltages were monitored for agreement. Plasma density, shown in Fig. 4.2, was determined using Eq. 3.3. Uncertainties are not presented because the dominant uncertainty, caused by the high particle drifts and discussed in Sec. 4.7, are beyond the scope of this work to estimate. A first order calculation based on the plasma conditions measured during the experiment compares to these values to within a factor of 2.

Electron temperature, which is needed to determine IAT wave energy per Eqs. 2.24, is shown in Fig. 4.3. Values of 2-3 eV were found, consistent with values reported by Jorns[21]. In general the temperature increases with discharge current and decreases with higher neutral gas flow. The measurements for the 70 A case at z=18 and 20 mm locations are absent due to data integrity concerns. An uncertainty analysis based solely on curve fitting shows an uncertainty $< 1\%$, with the following caveats: data was only fitted on a small region along the lower portion of the exponential, a linear fit was used for subtraction of the ion saturation

current, and no flow effects were considered. As with density, particle drift effects are thought to be the dominant source of uncertainty.

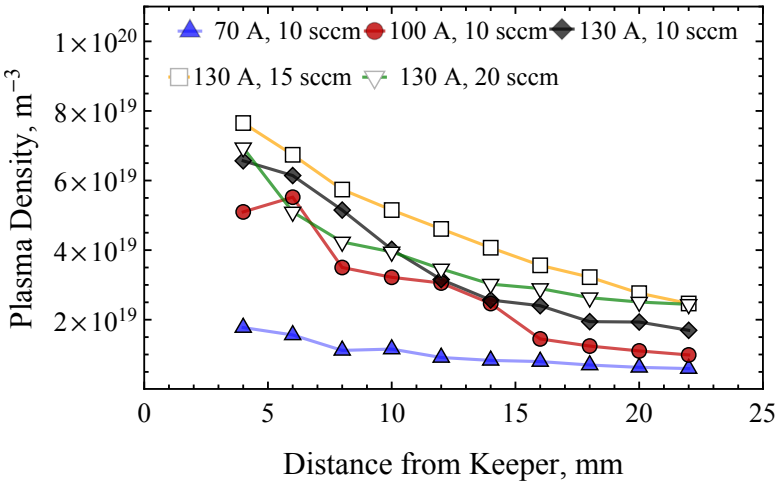

Figure 4.2: Plasma density based on ion saturation current measurements from a cylindrical Langmuir probe.

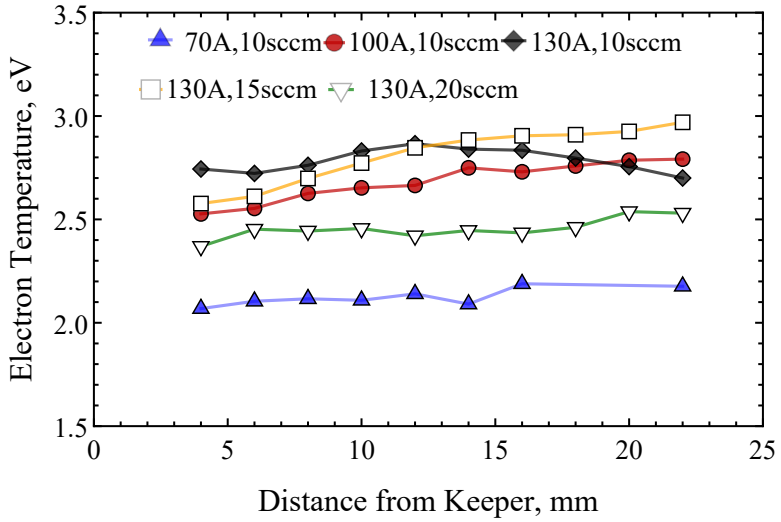

Figure 4.3: Electron temperature vs. distance downstream of the cathode keeper face.

4.3 RPA Measurements

The ion energy distribution function measurements obtained with the RPA in the far plume on-axis are shown in Fig. 4.4. The change from 70 A to 100 A at 10 sccm produced no appreciable change to the IEDF, but increasing current to 130 A resulted in an increase in maximum energy by ∼10 eV, with the most probable energy relatively unchanged. Note that the hump in the 130 A, 10 sccm signal around 60 eV is believed to be due to the numerical differentiation performed on raw data with low signal-to-noise ratio. All cases showed maximum energies greater than the ∼20 V discharge voltage. The effect of increasing flow rate at 130 A was more apparent, having the opposite effect to increasing current: the mean energy decreases as does the maximum. This follows the trends of Ref. 21.

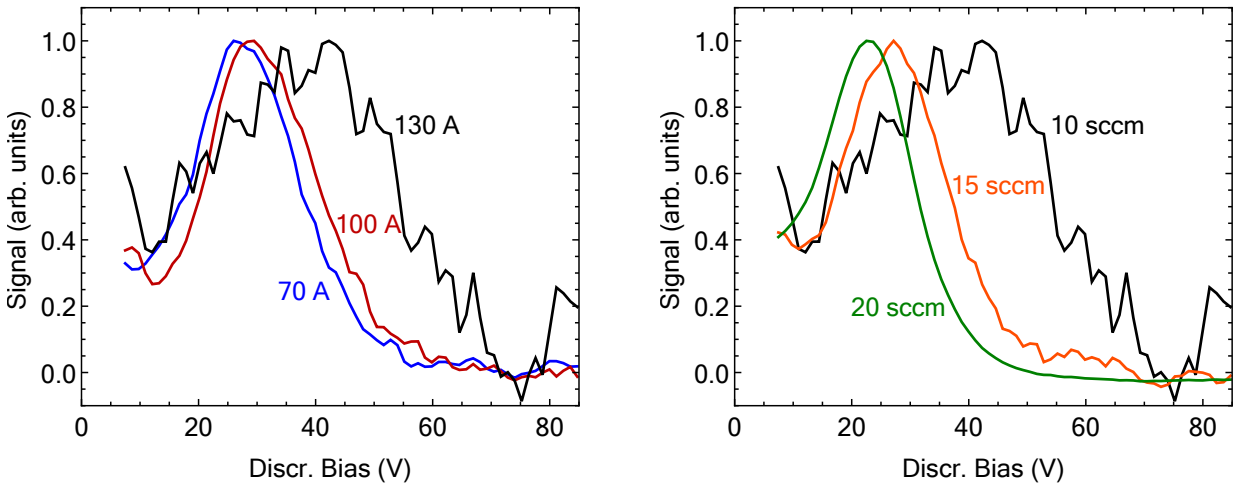

(a) Variable current at 15 sccm flow rate.

(b) Variable flow rate at 130 A discharge current.

Figure 4.4: Axial ion energy distribution functions taken with the RPA. The signals are each normalized to its maximum value.

4.4 LIF Measurements

4.4.1 Lineshape Observations

The LIF results for the ion lineshapes show a Gaussian distribution near the keeper orifice with temperature of ~ 1 eV. This is consistent with classical heating mechanisms inside the cathode, presumed to be caused by a cascade of ions falling through wall sheath potentials, undergoing charge-exchange collisions, and being resistively heated as shown by the modeling by [40]. Downstream the distribution broadens to non-classical values, and a second peak forms nearly centered at 0 km/s. An example of this lineshape evolution is shown in Fig. 4.6.

The two most obvious sources of ions that appear to have zero net drift velocity and a Maxwellian IVDF are charge exchange (CEX) and ionization. To evaluate which is more likely we first seek the mean free path for these processes. First we address CEX, for which the mean free path, λ_{CEX}, is:

$$\lambda_{CEX} = \frac{1}{n_n \sigma_{CEX}}, \tag{4.1}$$

where σ_{CEX} is the CEX cross-section and we have assumed the velocity of the neutrals is low relative to that of the ions, which has been confirmed experimentally [53]. Without advanced diagnostics it is impossible to measure n_n, directly, and so we rely on our simple neutral gas model from Sec. 2.3, which predicts 10^{19}-10^{20} m^{-3}. The maximum value for σ_{CEX} is $\sim 10^{-18}$ m^{-2}, resulting in λ_{CEX} between 5 and 50 mm. The second population is typically seen to form at 15 mm into the plume or further downstream, so it is possible it is (at least partially) caused by CEX.

Likewise, the mean free path for ionization, λ_{iz}, is given by:

$$\lambda_{iz} = \frac{v_n}{n_e \langle \sigma_{CEX} v_e \rangle}, \tag{4.2}$$

where $\langle \sigma_{iz} v_e \rangle$ is the ionization cross-section averaged over the electron velocity distribution function. The neutral velocity, $v_n = \sqrt{kT_e/m_i}$, is $\sim 250 m/s$ for xenon neutrals at 300 K,

and the ionization cross-section for a Maxwellian electron population at ∼3 eV is ∼ 25 mm, which also makes it a possible source of ions at the locations seen.

Also of note is the absence of a clear plateau or tail on the ion distribution functions as predicted by the models in Ref. [54, 27], which could be formed by ion Landau damping. For some locations a slight tail appears to exist but lies within or near the noise floor of the signal. Generally the IVDF's can be deconvolved into Gaussian-shaped distributions. Similarly, some measurements indicate a slight plateau on the high velocity side of the IVDF, but this could be due to the convolution of the two ion populations. Regardless, any significant tails or plateaus are absent, indicating that either the relative proportion of ions resonant with the waves is small or that the thermalization length scale for ions is small.

The likelihood of the latter can be assessed by evaluating the mean free path of ion-ion Coulomb collisions, $\lambda_{ii} = v_{ti}/\nu_{ii}$, where v_{ii} is the ion thermal velocity and ν_{ii}, the ion-ion collision frequency, is given by (see Ref. 34):

$$\nu_{ii} = Z^4 \left(\frac{m}{M}\right)^{1/2} \left(\frac{T_e}{T_i}\right)^{3/2} \nu_{ee}, \tag{4.3}$$

where Z is the atomic number and ν_{ee} is the electron-electron collision frequency given by

$$\nu_{ii} = 5x10^{-12} \frac{n_e \ln \Lambda}{T_e^{3/2}}, \tag{4.4}$$

where Λ is the Coulomb logarithm and T_e is the electron temperature in eV. The resulting mean free path is ∼0.5 mm near the keeper and increases to ∼200 mm at the anode. This indicates that ion-ion collisions could play a role in thermalizing any ion tail in the near plume but would have diminishing effect with distance downstream. To determine how much of a tail should form, a kinetic model accounting for both IAT-driven heating and ion-ion collisions is needed. The mean free paths for these processes is shown in Fig. 4.5

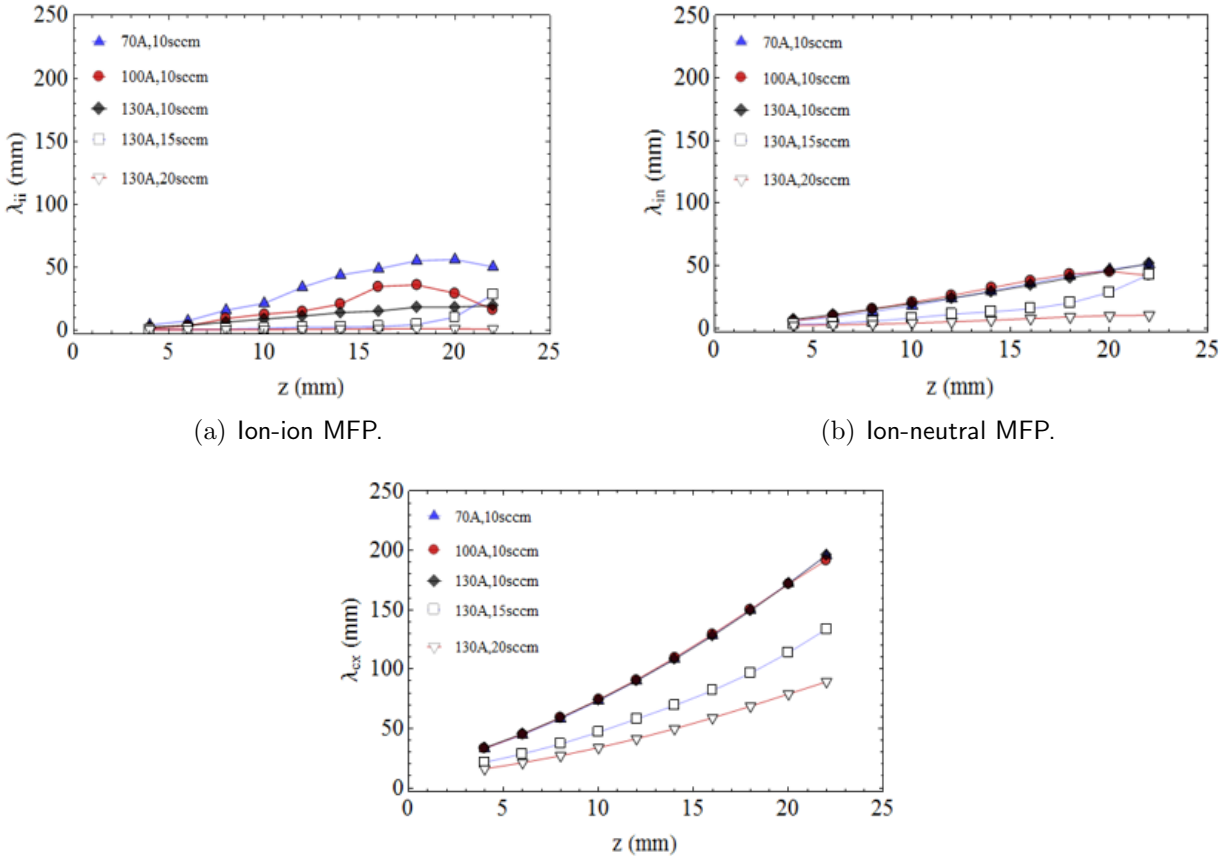

(a) Ion-ion MFP.

(b) Ion-neutral MFP.

(c) Charge-exchange MFP.

Figure 4.5: Collision mean free paths.

4.4.2 Ion Energy and Temperature

To enable comparison to the far-field IEDF results obtained by the RPA in Fig. 4.4, IEDF's calculated from LIF measurements are shown in Fig. 4.7 at the z=12 mm, for the fast population only. Although not reported here, for z≥20 mm, the maximum ion velocity remains nearly constant, and so these LIF-derived IEDF's are representative of that which is expected to exist at the RPA location. These results follow the same qualitative trends in relation to mass flow and discharge current as the axial RPA results, with maximum ion energies also similar.

The results for ion temperature are shown in Figure 4.8. We observe that ion heating

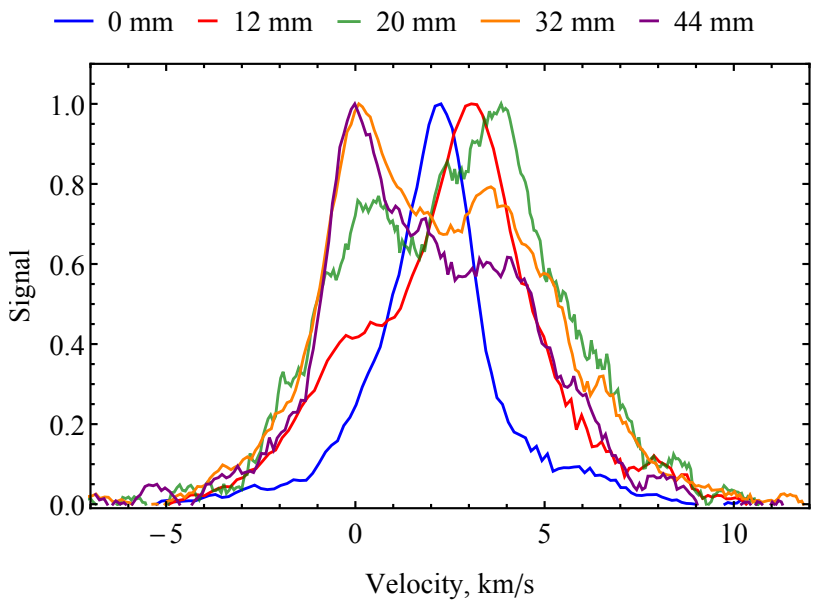

Figure 4.6: Centerline IVDF's for the 70 A, 10 sccm operating condition at various locations downstream. Each plot is normalized by the maximum intensity and filtered using a 9 point moving average.

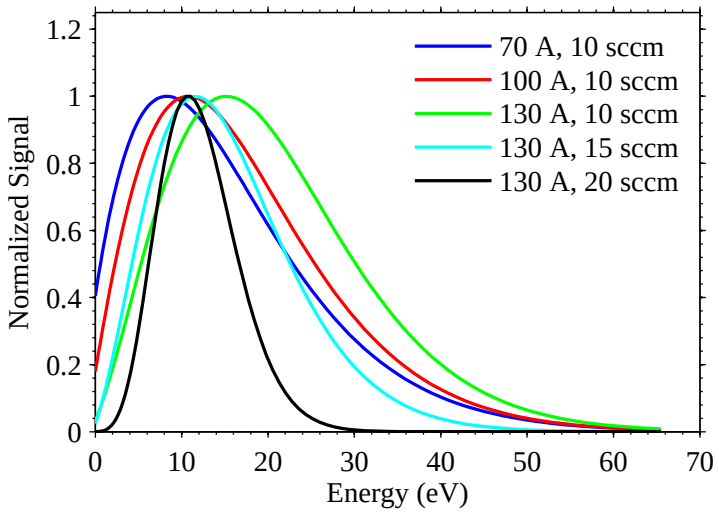

Figure 4.7: Centerline IEDFs at location of peak ion temperature vs. distance downstream of keeper face using a Gaussian fit to the drifting population. The curves are normalized to maximum signal.

is weakly dependent on current but strongly dependent on flow rate. However, all cases at 10 sccm show increasing temperature with distance downstream. For the case of increasing

flow rate the ion heating rate is suppressed and nearly flat for the 20 sccm case. The most probable ion velocities are shown in Fig. 4.9. All cases show a gradual increase in drift velocity with distance from the keeper face. The mechanism responsible for the acceleration could possibly be due to pressure or potential gradients.

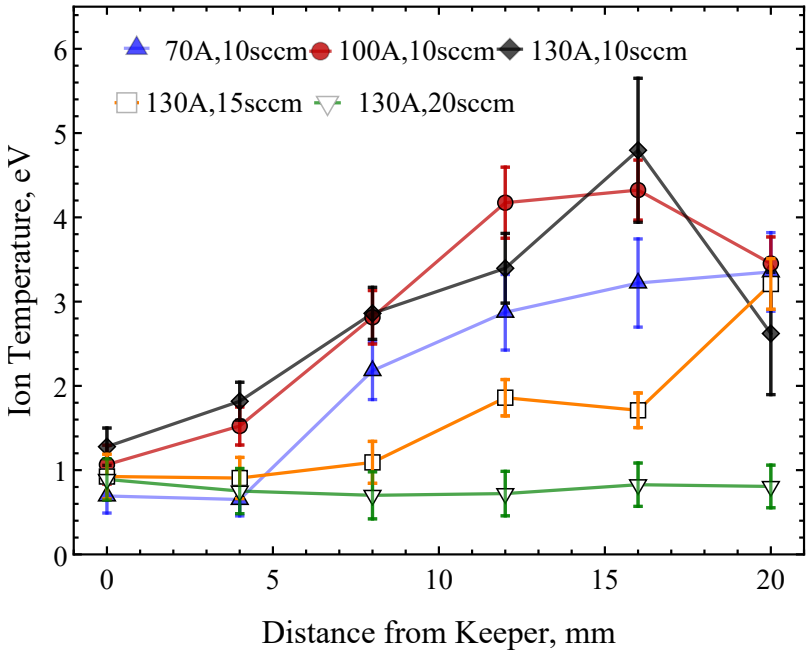

Figure 4.8: Ion temperature for the fast population.

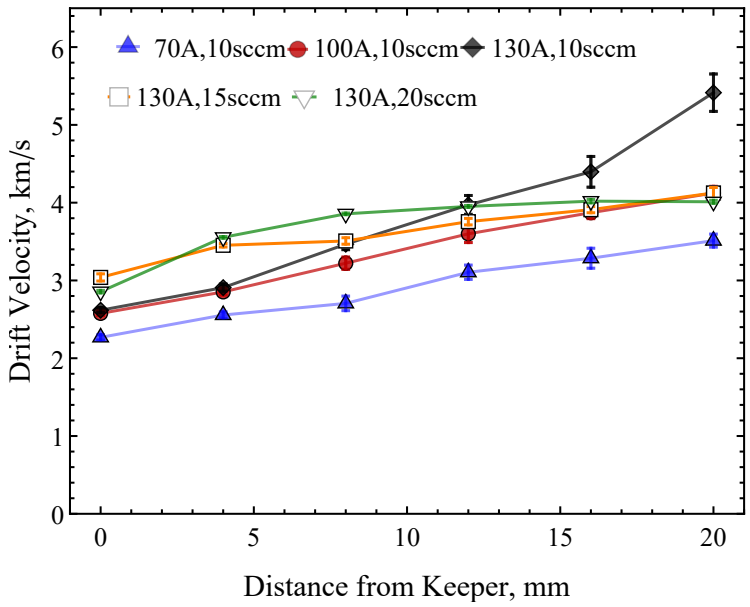

Figure 4.9: Drift velocity of the fast ion population.

4.5 Wave Energy Measurements

To isolate the wave energy associated with the IAT mode from the low-frequency fluctuations, typically at frequencies <100 kHz, the raw spectrum of signal power (i.e. $|\tilde{\phi}|^2$) was fit to a polynomial forced to terminate to zero amplitude at approximately 100 kHz. This ad hoc approach was used because the spectral profile of the low-frequency fluctuations is not known, and because the majority of conditions resulted in an IAT-dominant spectrum. Therefore this approach to spectral curve-fitting should introduce little uncertainty to the integrated spectral power.

Figure 4.10 shows contour plots of the spectral power evolution with distance into the plume, illustrating increase in power at higher frequencies followed by a reduction towards low frequencies near the anode. Using Eq. 3.4 and these integrated spectral powers, the wave energy density was calculated and is shown below in Fig. 4.11. Note that the wave energies for the 70 A, 10 sccm condition are not reported for z > 14 mm due to the inability to isolate the IAT component. The first general trend found is that increasing gas flow rate correlated with decreasing wave energy, possibly due to larger damping of the IAT mode by ion-neutral

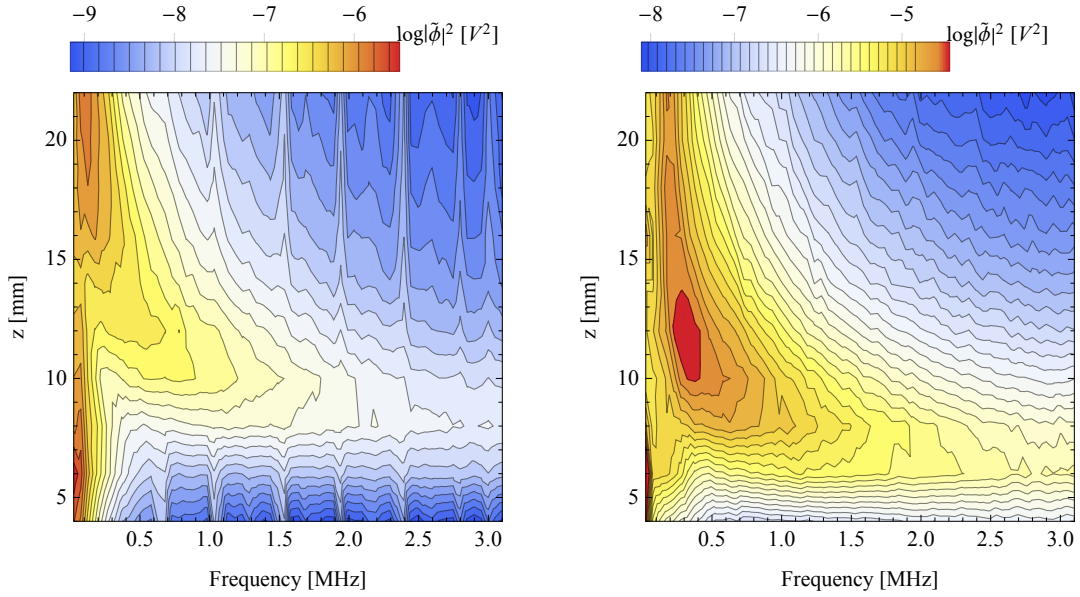

(a) 70 A, 10 sccm

(b) 130 A, 10 sccm

Figure 4.10: Wave fluctuation power spectrum evolution with distance downstream for two different operating conditions. (Note that the intensity scales are different for the two operating conditions).

collisions. The second trend is that increasing discharge current correlated with increasing wave energy. However, the peak wave energy for the 100 A, 10 sccm case was higher than the 130 A, 10 sccm case, which differs from the trend seen in Ref. 21 (for similar currents but at 15 sccm instead of 10 sccm) which showed a monotonic increase in total wave energy with discharge current. The correlation of wave energy with discharge current is not obvious because the growth term depends not only on current but also on the relative electron drift velocity and particle temperatures, as well as on the specific non-linear saturation mechanisms of the turbulent energy spectrum. This non-monotonic increase of IAT with discharge current remains an open issue. As discussed by Jorns [1] and Fenneman [28], there is not an obvious dependence of electron drift velocity, which determines the growth rate, and discharge current. A final note on the growth, and saturation, of the wave energy is that, as shown by Jorns in Fig.13 of 1, the growth increases until reaching the so-called Sagdeev limit [38], which is based on a saturation bound due to non-linear Landau damping.

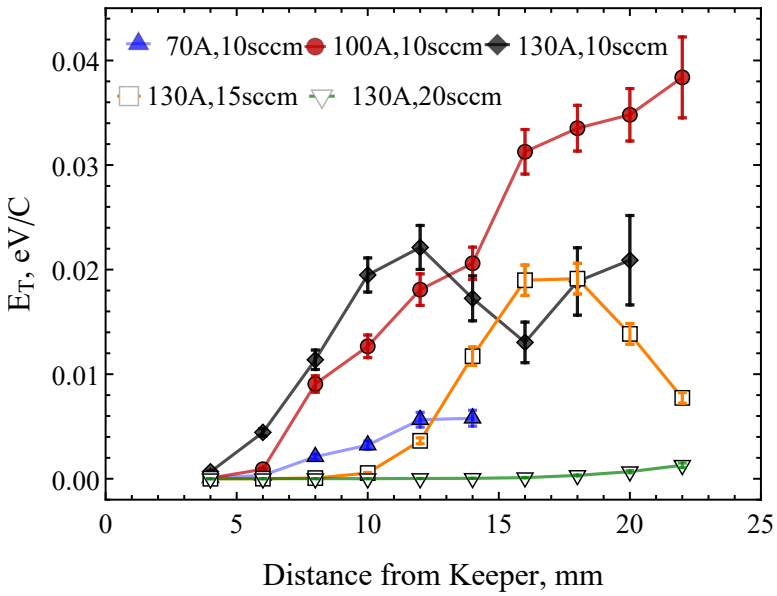

Figure 4.11: Wave energy vs. distance downstream of the cathode keeper face.

4.6 Scaling of Ion Temperature with Wave Energy

As discussed in the introduction, there is evidence for a correlation between ion energy in the far plume and wave energy associated with IAT wave energy. Indeed, the results of this study (as shown in Figs. 4.8 and 4.11) show similar qualitative trends in both ion temperature and wave energy as discharge current and flow rate are varied, resembling correlations first noted in Ref. 27 using an RPA to determine ion energy in the far plume. These observations also make intuitive sense in that the waves are primarily carried by ion motion and therefore an increase in wave energy should lead to an effective increase in ion temperature. It should be noted that we can not rule out other mechanisms that could also contribute to ion heating. For example, it is possible that there could be a potential drop along the centerline that could accelerate ions. Although plasma potential was not measured in this experiment, no measurements in the literature indicate potential drops sufficient to explain the high energies measured here by LIF and RPA diagnostics. Additionally, ions may gain energy from the low-frequency fluctuations. Because such a coupling has not been investigated, it is not possible to estimate this effect, and so we focus here exclusively on the effects of the IAT

mode.

We will now explore this scaling quantitatively in the near plume, which could be useful for informing cathode simulations such as that in Ref. 40 that are attempting to self-consistently determine the wave energy density and ion temperature. We follow the theory discussed in Sec. 2.4, in which we defined the experimentally determined scaling parameter as $\Gamma_{Meas} = \Delta T_i / \Delta E_T$, where ΔT_i and ΔE_T are the changes in ion temperature and wave energy density relative to the conditions at the keeper face (approximated by measurements at z=4 mm). Figure 4.12a shows both Γ_{Meas} (where ΔT_i at the location of the E_T measurements was estimated by interpolation of the LIF-obtained T_i) and Γ_{Theory} calculated using Eq. 2.25 on a semi-log scale. Due to the large number of assumptions no uncertainty analysis for the theoretical estimate was performed. Figure 4.12b shows the scaling parameters accounting for propagation of uncertainty on a linear scale. Upstream of z=12 mm the uncertainties in Γ_{Meas} are large due to the large relative uncertainties and small changes in parameters before the exponential rise downstream. For this reason we focus on the region z$\geq$12 mm where the scaling parameters converge towards the theoretical estimates. Additionally, because no appreciable changes in either ion temperature or wave energy were observed for the 130 A, 20 sccm operating condition, scaling parameters for those measurements are omitted from both figures.

These figures show that Γ_{Meas} is very large in the region nearest the keeper and decreases exponentially downstream, almost monotonically. Some potential explanations for the deviation between Γ_{Meas} and Γ_{Theory} are proposed here. The first uncertainty considered is the value of ion temperature. As discussed, the degree of saturation broadening cannot be fully determined without repeating the experiment due to uncertainties in validity of the two-level energy model for this transition. Additionally, it is possible that one or both of the ion distributions being fitted are not Gaussian. However, in the near-keeper region the temperature estimates would have to be off by 2-3 orders of magnitude to explain the disagreement in Γ. The wave energy measurements could also have been affected due to the

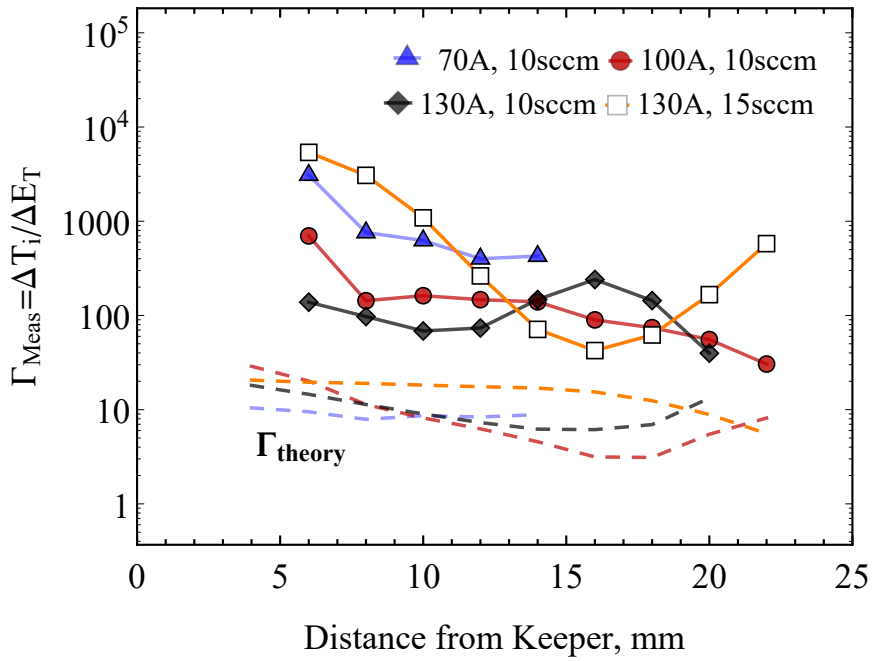

(a) Measured (solid) and theoretical scaling parameters (dashed).

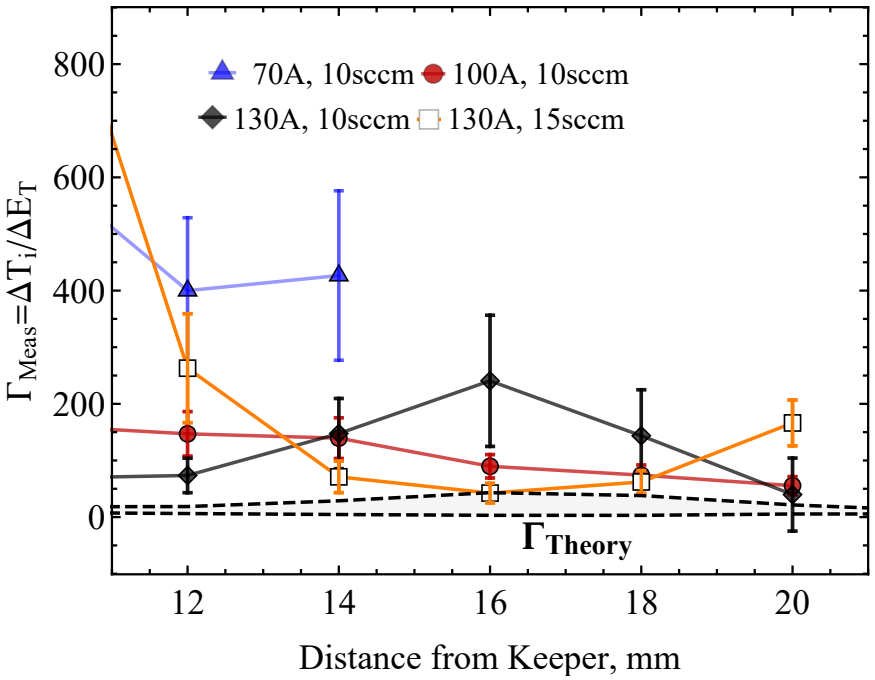

(b) Measured scaling parameters with uncertainties for z > 10 mm. Only the bounds of the theoretical scaling parameter are shown for clarity.

Figure 4.12: Scaling parameters.

inevitable perturbation of the plasma since the probe was large in relation to the plume diameter near the keeper.

Another possible explanation for these observations could be that the fluid formulation used to derive the scaling parameter in Eq. 2.25 in Ref. 39 is not valid in the region nearest the keeper, but becomes increasingly valid with distance downstream where the instability saturates. The theory assumes slowly varying plasma parameters with respect to the wave growth rate, which may not be the case in regions nearest the keeper. Also, the α parameter from Eq. 2.25 may not be constant in the plume. Near the anode, where the IAT is more fully developed, there is agreement to theory within a factor of 10 for two operating conditions, which is encouraging and may indicate that the theory can be improved to better account for regions corresponding to the initial growth of the instability.

4.7 Particle Drift Effects

The Langmuir probe interpretation used to generate the results of this study assumes ion drifts are small relative to their thermal speeds (i.e. $M_s = V_s/v_{th} << 1$). However, centerline Mach numbers of 2-4 for ions were measured for this experiment as shown in Fig. 4.13, indicating that drift effects on density measurements may be important. An estimate for this effect can be performed based on the results of McMahon [55], who performed simulations of drifting plasmas incident on cylindrical probes. Using the results in Sec. 4.2, and referencing McMahon's parametric curves, the result is that the non-drifting assumption overestimates plasma density by a factor of 2 along the plume centerline compared to the case where drifts are considered, assuming ion temperature isotropy and a constant ratio of ion to electron temperature. Since ion temperature anisotropy, electron temperature, and plasma potential are all varying throughout the plume, proper correction for flowing effects on density are outside the scope of this paper. However, given the large potential additional uncertainty of particle flows, the results here should be viewed with the understanding that the corrected

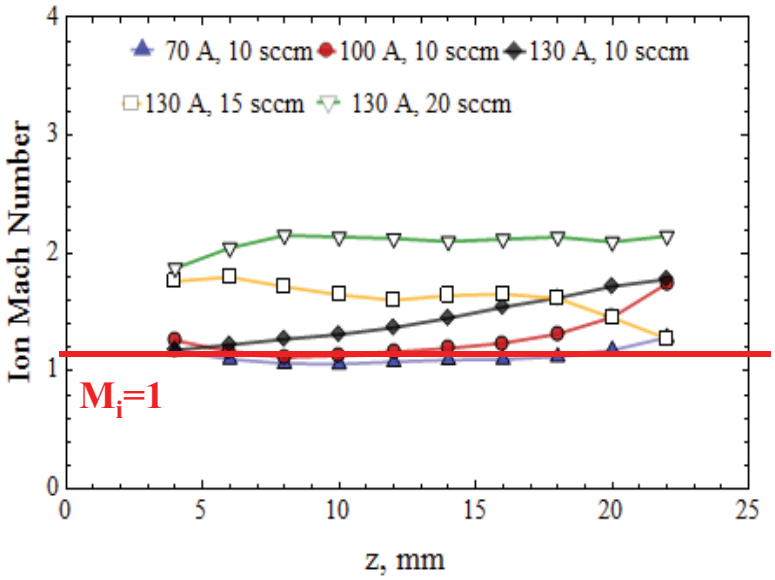

Figure 4.13: Ion Mach numbers calculated using $M_i = V_i/v_{th}$.

densities could be lower than that shown.

The effect of drifting electrons will be primarily on the electron temperature measurement. Assuming a drifting Maxwellian electron population incident on a probe, there be a significant modification to the equation used for estimating T_e if $M_e = V_e/v_{e,th} > 0.1$ [56]. For a cylindrical probe oriented with the probe axis orthogonal to the electron drift direction the traditional analysis tends to overestimate T_e, and this correction factor scales with the drift magnitude as $T_{e,drifting}/T_{e,stationary} = e^{1.12M_e}$. Applying this correction and using the Mach numbers calculated by Jorns for this operating condition in Ref. 1 (where $M_e \sim 1-2$), the electron temperatures would be reduced by a factor of 2-9, which is significant.

The challenge in applying this correction is knowing the electron drift velocity profile in the plume. The approach by Jorns [1] estimates the average electron drift by integrating the electron current density over an area at a fixed axial position with a known total current, giving a mean drift speed across the plume jet. However, it is possible that the maximum drift us not captured due to the averaging. Also, it is possible that more electron current is carried by off-axis plasma since the potential trough would tend to draw electrons radially

outward as well as downstream towards the anode. Due to these unknowns, we acknowledge that the approach taken here may result in an overestimate of T_e in regions of significant electron drift, which is most relevant to the calculation of the wave energy calculation, Eq. 3.4, since when the relation for $\widetilde{\phi}_\omega$ from Eq. 3.5 is inserted the result is that $E_T \propto T_e$. This implies that the wave energy may be lower than presented here.

CHAPTER 5

Ion Energy and Wave Propagation in Two Dimensions

5.1 Introduction

The objective of this experiment was to evaluate the ion and wave properties throughout the plume domain, rather than just along the centerline as was performed in Ch. 4. While there are no theoretical predictions yet for the scaling of wave and ion energy, the scaling can be measured and the flow and energies measured to reveal the dominant physics in the plume. Upgrades to the experimental setup include using an array of three probes instead of one (to measure wave dispersion) and the addition of a radial LIF injection beam for measuring the radial IVDF component.

5.2 Operating Conditions

The centerline study discussed previously was performed at background pressures of 2.2×10^{-4} Torr in order to match conditions for earlier IAT experiments at JPL. However, for the pumping configuration used, even when only operating a single cryopump a large xenon flow rate through a leak valve was needed to maintain this pressure. Without the leak valve, when at $\sim 10^{-6}$ Torr background pressure, the cathode would become wildly unstable and discharge currents >50 A were not attainable at the flow rates tested previously. To minimize the amount of xenon used for testing, and to maintain high currents, the flow rates tested were increased to 15, 20, and 25 sccm, and the discharge currents tested were 100, 130, and 160 A. The I-V curve for 15 sccm is shown in Fig. 5.1, and the operating conditions for this second

test series are shown in Table 5.1. (Note that the standard used for flow rate is 25°C and 14.7 psia). Probe measurements of the plasma properties were obtained for all the operating conditions, but due to time constraints LIF measurements in the full 2D half-plane were obtained only for three operating conditions. Centerline LIF measurements were obtained for all operating conditions.

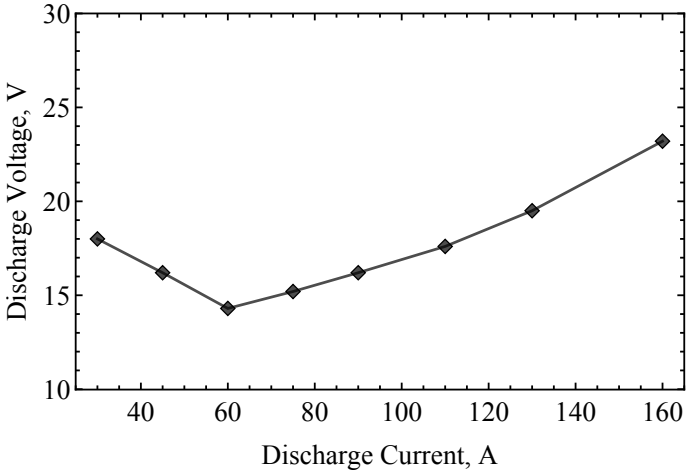

Figure 5.1: Discharge voltage vs. discharge current for 15 sccm.

Table 5.1: Operating Conditions.

Discharge Current [A]	Discharge Voltage [V]	Flow Rate [Std. cm^3/s]	Measurements
100	16.7	15	Probes, 2D LIF
130	19.5	15	Probes, CL LIF
160	23.2	15	Probes, 2D LIF
160	20.6	20	Probes, CL LIF
160	19.0	25	Probes, 2D LIF

To verify there were no large-amplitude, global fluctuations (plume mode or otherwise), for this experiment a current probe was used on the cathode discharge power supply cable. Used in AC-coupled mode, the discharge voltage, discharge current, and discharge current fluctuations were recorded as shown in Fig. 5.2.

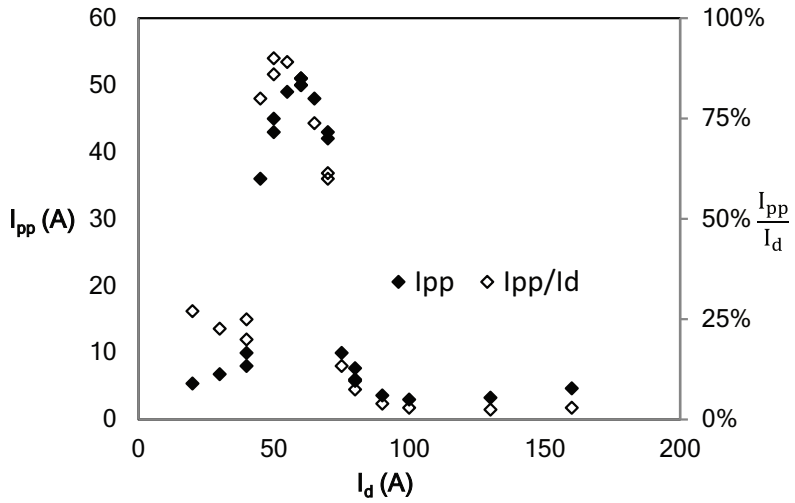

Figure 5.2: Discharge current oscillations.

5.3 Background Plasma Properties

Figure 5.3 shows the steady-state background plasma properties for the five operating conditions probed. Plasma density, electron temperature, and plasma potential in the plume are presented using using first-order interpolation. The density shows a dense jet of plasma flowing axially towards the anode, with most of the plasma located within the keeper radius of 5 mm. As will be discussed later, this high density along with a neutral gas density of $\sim 10^{20} m^{-3}$ should result in a high ion collision frequency that would tend to thermalize to a Maxwellian. Electron temperatures of 2.5-3.5 eV are found throughout the domain but dropping significantly at the wings. These measurements are consistent with previous measurements in these operating regimes.

The plasma potential shows a potential trough with increasing potential towards the wings of the plume. Since the plasma potential a result of charge particle balance and the potential of the boundary conditions, it makes sense that the maximum potential would occur on the sides in line with the anode which is biased at $\sim V_d$ relative to the cathode (which is at ground potential). Along the centerline the potential gradient is negligible.

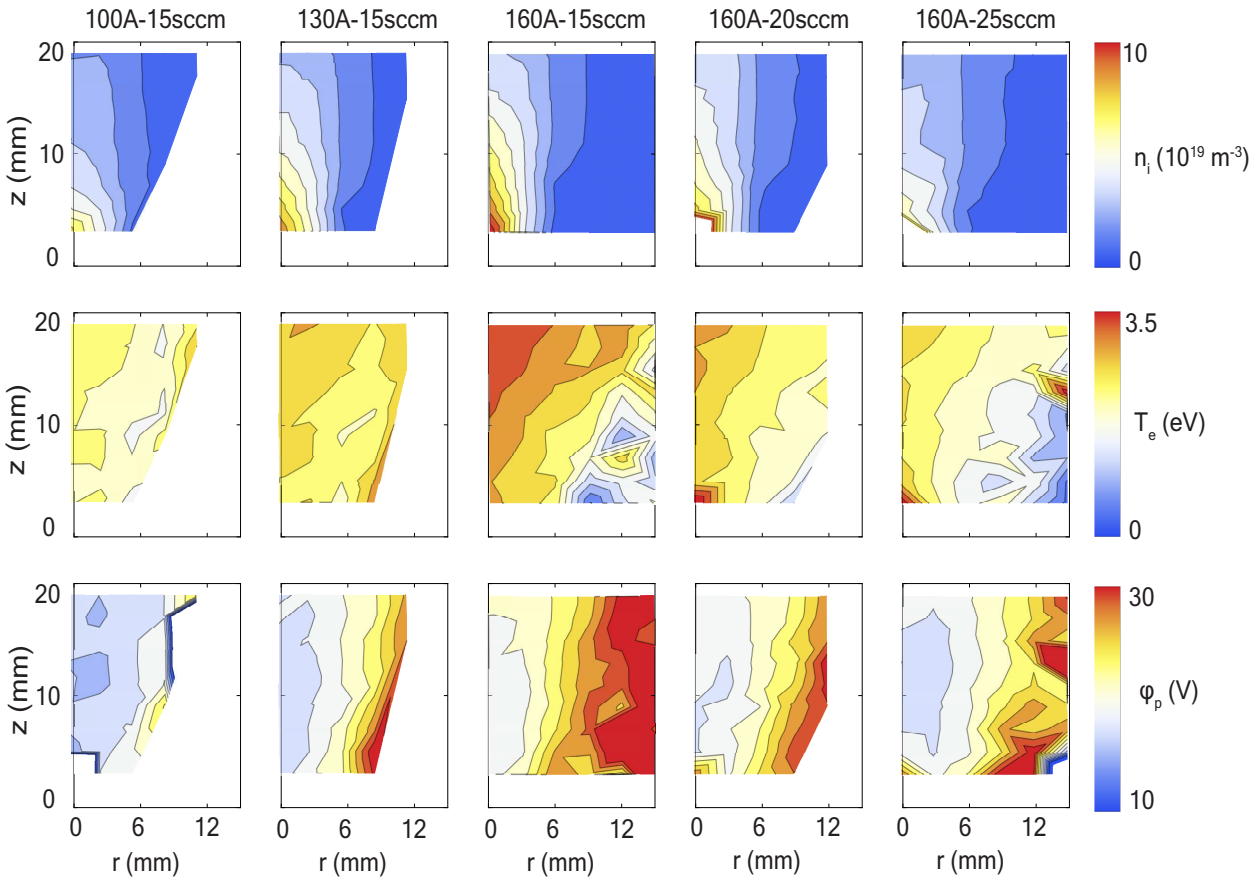

Figure 5.3: Background plasma properties: density (top row), electron temperature (middle row), and plasma potential determined indirectly from density and temperature (bottom row). First order interpolation was used to generate the countours.

5.4 LIF Measurements

The ion properties in the plume discussed here were obtained using LIF. The domain was sampled with Δr=3 mm and Δz=4 mm. Figure 5.4 shows several of the axial IVDF's measured throughout the domain, along with the curve fit applied to the drifting component (in red). The radial IVDF profiles are not shown because they all could be fit by single Gaussian curve fits and showed single peaks only. Several features were observed in the axial IVDF's. First, for regions outside the cathode orifice but near the keeper (i.e. for r$\geq$3 mm and z$\leq$11 mm) a second, negative velocity peak was observed, with velocity opposite that of the positive-going peak but with varying amplitude. This is believed to be due to reflection

of the axial LIF injection beam off the tungsten orifice and off of tungsten deposition on the keeper face (caused from sputtering of the anode liner), which was found to be significant in the post-test examination of the keeper. Due to a dropoff in intensity of the reflected laser light with distance from the keeper, the peak assoaciated with it drops and is essentially invisible at z=10 mm. Farther downstream, an additional signal peak appears at ∼0 km/s.

Additionally, for regions farther into the plume (z>11 mm) a second peak in the signal is found approximately centered at 0 km/s. As discussed in Sec. 4.4, this could be due to the background plasma formed by ionization or charge-exchange collisions. Interestingly, the amplitude of the slow peak was only signifant for the 160 A, 15 sccm operating condition. The reason for this is unknown at this time. Also, since ionization and charge-exchange are isotropic, slow peaks would be expected in the radial IVDF's but none were observed, even for the 160 A, 15 sccm condition. It is possible that the radial velocity distribution functions of the two populations were closely overlapped in velocity space.

The ion velocity vectors for the fast population are shown in Figure 5.5(a). Uncertainties in flow direction are less than 2%. It was found that both the axial and radial drift components increase with distance from the cathode orifice, beginning at ∼2.5 km/s and increasing to nearly 5 km/s near the anode (see Fig. 5.6). The most likely cause for the acceleration is due to the strong pressure gradient. The structure of the flow is similar for all three operating conditions, despite differences in background plasma profiles, perhaps due to the similar pressure gradient profile for the three cases.

Figure 5.5(b) shows the variances of the Gaussian fits to the IVDF chords of the fast population, measured using the axial and radial injection beams. The length of the bars represents temperature and the bars are aligned with the direction of the injected beam. Both the axial and radial IVDF's obtained show an increase in the temperature with distance from the cathode orifice. Along the centerline the ions start out isotropic with T_i=1 eV, and evolve downstream to have an axial temperature of ∼5 eV with the radial temperature only increasing slightly. Only the condition with the highest discharge current - flow rate

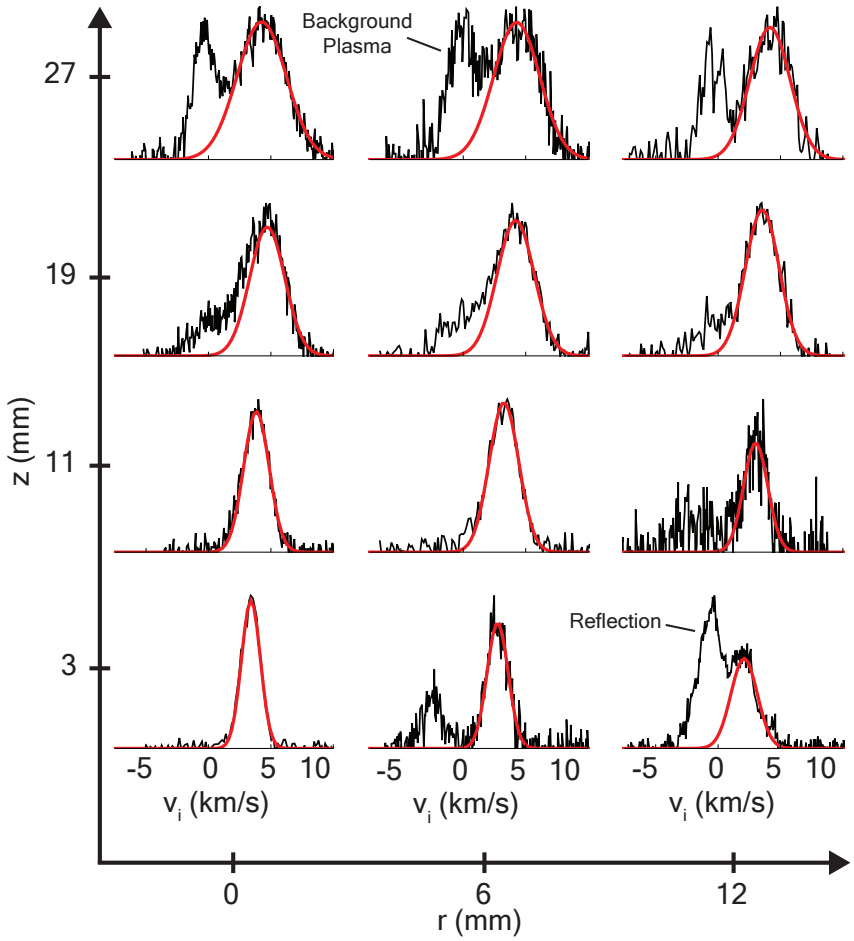

Figure 5.4: Axial IVDF's measured by LIF for the 160 A, 15 sccm operating condition. The raw data is shown in black and the Gaussian fit to the fast population is shown in red.

ratio shows significant ion heating. Uncertainties of the LIF measurements are shown in Appendix A.

We were not able to measure the IVDF along other chords so we cannot say what the 2D IVDF would look like. However, one could speculate that if it is Gaussian in all directions that there is some direction in which the ellipse is longest. It would be interesting to make a 2D measurement of the IVDF in order to see if there is a correlation between the long axis of this supposed ellipse and either the ion drift direction or acoustic wave propagation direction, as it could shed some light on the mechanism between the heating.

A final note regarding the shape of these distributions is the lack of any appreciable velocity component in the direction of the keeper. Neglecting the portion of the signal attributed to the reflection of the laser off the keeper orifice or keeper face, there is only a small portion of the distribution (seen as the curve fit to the fast population) directed back to the keeper. If these conditions are in fact similar to those tested by Ho [23], then this would imply that a) the number of singly-charged ions incident on the keeper face is small, b) the number is appreciable but the signal is buried in the reflection signal, an so not possible to deconvolve, c) the density in the region near the keeper is high enough such that even with the low energy towards the keeper there is sufficient sputtering to explain the erosion, d) the conditions tested here were not the same as those tested by Ho, or finally e) the cause of the anomalous erosion is not caused by singly-charged ions, but instead is caused by doubly- or triply-charged ions that gain more energy in falling through the keeper sheath and cause sufficient erosion due to the nonlinear scaling of sputter yield with ion energy.

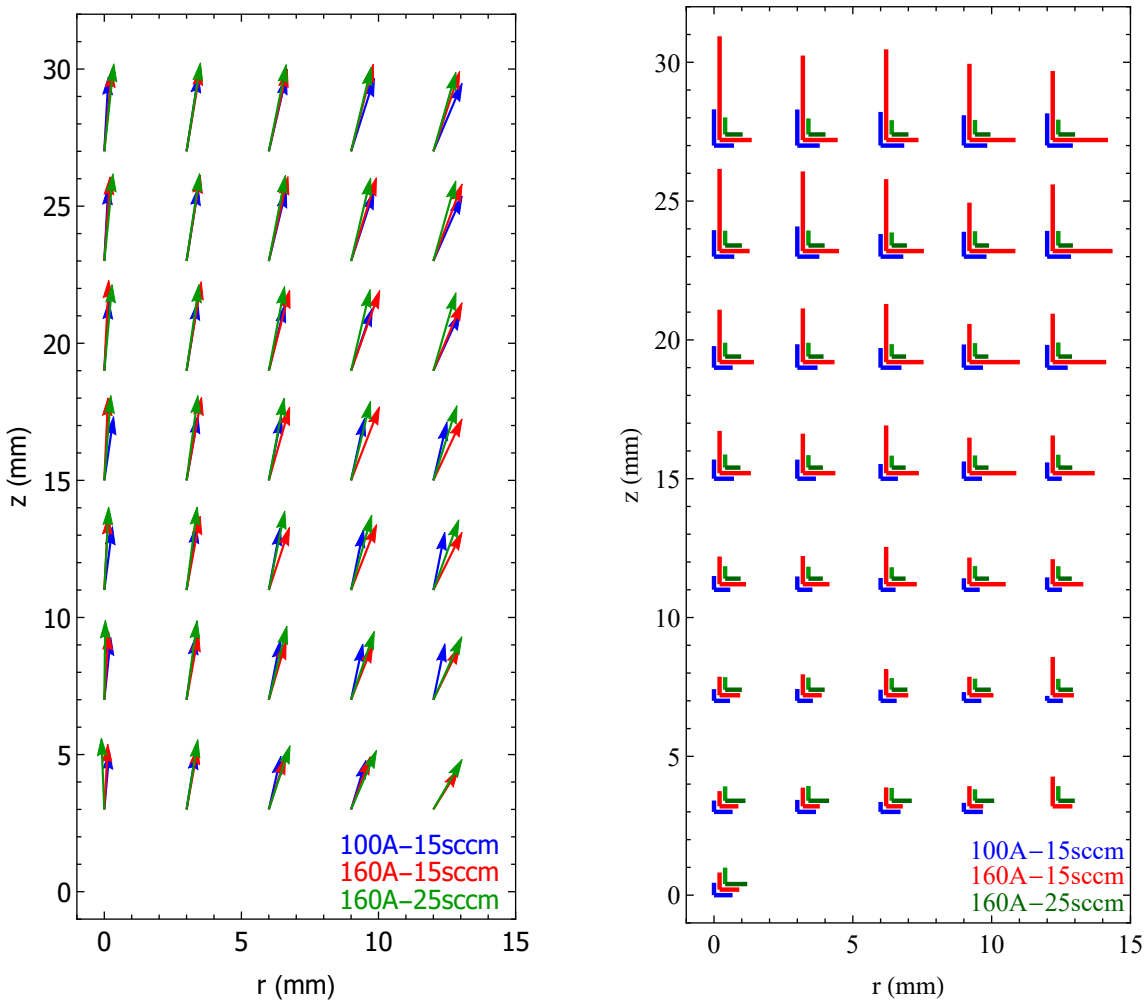

(a) Most probable drift velocities for the fast ion population measured with LIF.

(b) Temperature measurements for the axial and radial velocity distribution measurements.

Figure 5.5: LIF measurements of velocities and temperatures of the fast ion population.

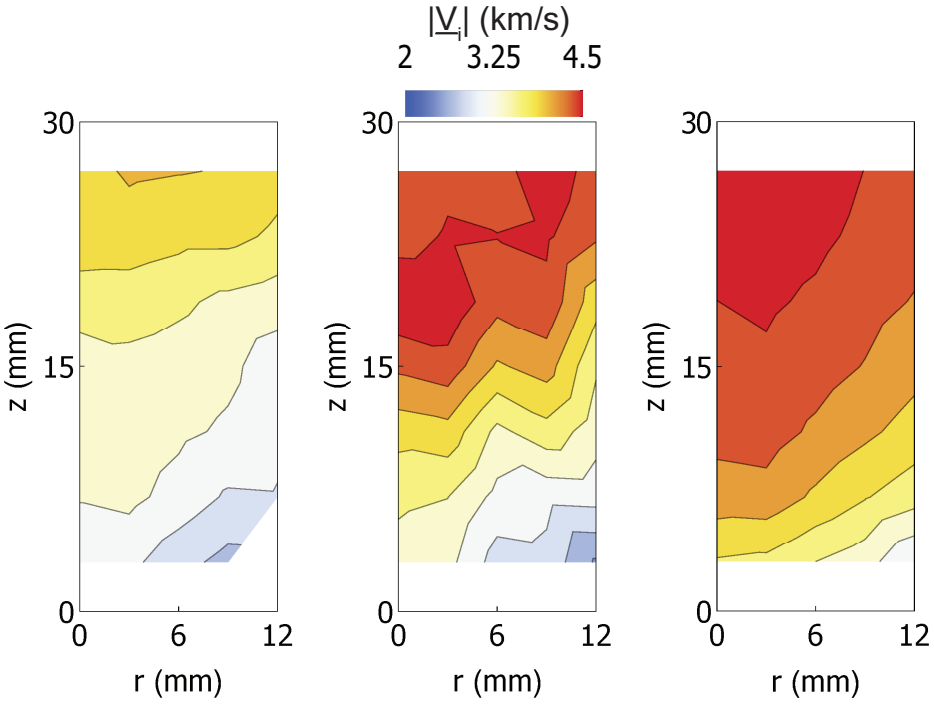

Figure 5.6: Ion drift speeds.

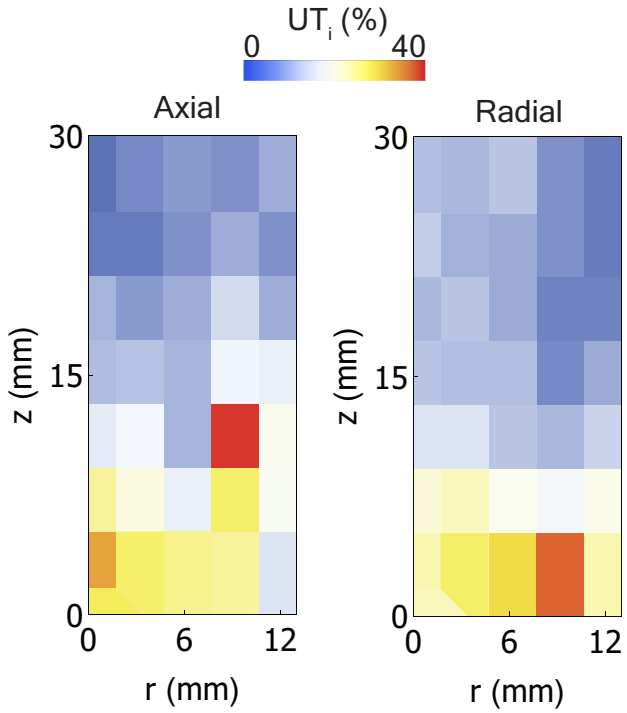

Figure 5.7: Ion temperature uncertainty for the axial LIF measurement at the 160A, 15sccm operating condition.

5.5 Wave Measurements

The wave measurements obtained from the Langmuir probe array, described in Sec. 5.5, will now be discussed. First we will present the dispersion relation measurements which provide information on wave vector direction and phase velocity, and then we will present the wave energy obtained by integrating the fluctuation spectrum.

5.5.1 Dispersion Plots

An example of the types of dispersion measurements is shown in Fig. 5.8 for the 160A-15sccm operating condition. Near the keeper the SNR is low despite the high density in this region, possibly because the wave is strongly damped at this stage. Downstream the SNR increases, and in the jet portion of the plume the linear dispersion is clearly observed for $f > 100$ kHz. For lower frequencies, and for all frequencies near the wings of the plume (outside the jet) the dispersion is less clear. Additionally, the radial measurements generally had a lower SNR than the axial, as well as a broader dispersion. This is suspected to be due to the primarily axial propagation of the waves. Some other observations that deserve note are plots with nearly vertical profiles (suspected to be a signature of plume mode [57, 58]), negative slopes in the low frequency portion (possibly negative-going ion acoustic waves [59]), or inflection points in the slopes of the IAT portion. One cause of this last observation is the presence of the background plasma in which waves would propagate at a slower absolute velocity (since stationary), and that this signal would be more dominant in some portions of the dispersion relation. Investigations into these features could lead to a better understanding of the nature of the modes present in the cathode plume.

5.5.2 Wave Propagation

Figure 5.9 shows the results for the wave propagation directions using the dispersion relation measurements for all five operating conditions tested as part of this experiment. The vector

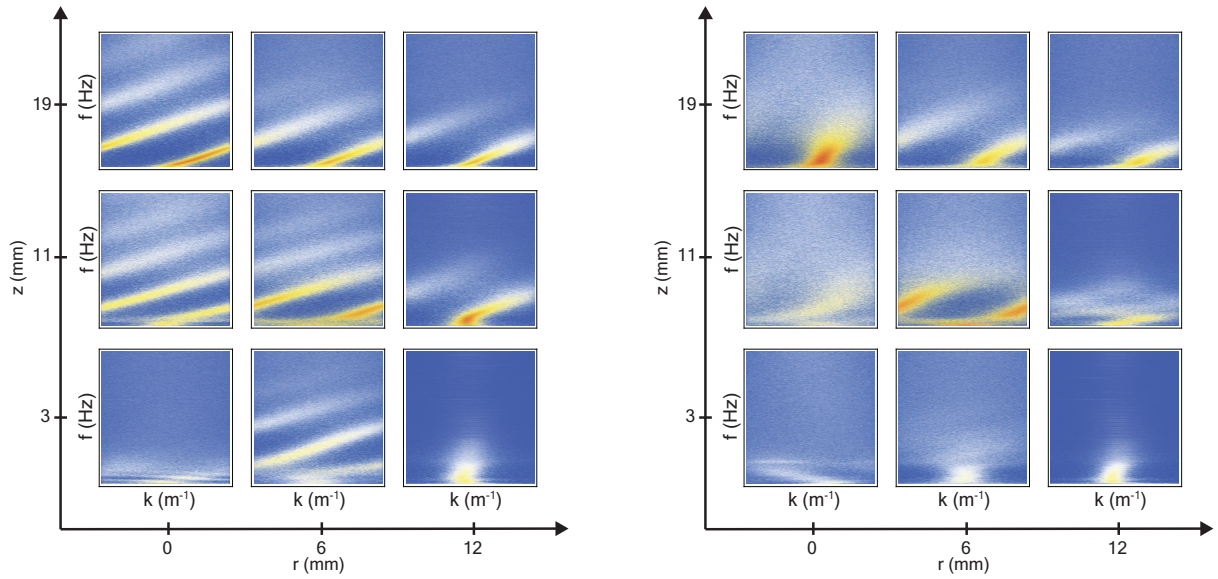

(a) Axial dispersion relations.

(b) Radial dispersion relations.

Figure 5.8: Dispersion Relation Measurements

magnitudes are normalized. The domain was sampled with 2 and 3 mm spatial resolution in the axial and radial directions, respectively. The vectors for some locations are not shown due to the low signal-to-noise ratio in those regions. The first observation is that the waves propagate outward from the orifice. Since the energy source for IAT is the electron drift, and the electrons carry the discharge current to the anode, it is reasonable for the waves to propagate outward from the orifice in the direction of the anode. The wave propagation direction for all five cases is similar in the jet of the plume. Since the waves propagate in the relative drift vector of the ions and electrons, and the ion flow is similar for all cases in the core as well, this indicates the electron flow velocity is similar (at least in direction) for all conditions. This could be due to the similar plasma potential structures for each condition.

The wave propagation directions deviate from one another near the keeper and on the wings of the plume. In these regions, SNR of the radial dispersion relation measurement in particular becomes low, adding uncertainty to the group velocity estimates. Figure 5.10 shows the uncertainty in the wave propagation angle for the 160 A, 15 sccm condition illustrating this spatial profile. Angle uncertainty is <10 ° in the jet of the plume. In the regions

where the uncertainty is greater, the vectors also disagree, indicating that perhaps this is due to the low SNR in these regions rather than an actual deviation in wave propagation. It is also possible that the differences are due to the different potential well structures which may be more pronounced on the wings than near the core, leading to a different flow path of electron current and, therefore, wave generation and propagation directions. The other two cases, though not shown, had wave angle uncertainties that were less than the case shown here.

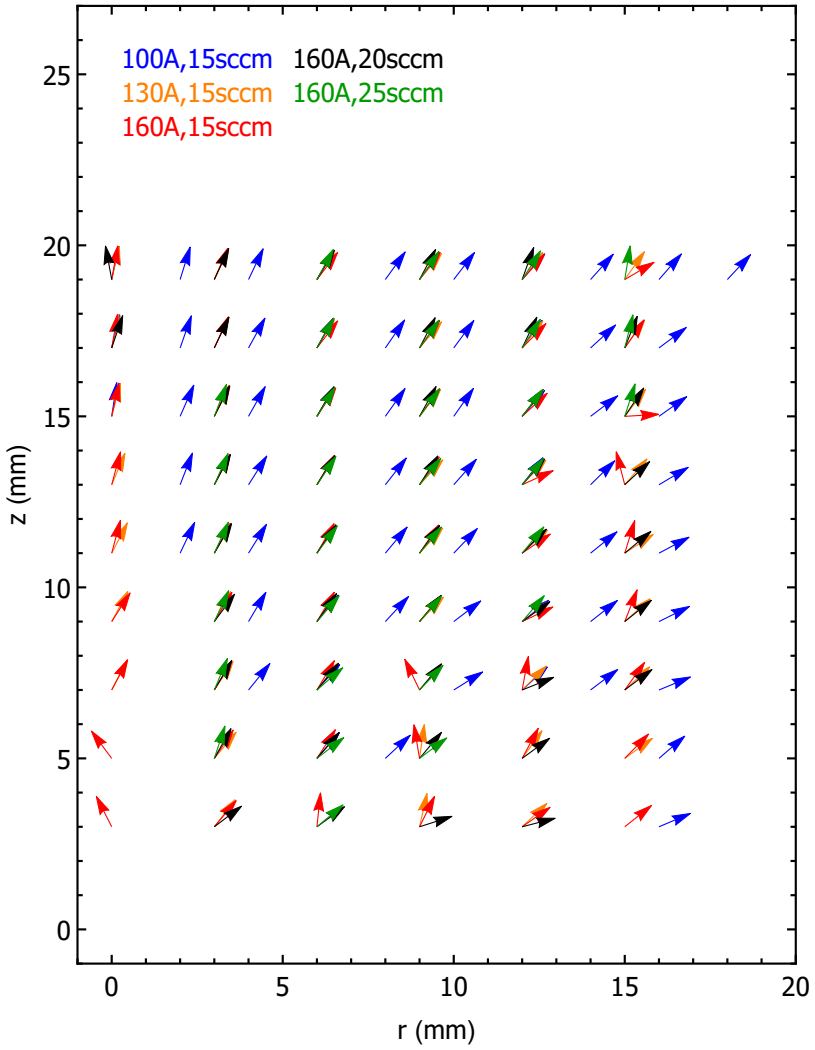

Figure 5.9: Group velocity vectors of the ion acoustic waves, determined by fitting to the slopes of the linear portions of the dispersion relations. The vector magnitudes are normalized.

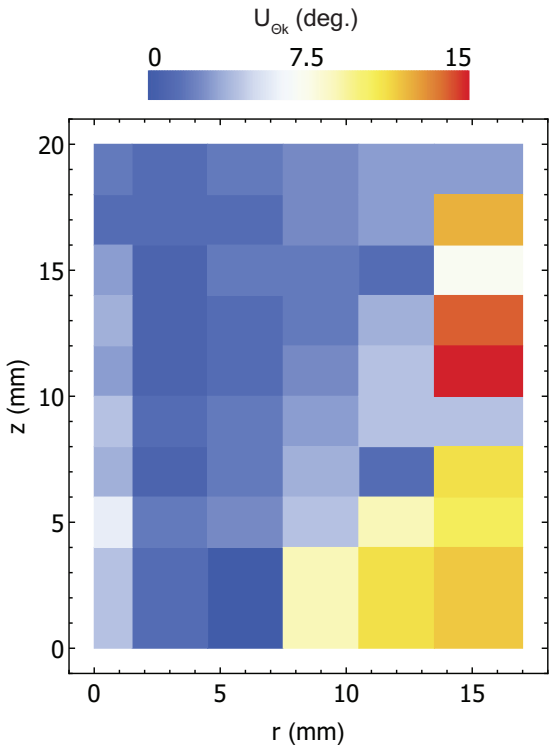

Figure 5.10: Uncertainties of the wave vector angles for the 160 A, 15 sccm operating condition.

5.5.3 Wave Spectra and Energy

Examples of the wave spectra used to determine the spectral power for the wave energy calculation of Eq. 3.4 are shown in Fig. 5.11. From these, and the background properties discussed previously, the wave energy results for the three cases is shown in Fig. 5.12. The intensity scale is logarithmic due to the several orders of magnitude difference between the cases. The wave energy grows with distance from the orifice. For the 100A-15sccm and 160A-15sccm casees the peak is along the centerline, whereas for the 160A-25sccm case the peak is off-axis, although it is possible the peak is along the centerline for this case as well but was beyond the measurement domain. Exponential growth of the wave energy density was observed along the centerline up to ∼15 mm from the keeper, where it then saturates based on the analysis of these data (cf. Ref. 1, Fig.11). In that analysis the growth rates matched analytical predictions (using a quasilinear hierarchy) within the experimental

uncertainty. Note that the 160A-15sccm case was also the case in which the most ion heating was observed, adding further evidence of a correlation between IAT wave energy density and ion temperature, consistent with previous results from Dodson et al. [60]. The uncertainty of the wave energy measurement is low along the centerline and in the plume jet, but increases dramatically on the wings of the jet due to the contributions of electron and ion temperature uncertainties in these regions.

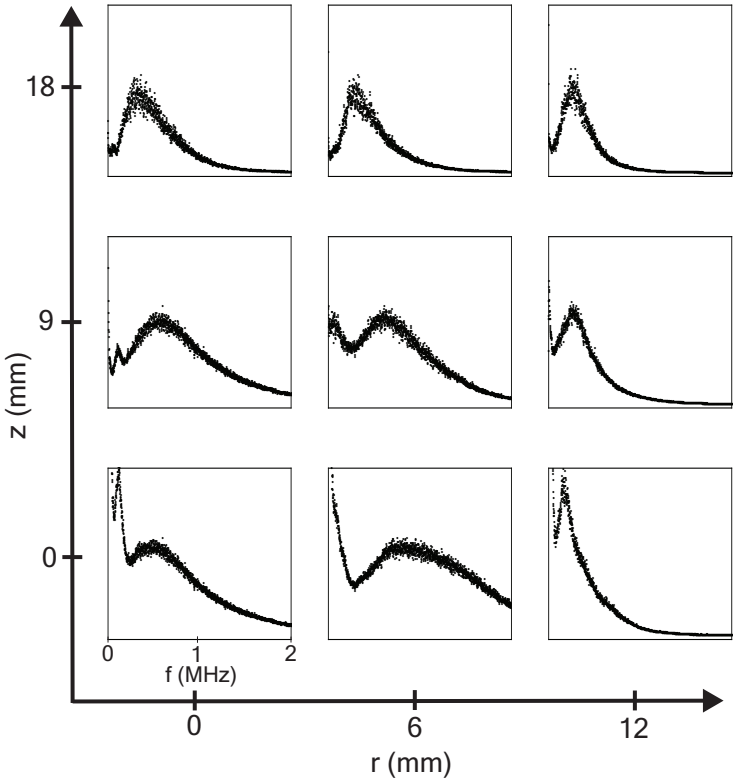

Figure 5.11: Wave spectra for the 160 A, 15 sccm operating condition. The vertical axis scaling is different for each to illustrate the spectral profile only.

According to Kadomtsev [36] the wave energy is highest in the direction of the relative drift between the electrons and ions. Given this assumption, Fig. 5.9 indicates that the ions and electrons are drifting collinearly. It is possible that it is a coincidence that the vectors line up given that there is uncertainty in vector directions, probe effects could be significant, there is ion temperature anisotropy, and the fact that there are multiple ion populations. However, this observation warrants further investigation to see if it is possible

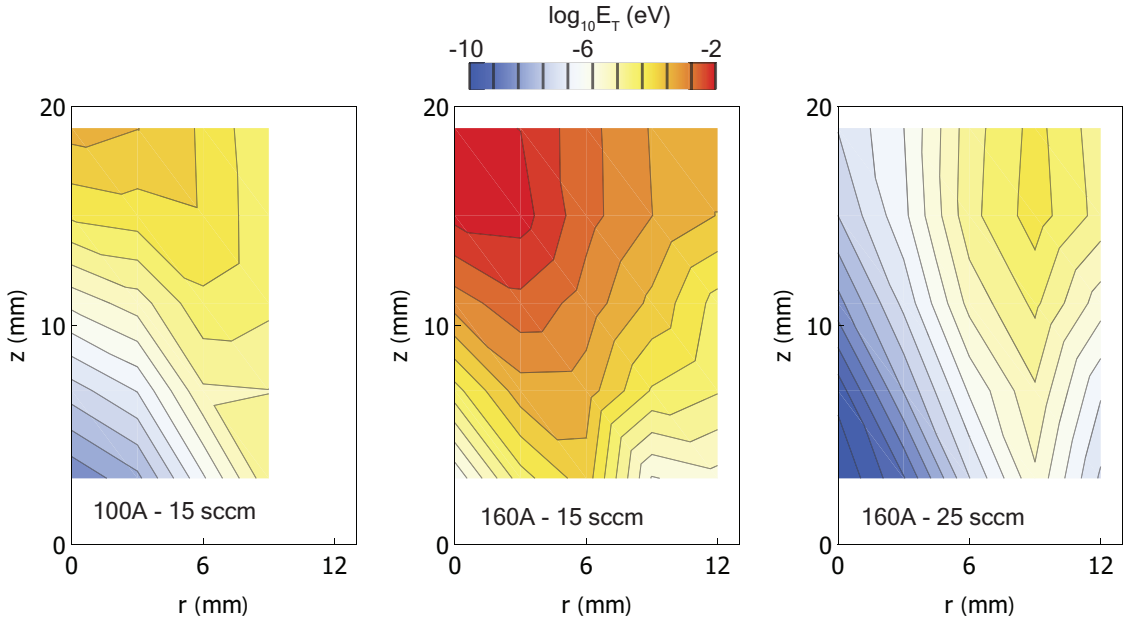

Figure 5.12: Wave energies for three operating conditions. The intensities are scaled logarithmically, with each contour representing an order of magnitude difference in wave energy.

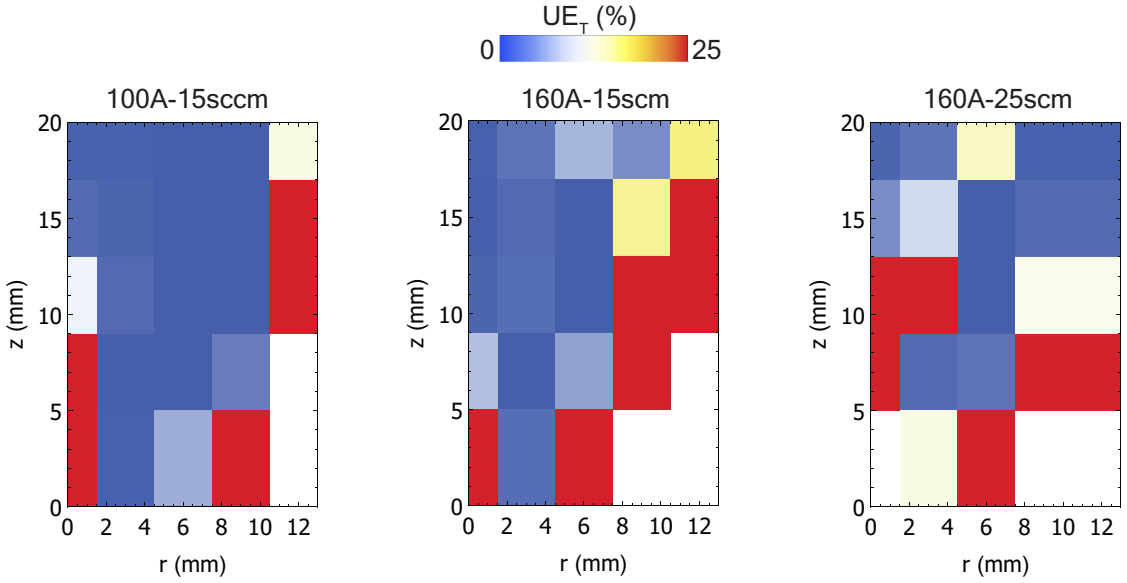

Figure 5.13: Wave energy uncertainty. Note that the red regions indicate uncertainties of 25% or greater.

that wave-particle effects in the direction of the acoustic waves is causing the ion velocity change.

Using the wave spectra we can also determine the mean frequency of the spectra which is relevant to the moment-based approach to estimating IAT wave heating from Sec. 2.4. The mean frequency, ω_0, is determined as follows:

$$\omega_0 = \frac{\omega_r \int W_k(\omega_r) d\omega_r}{\int W_k(\omega_r) d\omega_r}, \tag{5.1}$$

In Fig. 5.14 we show ω_0 in the measurement domain for the three operating conditions analyzed. In general, the average frequency near the orifice is 2 MHz and drops in other regions of the plume.

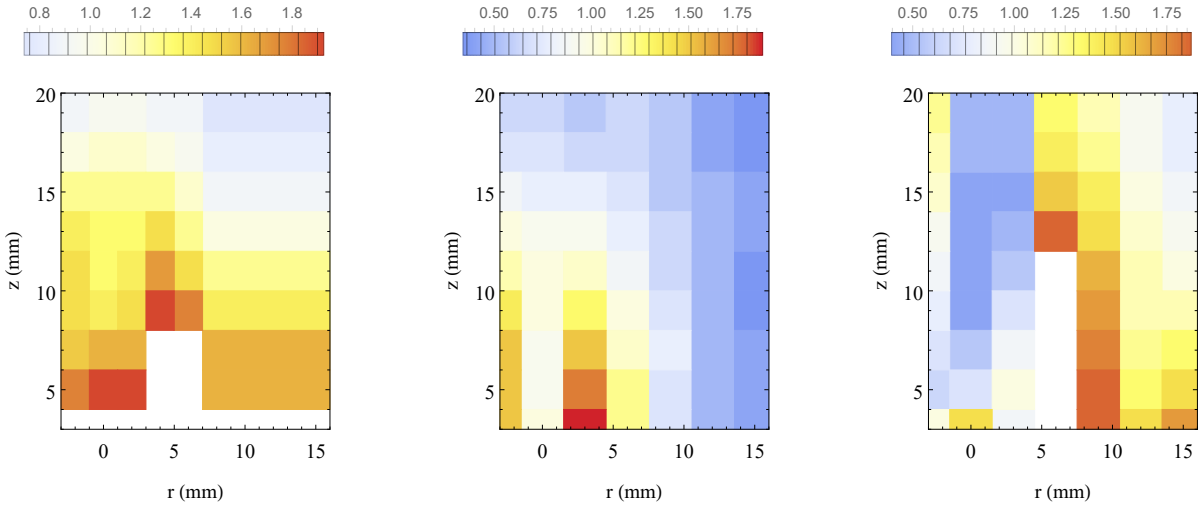

(a) 100A, 15sccm. (b) 100A, 15sccm. (c) 160A, 25sccm.

Figure 5.14: Average IAT frequencies. Note the legend is scaled in [MHz].

5.6 Background Pressure Effects

While the intention of this study was not to investigate the effect of the background pressure on the plume, there was a single operating condition, 130 A, 15sccm, that was performed

for both studies. This provides an opportunity to evaluate background effects at least along the centerline. Note that the higher pressure case was achieved by flowing xenon through a separate leak valve into the chamber.

Figure 5.15 shows some of these properties along the centerline for the two background pressures. In summary, electron temperature, ion temperature, and ion drift velocity was not strongly affected by the higher pressure. However, the plasma density and wave energy showed some effect. Density near the anode for the higher pressure case dropped off at a lower rate than for the low pressure cause, which is expected since it would result in lower ionization rate in the plume. The wave energy showed the most significant difference. As shown in Fig. 5.15(e), which is shown using a logarithmic scale, the wave energy grows exponentially with distance. However, the higher pressure case rolls over sooner and actually decreases in magnitude, in contrast to the lower pressure case which continues to increase and then flatten. This behavior may be due to ion Landau damping or interactions with the neutrals. Although Jorns [1] showed that the damping coefficient due to ion Landau damping was more significant than that due to neutral collisions, it is possible that the ion temperature was first reduced by neutral collisions. Since we measure the final state of the ion temperature, it is not possible to say which effect is more significant without a more detailed model accounting for collisions with neutrals, and without first knowing how much energy the ions obtain from the IAT mode. A practical results of this analysis is that, since the wave energy is more sensitive to background pressure than the other macroscopic parameters, future experiments should be conducted with a representative neutral gas density profile to get accurate wave energy measurements.

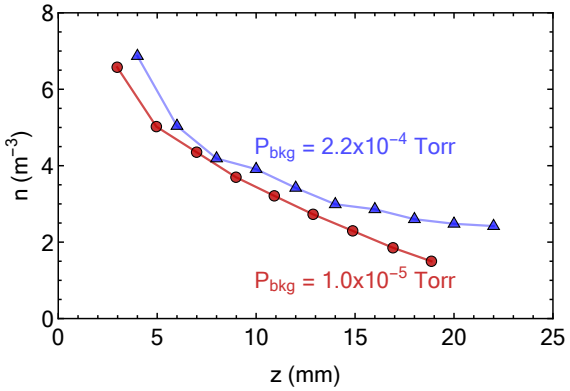

(a) Plasma density.

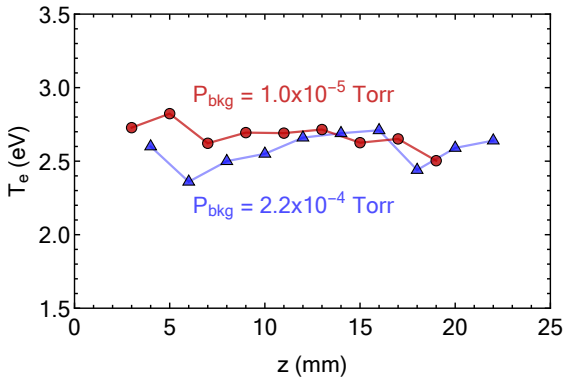

(b) Electron temperature.

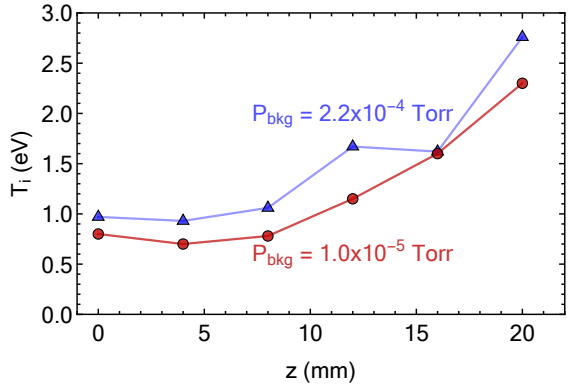

(c) Ion temperature.

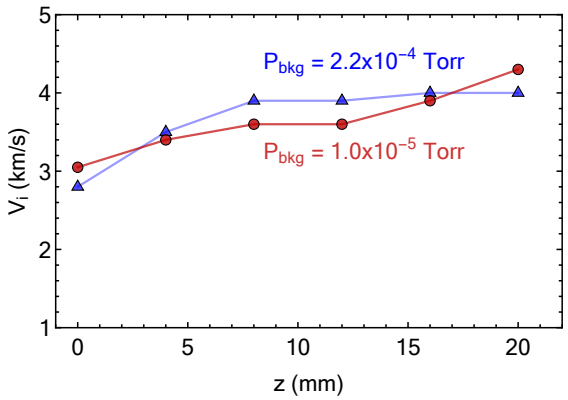

(d) Ion drift velocity.

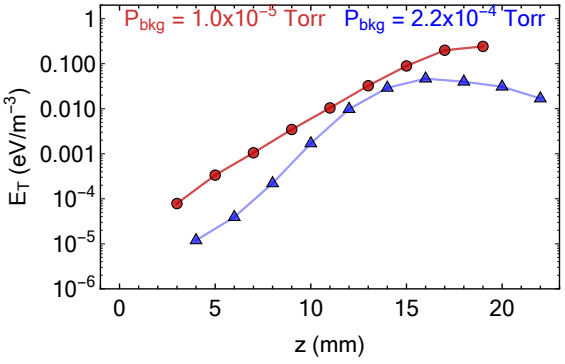

(e) Wave energy (note logarithmic scaling).

Figure 5.15: Comparison of plasma properties for the 130 A, 15 sccm operating condition at two different background pressures.

CHAPTER 6

Conclusion

6.1 Summary of Findings

This dissertation presents the experimental results and analysis of an investigation of the plasma properties in the near plume of a high current hollow cathode operated in a regime dominated by the ion acoustic mode. The motivation for this work was the observation of anomalously energetic ions that are a concern for long duration missions. The conclusion of this study is the following picture. The large electron current carried by this system results in a high density plasma jet with a potential well on axis. This potential structure causes the electrons to flow radially and axially. The ions are accelerated by the pressure which is primarily axial, resulting in a warm beam with up to $\sim$ 10 eV of energy. The electron flow is high enough that the ion acoustic mode is excited and becomes unstable for a wide range of frequencies. This mode is carried by a random walk in velocity space, resulting in an increase in the ion temperature. Typically the ion acoustic mode cannot propagate to the extent measured in this study due to the strong ion Landau damping that occurs for $T_i \approx T_e$. However, because of the large net electron current, along with the properties specific to the hollow cathode plume that result in a large electron drift velocity, the free energy of the electrons overcomes the damping by the ions and ion-neutral collisions, resulting in a positive growth rate and ion heating.

The first significant finding was the confirmation of local ion energy gain in the near plume that appears to correlate with wave energy. A detailed study of this was performed on the centerline and it was found that the ions are already at supersonic velocities in

the near keeper regions, and accelerate downstream. Ion temperatures are found increase in temperature, correlating with the increase in wave energy. A second, two-dimensional analysis was performed to evaluate the propagation of wave energy. It was found that the ion acoustic group velocity vectors correlate with the direction of the change in the IVDF in 2D, implying that the non-resonant wave particle interactions (in which the IAT energy is carried) could be causing the heating. The group velocity vectors occur in the same general direction as the ion drift. We observed the ion and wave propagation in the jet of the plume to be similar for all operating conditions. However, the amplitude of the fluctuation energy was larger by several orders of magnitude for one case that also corresponded to the case with the most ion heating. This same trend was found with the detailed analysis of the scaling of wave energy and ion temperature along the centerline: higher IAT wave energy results in larger ion temperature. These results show a clear correlation between wave energy and ion temperature in the cathode plume.

6.2 Recommendations for Future Work

The following sections discuss the author's recommendation for future efforts to better understand the cathode plume. While some suggestions for specific experiments or analyses are given, the emphasis is on the key information desired and what it could reveal about the important plasma processes of the cathode plume.

6.2.1 EVDF measurements

No measurements of the EVDF were attempted in this experiment, and it was assumed that it was Maxwellian. However, others have measured non-Maxwellian EVDF's in cathode plumes. A non-Maxwellian electron population has important effects on the interpretation of probe results, the IAT dispersion relation, the nature of the instability (knowing the electron Mach number), and the location of the source of the ion acoustic waves.

6.2.2 Corrected Probe Measurements for Flow

Because of the high Mach numbers of both the electrons and ions, particle flow effects might be significant. To assess this, it is recommended to assess the flow effects in similar operating conditions. This can be achieved by using an axially-oriented cylindrical probe, or perhaps a flat probe, and comparing to the orientation used here. The cylindrical probe could collect plasma primarily perpendicular to the flow, assuming the probe alignment is parallel to the net drift direction (which in many regions are collinear). Use of the flat probe requires corrections but this is simplified compared to that needed for cylindrical probes oriented with the probe axis parallel to the particle flow.

6.2.3 Assess effects of an external magnetic field

Thus far neither the ion properties nor the wave properties have been measured with a realistic external magnetic field. This was done for simplicity. However, a magnetic field will alter the dispersion relation and the electron trajectories which in turn will affect the plasma potential structure, wave propagation directions, and possibly the heating of the ions. A study like this one with a magnetic field could elucidate the magnetic field effects, informing future experiment requirements and clarifying the relevance of experiments performed without a magnetic field to more realistic conditions.

6.2.4 Identify conditions associated with energetic ions incident on the keeper

This work was motivated by measurements of high energy ions and anomalous keeper erosion in regimes associated with the IAT mode. However, except for a couple operating conditions in which it was suspected that plume mode (or some other instability) existed concurrently, none of the cases investigated here showed ions with anomalous energy entering the region near the keeper. One explanation is the low SNR near the keeper prevented measuring the backward-going, energetic ions incident on the keeper. Another is that multiply-charged ions

falling through the sheath which would have more energy and thus cause increased erosion due to the nonlinear scaling of ion energy with sputter yield. This might be investigated by optical emission spectroscopy. Work done recently by Thomas [61] used OES on the plume of a high-current hollow cathode to show that the amount of sputtered carbon present in the plume correlated with higher concentrations of triply-charged xenon. Perhaps the operating conditions in which IAT is significant correspond to high populations of doubly- or triply-charged ions, which cannot be measured using the LIF technique employed for this study. Further investigation into conditions that might result in ions with significant keeper-directed velocity is recommended.

6.2.5 LIF measurements

The axial IVDF's obtained in front of the keeper face were obscured by the signal peak caused by the reflection of the laser beam off of the keeper orifice face or the keeper itself, which had become coated with tungsten from the liners on the inside of the anode sputtered by ions. Because one of the motivations for this research was to address the cause of the anomalous erosion seen on the keeper face, it is important to have improved axial IVDF measurements in front of the keeper. If sputtering cannot be prevented, then one solution would be to orient the axial injection laser beam at an angle relative the cathode axis such that the reflected beam doesn't intersect the interrogation volume. With IVDF's obtained in this manner, along with density measurements and estimates of the keeper sheath potential drop, the ion energy distribution incident on the keeper face could be calculated and total sputter rate estimated.

It would also be useful to perform a study of the effect of laser intensity on saturation broadening in the near plume. The model used for estimating saturation broadening in this study was comprised of only two energy levels, and may not be justified. Measuring the line broadening for a range of laser intensities could reveal the range of applicability of this model. Such a study could be performed for a range of mass flow rates and discharge currents in

order to see the dependence of the broadening on parameters such as plasma density, electron temperature, ion temperature, and neutral gas density, all of which factor into the two-level model. In this study the effects of saturation were treated as an uncertainty because such a study has not been performed. With a database of saturation levels the ion temperatures and ion heating-wave energy scaling parameter uncertainties could be reduced. This would also be useful to the EP community in general since the high SNR possible with a partially to moderately saturated transition has advantages in terms of time and the accessibility of regions of plasma where typical intensities result in low or no signal.

While the LIF performed here resulted in 2D measurements of the axial and radial temperatures and the 2D flow velocity vectors, the full 2D IVDF in the plume has not yet been mapped. While this would likely be a time-intensive experiment, understanding the full IVDF evolution in the near plume could provide more confirmation of the relevance of the wave-ion interactions in regards to ion heating. For example, this measurement could reveal if the IVDF's appear to be stretching in the direction of the ion acoustic waves. Additionally, since anisotropy has been shown to exist in this study, it would be interesting to see how this anisotropy evolves.

Finally, the high neutral gas and plasma densities in the plumes tested here result in high estimated neutral gas collision frequencies. These collisions will result in a reduction in energy of the ions and an increase in the energy of the neutrals. If the neutral velocity distribution function could be measured, the collision frequency and energy transfer could be inferred, and this would serve as a benchmark for models of the plume.

6.2.6 Evaluate the role of plume mode oscillations on ion heating in these types of IAT regimes

It was assumed in this study that because the amplitude of the density fluctuations in the low-frequency range was small relative to the IAT frequency regions that the effects of plume mode could be neglected. However, since the nature of plume mode is not understood it is

not clear that its influence can be ruled out. Further understanding of this mode, how it can affect the ion population, and how it can perhaps couple with the IAT mode is necessary for a full picture of ion heating.

6.2.7 Further analysis

The cause of the acceleration of the fast ion population is suspected to related to the plasma pressure gradient, which is steep in the near plume region. Since the acceleration of this population is a large contributor to the overall energy, the mechanism behind it is important to understand. Additionally, while there is a qualitative correlation between ion drift direction and wave propagation, a more detailed analysis of the effects of the waves on the particles is needed to see if collisions between fast ions in the tail and the bulk population might be able to alter the bulk ion velocity. The relative strengths of the the wave and pressure gradient effects could then be compared to see if the observed ion velocity profile can be explained based on these mechanisms alone.

6.3 Final Thoughts

This work has contributed new information on the properties of the near plume plasma of a high current hollow cathode plume. The measurements have and will continue to be used to formulate theoretical and computational models of hollow cathodes which will be used to self-consistently predict plasma behavior and estimate device lifetime for space missions using electric propulsion. 2D maps of ion acoustic wave propagation, energy, and fluctuation spectra might serve to validate theories for wave growth and propagation.

The results from these experiments will also be utilized as a data set for developing and validating cathode plume models in more realistic configurations, which will reduce the high costs and long duration of the lifetime qualification of the next generation of hollow cathodes. The improved understanding of the role that IAT has in energetic ion production

and the wave-particle energy balance in the plume will also enable a better understanding of all hollow cathodes, including lower-current designs currently flown.

Appendix A

Plasma Property Maps

A.1 Dispersion Relation Measurements

Following are the dispersion relations for all the operating conditions measured.

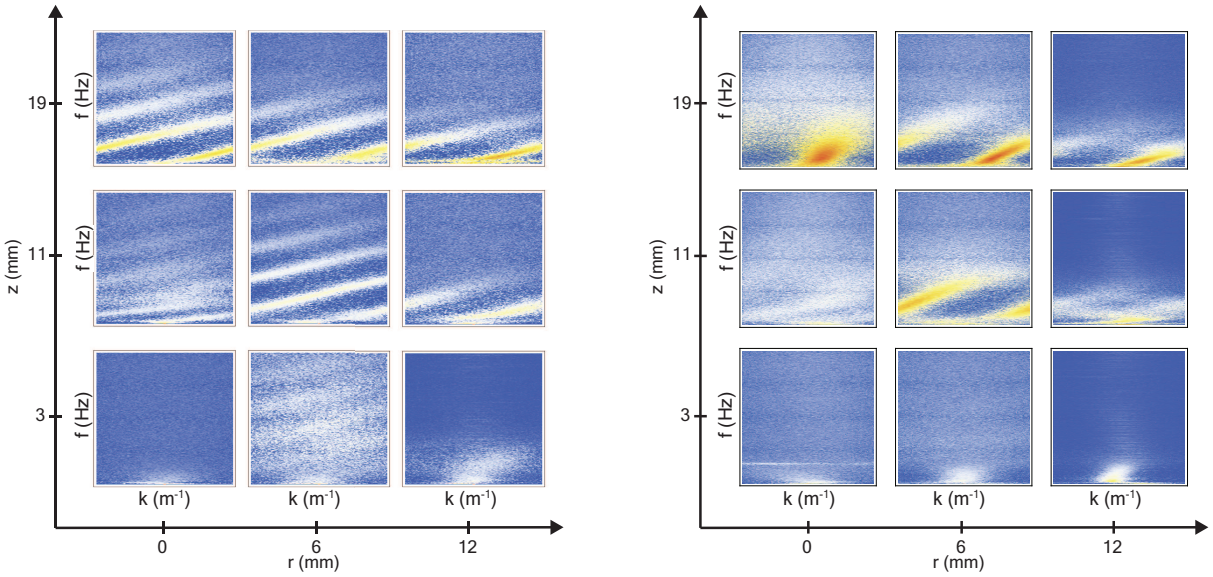

(a) Axial dispersion relations.

(b) Radial dispersion relations.

Figure A.1: Dispersion relations for the 100 A, 15 sccm operating condition.

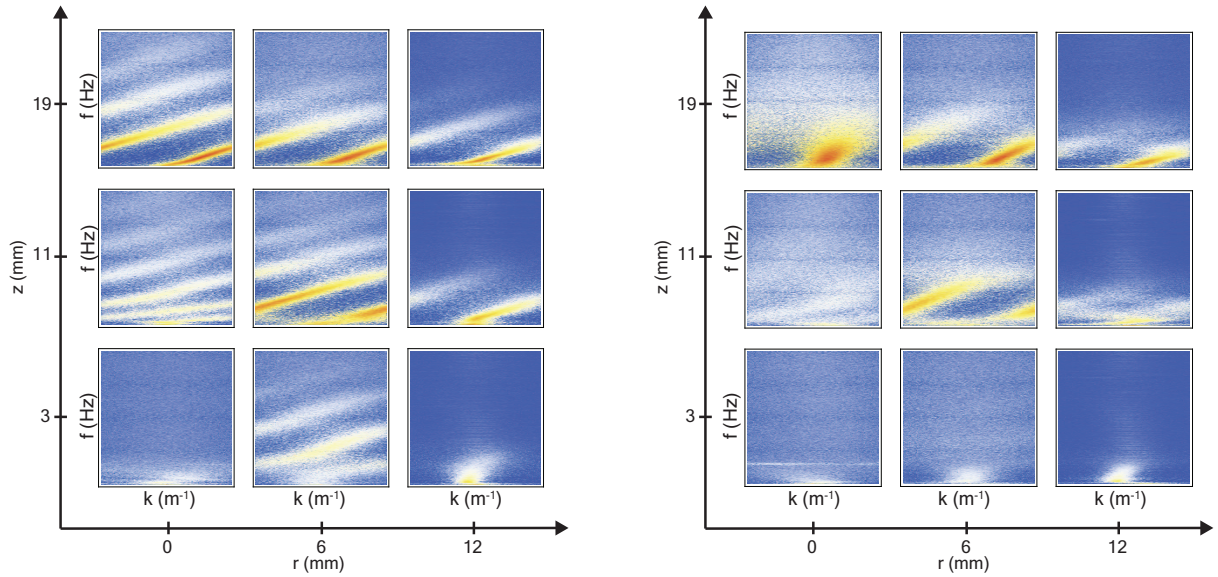

(a) Axial dispersion relations.

(b) Radial dispersion relations.

Figure A.2: Dispersion relations for the 130 A, 15 sccm operating condition.

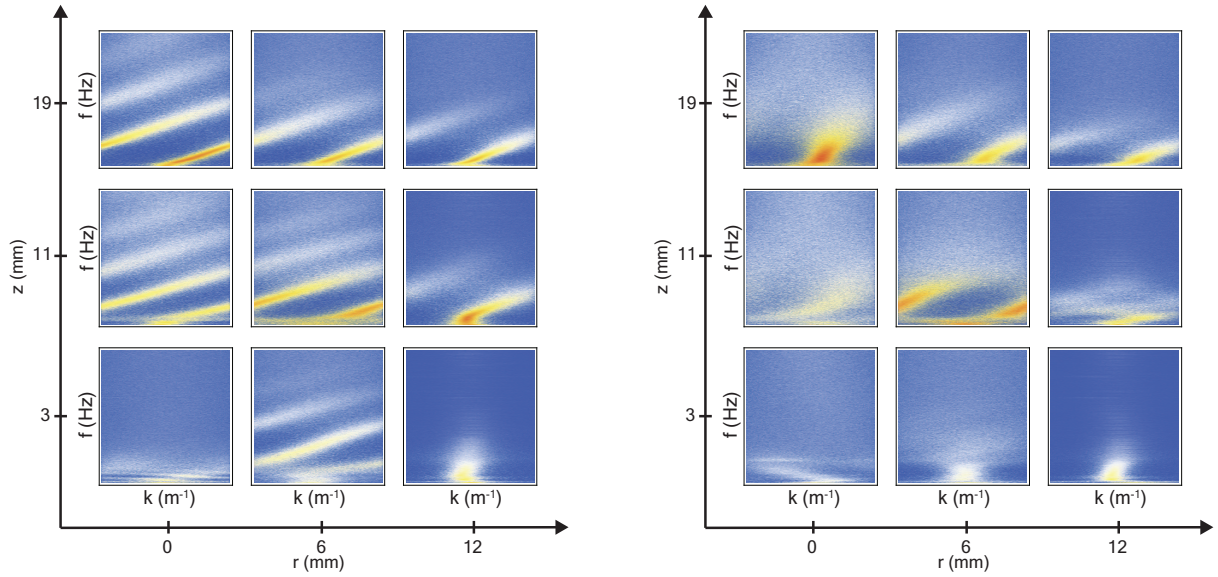

(a) Axial dispersion relations.

(b) Radial dispersion relations.

Figure A.3: Dispersion Relation Measurements

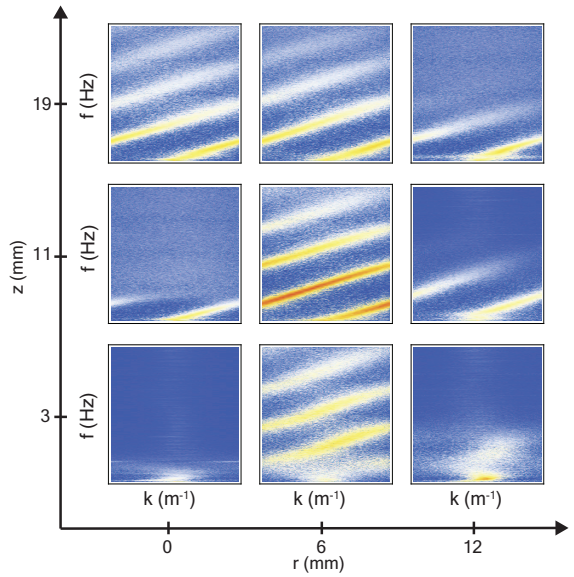

(a) Axial dispersion relations.

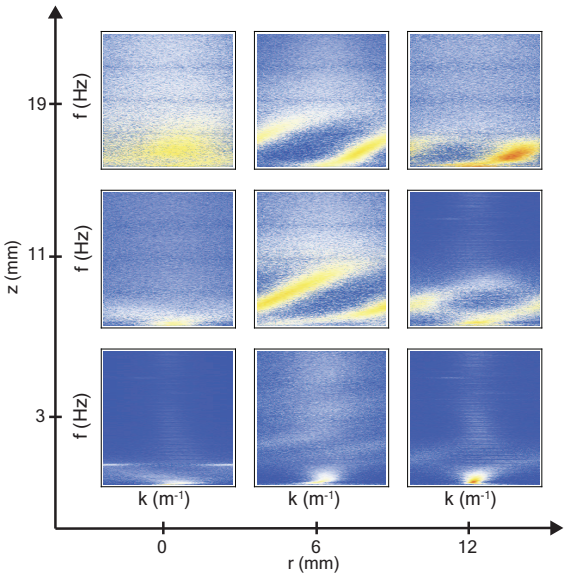

(b) Radial dispersion relations.

Figure A.4: Dispersion relations for the 160 A, 20 sccm operating condition.

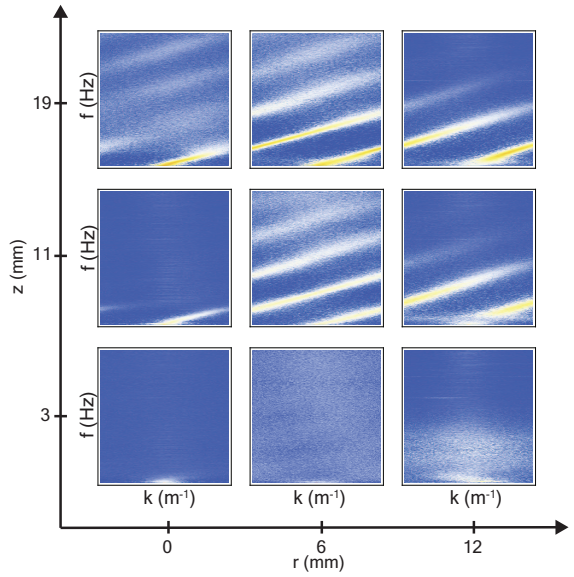

(a) Axial dispersion relations.

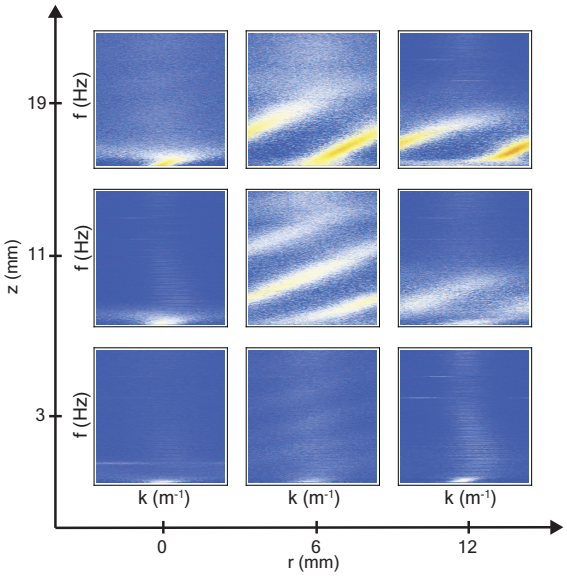

(b) Radial dispersion relations.

Figure A.5: Dispersion relations for the 160 A, 25 sccm operating condition.

A.2 Fluctuation Spectra

The following plots show the fluctuation spectra for the 2D experiment. The vertical axis is normalized to the maximum of the IAT portion of the potential spectrum to exmphase the shape of the line shape. It should be noted that the amplitudes of the spectra varied widely.

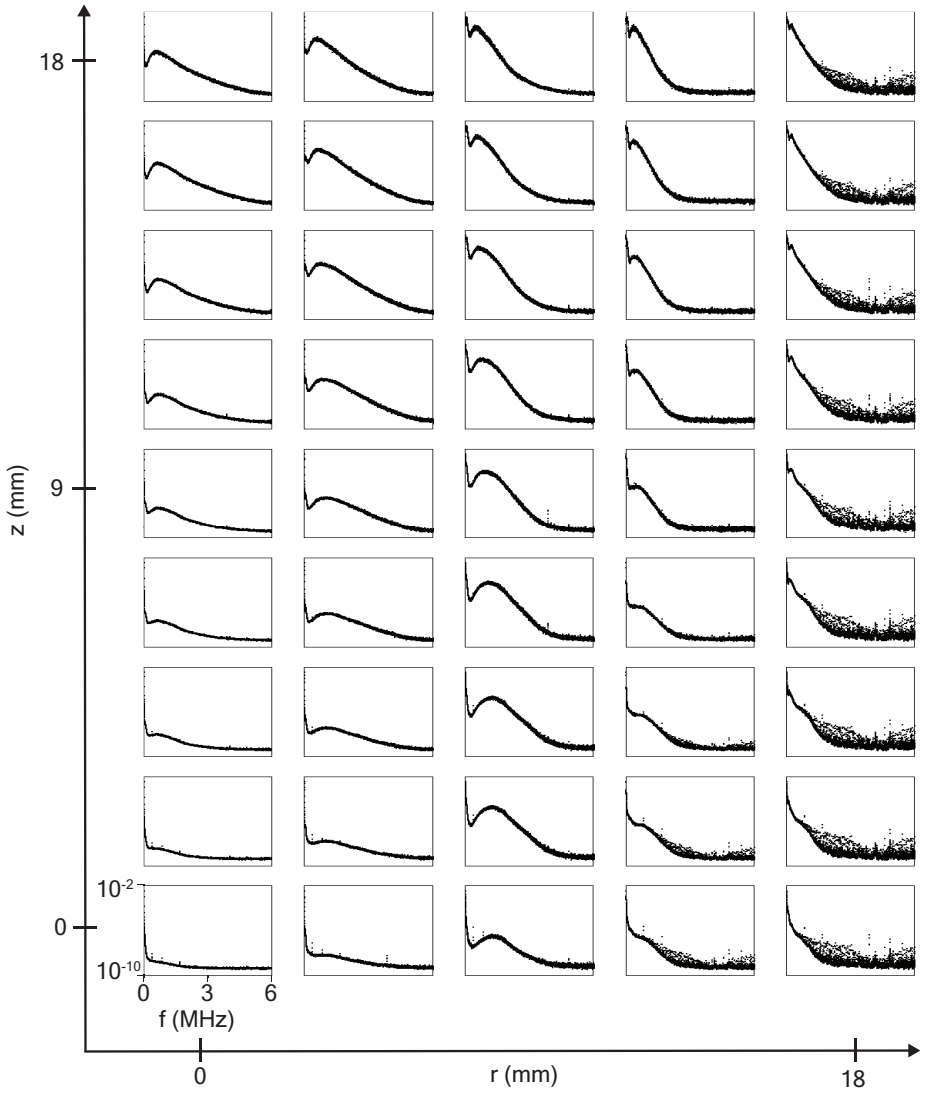

Figure A.6: Fluctuation spectra for the 100 A, 15 sccm operating condition. The vertical axis of each plot is the logarithm of the plasma potential fluctuation power, $|\widetilde{\phi}|^2$.

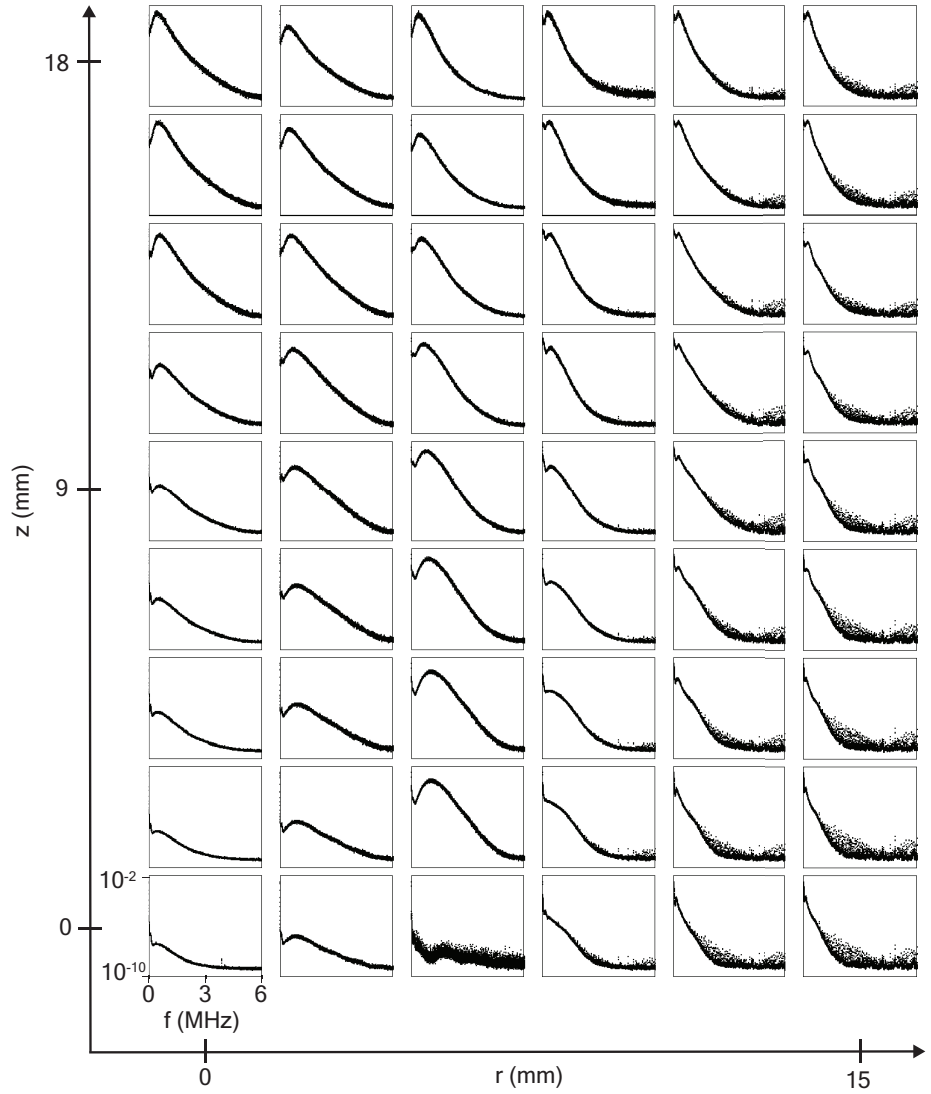

Figure A.7: Fluctuation spectra for the 130 A, 15 sccm operating condition. The vertical axis of each plot is the logarithm of the plasma potential fluctuation power, $|\widetilde{\phi}|^2$.

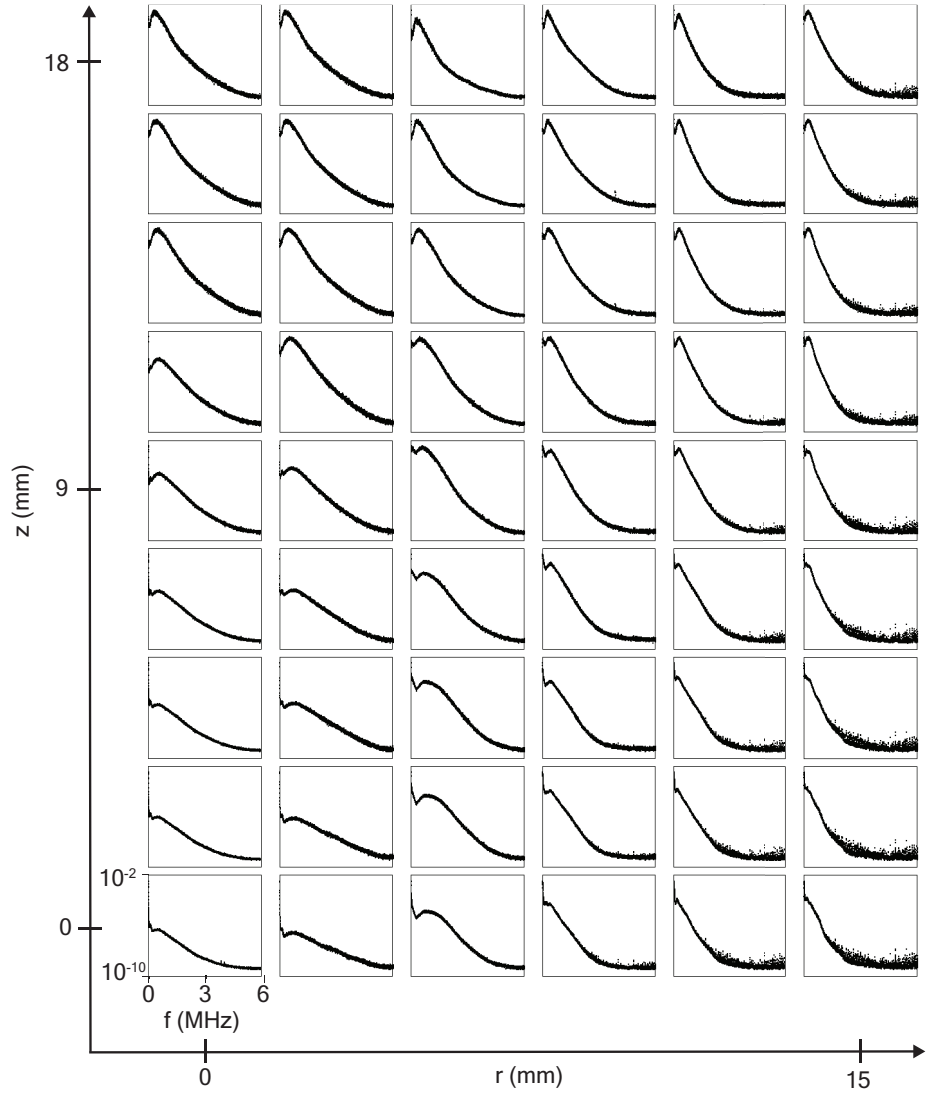

Figure A.8: Fluctuation spectra for the 160 A, 15 sccm operating condition. The vertical axis of each plot is the logarithm of the plasma potential fluctuation power, $|\widetilde{\phi}|^2$.

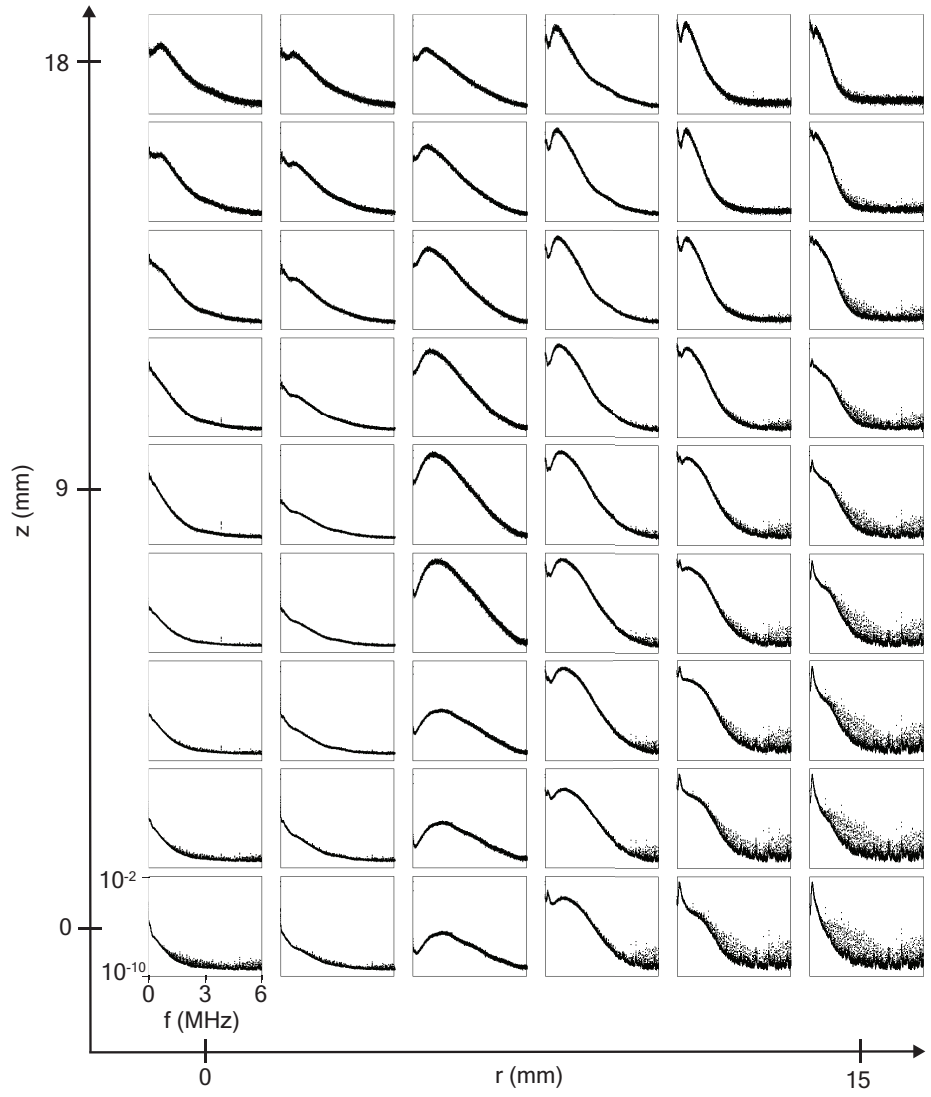

Figure A.9: Fluctuation spectra for the 160 A, 20 sccm operating condition. The vertical axis of each plot is the logarithm of the plasma potential fluctuation power, $|\widetilde{\phi}|^2$.

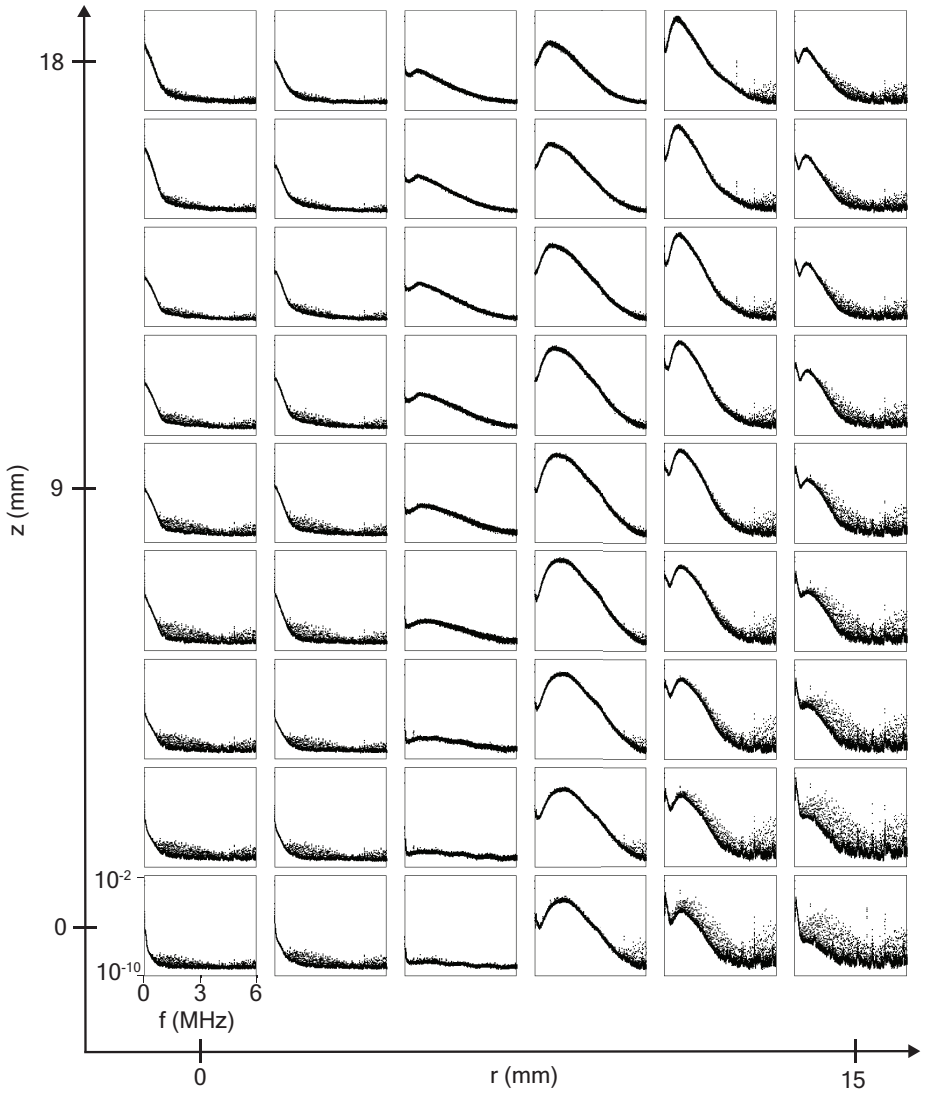

Figure A.10: Fluctuation spectra for the 160 A, 25 sccm operating condition. The vertical axis of each plot is the logarithm of the plasma potential fluctuation power, $|\widetilde{\phi}|^2$.

A.3 Ion Temperature Uncertainty

The uncertainties due to curve fitting and saturation broadening are shown here for the three cases where 2D LIF map were taken. The intensity scale is the same for all three sets of plots. A final note is that, while the relative uncertainty of the 100 A, 15 sccm condition is significantly higher than for the other two cases, because the temperatures were low (minimal ion heating) the absolute uncertainties were not significant.

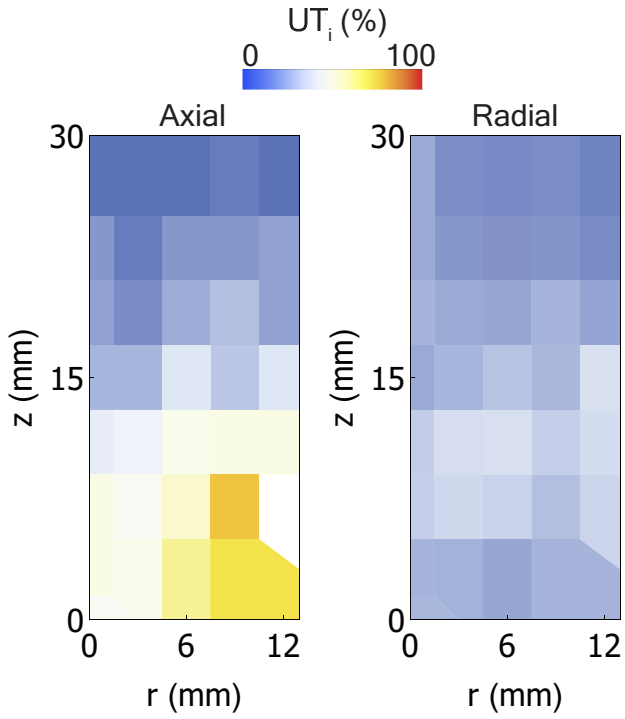

Figure A.11: Ion temperature uncertainty for the axial and radial LIF measurements at the 100A, 15sccm operating condition.

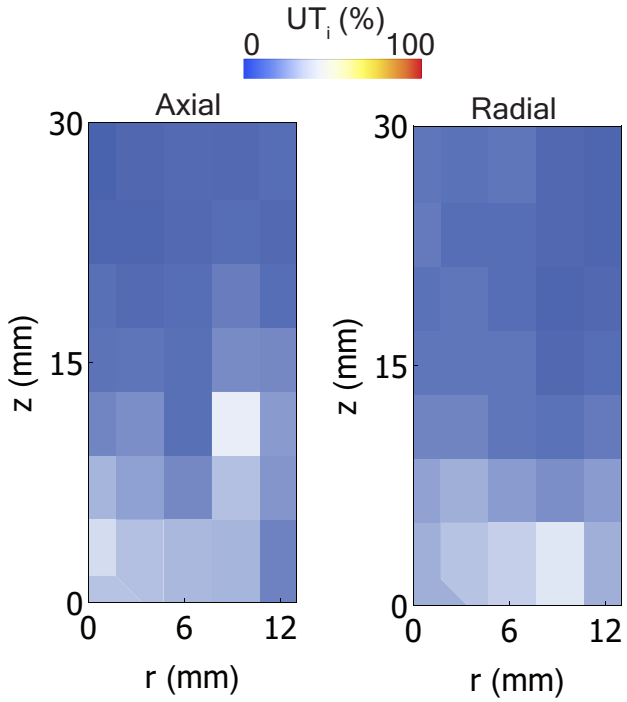

Figure A.12: Ion temperature uncertainty for the axial and radial LIF measurements at the 160A, 15sccm operating condition.

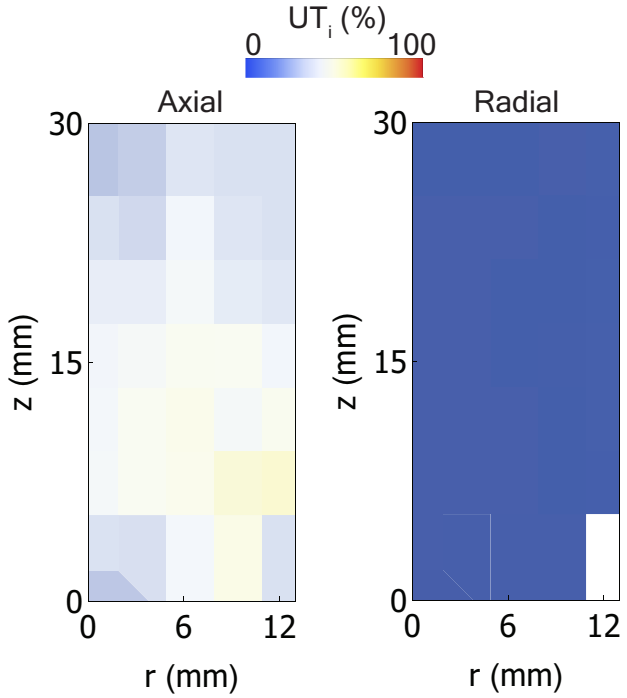

Figure A.13: Ion temperature uncertainty for the axial and radial LIF measurements at the 160A, 25sccm operating condition.

Bibliography

[1] Jorns, B. A., , C., Goebel, D. M., and Wirz, R., "Propagation of ion acoustic wave energy in the plume of a high-current LaB6 hollow cathode," *Physical Review E*, Vol. 96, No. 2, 2017, pp. 023208.

[2] Dodson, C. A., Jorns, B. A., and Wirz, R. E., "Ion Acoustic Wave Propagation and Heating in a High-Current Hollow Cathode Plume," *International Electric Propulsion Conference*, 2017, pp. IEPC–2017–398.

[3] Polk, J., "An Overview of the Nuclear Electric Xenon Ion System (NEXIS) Program," *39th AIAA/ASME/SAE/ASEE Joint Propulsion Conference & Exhibit*, 2003.

[4] Mikellides, I. G., Katz, I., Hofer, R. R., and Goebel, D. M., "Magnetic Shielding of the Acceleration Channel Walls in a Long-Life Hall Thruster," *46th AIAA/ASME/SAE/ASEE Joint Propulsion Converence & Exhibit*, 2010.

[5] Kamhawi, H., Huang, W., Haag, T., Yim, J., Chang, L., Clayman, L., Herman, D., Shastry, R., Thomas, R., Griffith, C., Myers, J., Williams, G., Mikellides, I. G., Hofer, R., Polk, J. E., and Goebel, D. M., "Overview of the Development of the Solar Electric Propulsion Technology Demonstration Mission 12.5 kW Hall Thruster," *50th AIAA/ASME/SAE/ASEE Joint Propulsion Conference & Exhibit*, 2014.

[6] Hofer, R. R., Kamhawi, H., Herman, D., Polk, J. E., Snyder, J. S., Mikellides, I., Huang, W., Myers, J., Yim, J., Williams, G., Ortega, A. L., Jorns, B., Sekerak, M., Griffiths, C., Shastry, R., Haag, T., Verhey, T., Gilliam, B., Katz, I., Goebel, D. M., Anderson, J. R., Gilland, J., and Clayman, L., "Development Approach and Status of the 12.5 kW HERMeS Hall Thruster for the Solar Electric Propulsion Technology Demonstration Mission," *34th International Electric Propulsion Conference*, 2015.

[7] Goebel, D. M. and Polk, J. E., "Lanthanum Hexaboride Hollow Cathode for the As-

teroid Redirect Robotic Mission 12.5 kW Hall Thruster," *34th International Electric Propulsion Conference*, 2015.

[8] Goebel, D. M. and Chu, E., "High Current Lanthanum Hexaboride Hollow Cathode 20-to-100 kW Class Hall Thrusters," *Journal of Propulsion and Power*, Vol. 30, No. Jan-Feb, 2014, pp. 30–40.

[9] Conversano, R., Goebel, D., Hofer, R., Matlock, T., and Wirz, R., "Magnetically Shielded Miniature Hall Thruster: Development and Initial Testing," *International Electric Propulsion Conference*, 2013.

[10] Hoskins, A., Aadland, R., Meckel, N., Talerico, L., and Monheiser, J., "NEXT Ion Propulsion System Production Readiness," *43rd AIAA/ASME/SAE/ASEE Joint Propulsion Conference & Exhibit*, , No. July, 2007, pp. 1–16.

[11] Goebel, D. M. and Katz, I. K., *Fundamentals of Electric Propulsion*, JPL Space Science and Technology Series, California, 2008.

[12] Rawlin, V. K., "Internal Erosion Rates of a 10-kW Xenon Ion Thruster AIAA-88-2912," *24th AIAA/ASME/SAE/ASEE Joint Propulsion Conference*, 1988.

[13] Brophy, J. R. and Garner, C. E., "Tests of High Current Hollow Cathodes for Ion Engines," *AIAA/ASME/SAE/ASEE 24th Joint Propulsion Conference*, 1988.

[14] Friedly, V. and Wilbur, P., "High Current Hollow Cathode Phenomena," *21st International Electric Propulsion Conference*, Vol. 8, No. 3, 1990, pp. 635–643.

[15] Friedly, V., "Hollow cathode operation at high discharge currents," Tech. rep.

[16] Foster, J. E. and Patterson, M. J., "Plasma Emission Characteristics from a High Current Hollow Cathode in an Ion Thruster Discharge Chamber," Tech. rep., 2002.

[17] Goebel, D. M., Jameson, K. K., Katz, I., and Mikellides, I. G., "Potential fluctuations and energetic ion production in hollow cathode discharges," *Physics of Plasmas*, Vol. 14, No. 10, 2007.

[18] Farnell, C., *Plasma flow field measurements downstream of a hollow cathode*, Ph.D. thesis, 2008.

[19] Chu, E., *External Mass Injection to Reduce Energetic Ion Production in the Discharge Plume of High Current Hollow Cathodes*, Master's thesis, 2012.

[20] Chu, E., Goebel, D. M., and Wirz, R. E., "Reduction of Energetic Ion Production in Hollow Cathodes by External Gas Injection," *Journal of Propulsion and Power*, Vol. 29, No. 5, 2013, pp. 1155–1163.

[21] Jorns, B. A., Mikellides, I. G., Goebel, D. M., and Ortega, A. L., "Mitigation of energetic ions and keeper erosion in a high-current hollow cathode," *International Electric Propulsion Conference*, 2015.

[22] Sommers, B. S., Foster, J. E., Davis, C. N., and Viges, E., "Preliminary Characterization of Ion Energy Spectra Acquired from High Current Hollow Cathodes," *33rd International Electric Propulsion Conference*, 2013.

[23] Ho, A. K., Jorns, B. A., Goebel, D. M., Mikellides, I. G., and Lopez-Ortega, A., "Wear Test Demonstration of a Technique to Mitigate Keeper Erosion in a High-Current LaB6 Hollow Cathode," *52nd AIAA/SAE/ASEE Joint Propulsion Conference*, 2016.

[24] Mikellides, I. G., Katz, I., Goebel, D. M., and Jameson, K. K., "Evidence of nonclassical plasma transport in hollow cathodes for electric propulsion," *Journal of Applied Physics*, Vol. 101, No. 6, 2007.

[25] Jorns, B. A., Mikellides, I. G., and Goebel, D. M., "Temporal Fluctuations in a 100-A LaB6 Hollow Cathode," *33rd International Electric Propulsion Conference*, 2013.

[26] Jorns, B. A., Mikellides, I. G., and Goebel, D. M., "Ion acoustic turbulence in a 100-A LaB 6 hollow cathode," *Physical Review E*, Vol. 90, No. 6, 2014.

[27] Jorns, B., Goebel, D. M., and Mikellides, I. G., "Investigation of Energetic Ions in a 100-A Hollow Cathode," *50th AIAA/ASME/SAE/ASEE Joint Propulsion Conference*, 2014.

[28] Fenneman, D. B., Raether, M., and Yamada, M., "Ion-acoustic instability in the positive column of a helium discharge," Vol. 871, No. 1973, 1973.

[29] Gekelman, W. and Stenzel, R. L., "Ion sound turbulence in a magnetoplasma," *Phys. Fluids*, Vol. 21, No. 11, 1978.

[30] Slusher, R. E., Surko, C. M., Moler, D. R., and Porkolab, M., "Study of Current-Driven Ion-Acoustic Instability Using CO2-Laser Scattering," Vol. 57, No. 21, 1976, pp. 1407–1410.

[31] Hamberger, S. M. and Jancarik, J., "Experimental studies of electrostatic fluctuations in a turbulently heated plasma," *Physics of Fluids*, Vol. 15, No. 5, 1972, pp. 825–836.

[32] Fried, B. D. and Gould, R. W., "Longitudinal ion oscillations in a hot plasma," *Physics of Fluids*, Vol. 4, No. 1, 1961, pp. 139–147.

[33] Bhatnagar, P. L., Gross, E. P., and Krook, M., "A model for collision processes in gases. I. Small amplitude processes in charged and neutral one-component systems," *Physical Review*, Vol. 94, No. 3, 1954, pp. 511–525.

[34] Huba, J. D., *NRL Plasma Formulary*, Naval Research Laboratory, Washington, DC, 2016.

[35] Landau, L., "On the vibrations of the electronic plasma," *Journal of Physics*, Vol. X, No. 1, 1946.

[36] Kadomtsev, B. B., *Plasma Turbulence*, Academic Press, New York, 1965.

[37] Levko, D., Krasik, Y. E., Vekselman, V., and Haber, I., "Two-dimensional model of orificed micro-hollow cathode discharge for space application," *Physics of Plasmas*, Vol. 20, No. 2013, 2013, pp. 083512.

[38] Sagdeev, R. Z. and Galeev, A. A., *Nonlinear Plasma Theory*, W. A. Benjamin, New York, 1969.

[39] Jorns, B. A., Lopez-Ortega, A., and Mikellides, I. G., "First-principles modeling of IAT-driven anomalous resistivity in hollow cathodes discharges I: Theory," *52nd AIAA/SAE/ASEE Joint Propulsion Conference*, 2016.

[40] Lopez-Ortega, A., Mikellides, I. G., and Jorns, B. A., "First-principles Modeling of IAT-driven Anomalous Resistivity in Hollow Cathode Discharges II: Numerical Simulations and Comparisons with Experiments," *52nd AIAA/SAE/ASEE Joint Propulsion Conference*, 2016.

[41] Conversano, R. W., *Low-Power Magnetically Shielded Hall Thrusters*, Ph.D. thesis, 2017.

[42] Hutchinson, I., *Principles of Plasma Diagnostics*, Cambridge University Press, 2005.

[43] Chen, F. F., "Langmuir probe diagnostics," *Mini-Course on Plasma Diagnostics, IEEE-ICOPS Meeting, Jeju, Korea*, 2003.

[44] Tsytovich, V., *Theory of Turbulent Plasma*, Plenum Publishing Corporation, New York, 1977.

[45] Beall, J. M., "Estimation of wavenumber and frequency spectra using fixed probe pairs," *Journal of Applied Physics*, Vol. 53, No. 6, 1982, pp. 3933.

[46] Manzella, D. H., "Stationary Plasma Thruster Ion Velocity Distribution," Tech. rep., 1994.

[47] Hargus, W. A. and Charles, C. S., "Near Exit Plane Velocity Field of a 200-Watt Hall Thruster," *Journal of Propulsion and Power*, Vol. 24, No. 1, Jan 2008, pp. 127–133.

[48] Williams, G., Smith, T., Domonkos, M., Gallimore, A., and Drake, R., "Laser-induced fluorescence characterization of ions emitted from hollow cathodes," *IEEE Transactions on Plasma Science*, Vol. 28, No. 5, 2000, pp. 1664–1675.

[49] Georgin, M., Durot, C., and Gallimore, A. D., "Preliminary Measurements of Time Resolved Ion Velocity Distributions Near a Hollow Cathode," *International Electric Propulsion Conference*, 2015.

[50] Huang, W., Gallimore, A. D., and Hofer, R. R., "Neutral Flow Evolution in a Six-Kilowatt Hall Thruster," *Journal of Propulsion and Power*, Vol. 27, No. 3, 2011, pp. 553–563.

[51] Huang, W., Smith, T. B., and Gallimore, A. D., "Obtaining Velocity Distribution using a Xenon Ion Line with Unknown Hyperfine Constants," , No. June, 2009, pp. 22–25.

[52] Chaplin, V. H., Conversano, R. W., Lobbia, R. B., Ortega, A., Mikellides, I. G., Hofer, R. R., and Jorns, B. A., "Laser-induced Fluorescence Measurements of the Acceleration Zone in the 12.5 kW HERMeS Hall Thruster," *35th International Electric Propulsion Conference*, 2017.

[53] Dodson, C. A., Perez-Grande, D., Jorns, B. A., Goebel, D. M., and Wirz, R. E., "Laser-induced Fluorescence Measurements of Energetic Ions in a 100-A LaB6 Hollow Cathode Plume," *52nd AIAA/SAE/ASEE Joint Propulsion Conference*, 2016, pp. 1–17.

[54] Ishihara, O. and Hirose, A., "Quasilinear mechanism of high-energy ion-tail formation in the ion-acoustic instability," *Physical Review Letters*, Vol. 46, No. 12, 1981.

[55] McMahon, J. C., Xu, G. Z., and Laframboise, J. G., "The effect of ion drift on the sheath, presheath, and ion-current collection for cylinders in a collisionless plasma," *Physics of Plasmas*, Vol. 12, No. 6, 2005, pp. 1–11.

[56] Sheridan, T. E. and Goree, J., "Langmuir-probe characteristic in the presence of drifting electrons," *Physical Review E*, Vol. 50, No. 4, 1994, pp. 2991–2996.

[57] Georgin, M. P., Jorns, B. A., and Gallimore, A. D., "An Experimental and Theoretical Study of Hollow Cathode Plume Mode Oscillations," *Iepc2017*, 2017, pp. 1–8.

[58] Georgin, M. P., Jorns, B. A., and Gallimore, A. D., "Plasma Instabilities in the Plume of a Hollow Cathode," 2018, pp. 1–11.

[59] Dubinov, A. E. and Kitayev, I. N., "Can Ion-Acoustic Waves in Plasma Be Backward Waves ?" Vol. 25, No. 2, 2017, pp. 137–139.

[60] Dodson, Christopher A., P.-G. D. J. B. A. G. D. M. and Wirz, R. E., "Ion Heating Measurements on the Centerline of a High-Current Hollow Cathode Plume," *Journal of Propulsion and Power*, Vol. 34, No. 5, Sept-Oct 2018, pp. 1225–1234.

[61] Thomas, R. E., Kamhawi, H., and Williams, G. J., "High Current Hollow Cathode Plasma Plume Measurements," *Iepc*, 2013, pp. 1–17.